Numerical Investigation on Large-sized Bubble Injection for Control of Turbulent Boundary Layer

－Horizontal channel flow and bubble-induced drag reduction－

A dissertation submitted to the

HOKKAIDO UNIVERSITY

for the degree of
Doctor of Philosophy

presented by

Sangwon KIM

Graduate School of Engineering

born March 21st, 1989

Supervised by Prof. Nobuyuki OSHIMA

prepared at *Computational Fluid Mechanic Laboratory*

北海道大学工学院 機械宇宙工学専攻
計算流体工学研究室
Computational Fluid Mechanics Lab.

Numerical Investigation on Large-sized Bubble Injection for Control of Turbulent Boundary Layer

Thesis for Ph. D. (Eng.) at Hokkaido University

Advisory Committee
Prof. D.Eng. Nobuyuki Oshima, Hokkaido University, Chair / Chief examiner
Prof. PhD. Yuichi Murai, Hokkaido University, Co-examiner
Prof. PhD. Masao Watanabe, Hokkaido University, Co-examiner
Assoc. Prof. PhD. Hiroshi Terashima, Hokkaido University, Co-examiner

Acknowledgment

August 24, 2021

Sangwon Kim

Abstract

The control of turbulent boundary layers by injecting bubbles has many advantages because the bubbles consistently modify the boundary layer by traveling with the main flow. The characteristics of these bubbly flows, which can be divided into vertical and horizontal bubbly flows, change depending on the direction of buoyancy relative to that of the main flow. However, horizontal bubbly flows have received less attention than vertical bubbly flows because buoyancy acts in the wall-normal direction and hinders heat exchange and mass transfer between the main flow and wall, rendering horizontal bubbly flow unsuitable for industrial demands and more complex flows. The horizontal bubbly flow modifies the inner-layer structure of the turbulent boundary layer formed beneath a horizontal flat wall, thus reducing the frictional drag on the upper wall. This characteristic is called bubble drag reduction (BDR) and is applied to liquid transport in pipelines and ship surfaces in water. In particular, the energy efficiency of large vessels can be promoted by reducing the frictional drag, which accounts for 80% of the total drag. Many previous studies on horizontal bubbly flow have been based on microbubbles for inducing BDR. The typical micro-bubble method applied in industrial fields contains bubbles of a- few- millimeters, which frequently coalesce in the shear layer and become large-sized bubbles in the downstream region. Furthermore, air films, which are also used for drag reduction and implemented by injecting air on a superhydrophobic surface to separate the liquid phase of the flow from the wall, are broken up and separated into large-sized bubbles from the downstream; however, the critical size of these large-sized bubble has not yet been determined. From this perspective, understanding large-sized bubbles is essential to retain drag reduction from the downstream. Recently, it was discovered that large-sized bubbles provided a velocity gradient that calmed the wake region; furthermore, the drag reduction performance depended on the bubble length. Interestingly, large-sized bubbles show a common spatial relationship between drag modulation (drag increment and reduction) and bubble location. However, the dynamics of large-sized bubbles include some open questions, such as the mechanism of drag modulation, as bubbles of a certain size can increase, rather than decrease, drag, which results in larger skin friction than that under single-phase flow. Accordingly, the goals of the present study are to numerically investigate the above questions and achieve a comprehensive understanding of large-sized bubble dynamics.

This thesis comprises seven chapters, summarized as follows.

1. First, background research on bubbly flow for drag reduction and related numerical studies are briefly described, and the objectives and strategies of the thesis are presented in Chapter 1.

2. The mathematical formulation and numerical details of the volume of fluid (VOF) methods and two different types of interface sharpening methods are presented. Several series of verification works as interface-sharpening methods are confirmed. [Chapter 2].

3. The modeling of a large-sized bubble interface and the vortical structures around the bubble are validated. Before the validation work, the main part to be modeled is divided into three parts, and the procedure of division is described in Chapter 3.

4. The dynamic behavior of the bubble interface and the drag modulation of large-sized bubbles in the turbulent channel flow are investigated by exploring various bubble sizes. The mesh condition of the numerical model is improved to resolve the coherent turbulent structure [Chapter 4].

5. The dynamic behavior of a large-sized bubble on turbulent Couette channel flow is examined to investigate differences such as the deformation mechanism from that of turbulent Poiseuille channel flow [Chapter 5].

6. The large-sized bubbly flow is investigated as a flow condition to explain the drag reduction involved in bubble formation [Chapter 6].

7. Reviews of each chapter and the conclusions of this thesis are presented [Chapter 7].

Contents

Contents

General introduction

Contents

1.1 Turbulent boundary control by bubbly flow

The control of turbulent boundary layers by bubbly flow has been studied for a long time by many researchers to characterize the effects of bubbly flow on heat, mass, and momentum transfers. It has many advantages because the bubbly flow consistently modifies the boundary layer by traveling with the main flow. The characteristics of these bubbly flows change based on the direction of buoyancy relative to the main flow direction; bubbly flows can be categorized as vertical and horizontal to distinguish these characteristics.

Vertical bubbly flows are the predominant objects of study because the buoyancy of the bubbles acts along the streamwise direction, resulting in an obvious difference in the distribution of the void fraction and flow pattern. This phenomenon is important for industrial demands relating to heat exchangers, such as those in nuclear reactors and power plants (Taitel et al., 1980; Tutu, 1982; Bilicki and Kestin, 1987; Hibiki and Ishii, 2002). Bubbles are deformed and fragmented by the shear of the flow and then coalesce through surface tension when they make contact with each other. Moreover, mutual interactions of bubbles exist in bubbly flows, such as bubble–bubble interactions (Kitagawa et al., 2004) and bubble deformation–flow structures (Brücker, 1999; Fujiwara et al., 2004). However, it remains difficult to completely understand the behaviors of such interactions and their effects on bubbly flows owing to multi-scale problems ranging from the thickness of the gas–liquid interface to the length scale of bulk

systems.

Conversely, horizontal bubbly flows have received less attention than vertical bubbly flows because buoyancy acts in the wall-normal direction of the channel such that air bubbles are present on the upper wall, irrespective of the bubble size or void fraction, and thus hinder heat exchange or mass transfer in the system between the liquid phase and the wall. This phenomenon is unsuitable for industrial demands and more complex flows. However, the bubbles can efficiently modify and control the inner-layer structure of the turbulent boundary layer formed beneath a horizontal flat wall through the congregation of bubbles near the wall, which reduces the frictional drag on the wall. This characteristic is called bubble drag reduction (BDR).

Researchers have studied the behavior of bubbles within and their effects on the near-wall turbulent boundary layer for horizontal bubbly flow. In studies on bubble behavior, bubbles smaller than the Kolmogorov length scale have been found to be concentrated in the ejection region between two streamwise vortices and to form bubble chains arranged in the streamwise direction (Harleman et al., 2011). Murai (2014) reported several types of bubble clusters based on the void fraction in horizontal bubbly flows and the Reynolds number defined by the height of the channel. Thus, their behaviors are affected by several parameters associated with the flow. Next, the bubble-induced effects of the turbulent boundary layer were classified into static and dynamic effects. The static effects, usually caused by relatively small bubbles compared with the thickness of the boundary layers, are characterized by modifications in the fluid properties, such as decreased average density and increased effective viscosity (Rust and Manga, 2002; Murai et al., 2008).

Dynamic effects are induced by the modification of vertical flow structures, such as streamwise vortices, in turbulent boundary layers by the fragmentation and deformation of bubbles. The Reynolds shear stress that dominates the skin frictional drag in turbulent flows is reduced by the injected bubbles because of turbulent energy and the modification of the components of velocity fluctuations (Meng and Uhlman, 1989; Kitagawa et al., 2005). Murai (2014) summarized the effects of bubble injection on flow and its contribution to drag reduction in his review paper and created a map of the main effects of bubbles based on their sizes and flow speeds. However, this transition map is incomplete because the effects and their conductivity are influenced by other factors, such as void fraction (Ceccio, 2010), wall roughness (van den Berg et al., 2007), and entrance distance from the bubble injector (Murai et al., 2006; Hara et al., 2011).

1.2 Limitations of the current air lubrication technology

Frictional drag reduction by air injection has been studied for over 40 years and applied to liquid transport in pipelines and ship surfaces in water. It causes no environmental damage, unlike other techniques such as injecting polymers (den Toonder et al., 1997) and surfactants (Ohlendorf et al., 1986), and requires no appendages or modification to the wall surface, unlike riblets (Walsh, 1983), compliant surfaces (Hahn et al., 2002), superhydrophobic surfaces (Fukagata et al., 2006), Lorentz forces (Berger, 2000), deformation of wall surfaces (Endo et al., 2000), spanwise oscillations of the wall (Baron and Quadrio, 1996), and heating of walls (Hossain et al., 2012). The energy efficiency of large vessels is expected to be promoted by reductions in frictional drag, which accounts for 80% of the total drag.

In industrial fields, air injection is referred to as air lubrication technology. Two aspects of drag reduction exist in the methodology, namely based on the air phases of microbubbles and air films, as shown in Fig. 1.1. Drag reduction by microbubbles was first reported by McCormick and Bhattacharyya (1973). Many researchers have since conducted similar experiments on microbubble drag reduction to study the parameter dependency and skin friction reduction process (Madavan et al., 1985; Merke and Deustch, 1992; Kato et al., 1999; Kodama et al., 2000; Gabillet et al., 2002). Meanwhile, Moriguchi and Kato (2002), Kawamura et al. (2003), and Shen et al. (2006) reported that not only "real microbubbles" but also those of some millimeters in size can reduce skin friction; furthermore, no significant bubble size dependency appeared under a high shear rate. Therefore, recent discussion has mainly focused on the role of the deformability of the bubble in reducing the local Reynolds shear stress, as reported by Kitagawa et al. (2005). This means that the bubble is not required to be small, and that a drag reduction mechanism independent of the spherical bubble may occur after the bubble starts to deform.

Conversely, air films have been found to be practically viable in the last two decades (Fukuda et al., 1999; Matsumura et al., 2002; Katsui et al., 2003). These are formed by injecting air into a superhydrophobic surface. The air film physically separates the liquid phase of the flows and the solid wall and thereby interrupts the momentum transfer from the flows to the wall (Fukuda et al., 2000; Mäkiharju et al., 2013). Although the main technical problem is the simple maintenance of a stable air sheet on the target wall, these walls easily break up into large bubbles downstream, owing to the Kelvin–Helmholtz instability. In this case, the bubble size after the film collapse is important in determining the total drag reduction when the streamwise persistence of drag reduction is required, because larger bubbles maintain some drag reduction

capability; however, for those in a particular size range relative to the boundary layer thickness, the drag increases owing to the enhanced turbulent momentum transfer by the bubbles. However, the critical bubble size that maintains drag reduction after the disappearance of the air film has not yet been determined.

This situation applies to both the air film and microbubble methods. Bubbles measuring a few millimeters contained in the microbubble swarm frequently coalesce in the shear layer and become large-sized bubbles in the downstream region. Therefore, it is important to study this range of bubble sizes and investigate the persistence of drag reduction along the streamwise length. Murai et al. (2006) investigated the drag reduction phenomenon for these bubbles (10–50 mm) and observed that calm regions were generated behind the bubbles. This feature differs greatly from that shown by microbubbles. The performance of large-sized bubbles with respect to BDR was later found to depend on the bubble length by Murai et al. (2007), who showed a common spatial relationship between the drag modulation and bubble location. Oishi and Murai (2014) rigorously investigated and described influential characteristics, such as the influential velocity field around the bubble and the instantaneous momentum flux **u'v'** contours related to the drag reduction of a single large-sized bubble. In addition to the velocity gradient in the wake region, it is assumed that the liquid film between the bubbles and the wall also reduces skin friction by relaminarizing the flow in the liquid film. Park et al. (2019) experimentally investigated the relationship between the film thickness and BDR. However, some open questions remain in large-sized bubble dynamics, such as the mechanism of drag modulation, as bubbles of certain sizes cause the increase, rather than decrease, of drag.

<Large-sized bubble in microbubble method>

<Large-sized bubble in air film method>
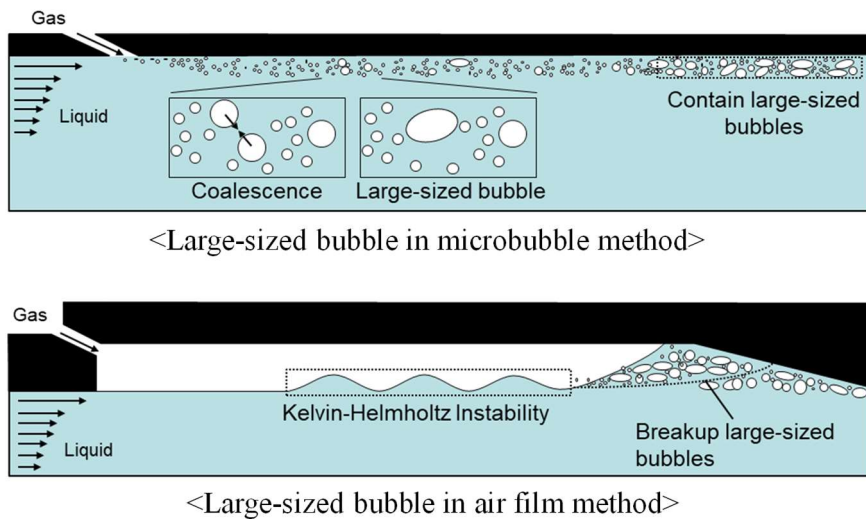
Figure 1.1: Schematic views of air lubrication technologies: (a) microbubble, (b) air film

1.3 Numerical simulations of bubbly flow

Direct numerical simulation (DNS) has played an important role in fully understanding bubbly flow, leading to considerable new insights. Sugiyama et al. (2001) utilized DNS to investigate a multiscale problem in bubbly flows, which ranges from the thickness of the gas–liquid interface to the length scale of the bulk system, to understand bubble behavior. A series of DNSs on vertical bubbly flow were also performed by Lu and Trygvasson, with variations in the type of bubbles, such as spherical and deformable bubbles, as well as flow direction, such as upflow and downflow. They examined turbulent bubbly downflow in the vertical channel with varied numbers of spherical bubbles; they confirmed that the bubbles became concentrated in the core region and verified similar flow characteristics in the wall region as those in single-phase flow, as well as the dependence of turbulent properties on bubble size (Lu and Trygvasson, 2006, 2007). The bubble characteristics for upflow (Lu and Trygvasson, 2008, 2013) confirmed that the spherical bubbles remained close to the wall, whereas deformable bubbles were distributed in the core region of the channel. The velocity fluctuation and vorticity were also enhanced by deformable bubbles and suppressed by spherical bubbles. Recently, they examined the effects of surface tension (Lu and Trygvasson, 2018) and void fraction (Lu and Trygvasson, 2019) on the structure of multiphase flow in a vertical channel.

Conversely, the first DNS study of horizontal bubbly flow was conducted by Kanai and Miyata (2001) on the drag reduction of microbubbles. Kawamura and Kodama (2002) and Xu et al. (2002) confirmed that bubbles reduced the turbulent energy and modified the velocity fluctuation components. Ferrante and Elghobashi (2004) showed by DNS that microbubbles pushed turbulent structures away from walls. Smaller bubbles congregated at the ejection region between two streamwise vortices and formed bubble chains arranged in the streamwise direction, as reported by Nierhaus et al. (2007). In addition, as the discussion progressed from the bubble size to the role of bubble deformability, DNS studies have also confirmed the positive contribution of deformable bubbles to the drag reduction process (Kawamura, 2005; Lu et al., 2005; Sugiyama et al., 2005; Spandan et al., 2017). Subsequently, many researchers (Pang et al., 2014; Zhang et al., 2020; etc.) have performed DNS studies on microbubbles. Meanwhile, the DNS study of large-sized bubbles, in a size regime between those of microbubbles and air films, has not yet been investigated, despite the importance of determining the drag reduction performance from both sides. The large computational resources required to resolve the high deformation of large-sized bubbles with sharp interfaces over a long period have hindered such DNS research.

1.4 Research objective

By summarizing research regarding large-sized bubbles, the current situation is as follows:

1. Large-sized bubbles are important to retain the persistence drag reduction achieved via the microbubble and air film methods. To achieve retention, the characteristics of the large-sized bubbles have been partially investigated experimentally; however, such research is scarce.

2. Based on the observations reported in previous studies, the skin friction trends with bubble size can be predicted, as shown in Fig. 1.2. However, it is not clear why drag increases and decreases with bubbles of different sizes, and the occurrence of drag reduction with large-sized bubbles, as shown by the dotted red line, has not yet been explained in detail.

3. Numerical study may be necessary in clarifying the above points; however, no previous studies of large-sized bubbles exist because of the requirement of massive computational resources to resolve the dynamic interfaces.

In this study, a numerical model suitable for high-performance computing (HPC) was developed. The open-source computational fluid dynamics (CFD) package OpenFOAM has been used by many researchers worldwide to solve various problems in fluid mechanics (Komen et al., 2014) on parallel HPC systems. Because no previous work on the DNS of a horizontal flow with large-sized bubbles was found in the existing literature, a numerical procedure for the injection of large-sized bubbles in turbulent channel flows was established. A series of code verification was required, and validation studies were performed by comparing the simulated results with those of experiments and other DNS results. Accordingly, the goals of the present study were to investigate the above questions numerically, as shown in Fig. 1.2.

1. The sources that cause the drag increase and decrease by bubbles in the millimeter regime as described in (1) of Fig. 1.2.

2. Evidence for determining critical bubble diameter ($d_{cri.}$) near the air film region, as described in (2) of Fig. 1.2.

To explain the answers to the above questions, the behavior of large-sized bubbles in horizontal turbulent channel flow was investigated using the developed DNS model under various conditions, including varied bubble sizes, numbers of bubbles such as single versus multiple conditions, and flow conditions such as Poiseuille versus Couette flow. The steps involved in this thesis are listed below. The generated DNS data can be used for further large-sized bubble modeling to achieve a comprehensive understanding of large-sized bubble dynamics.

1. The numerical solvers for large-sized bubbles were verified by evaluating the numerical diffusion and advection characteristics of an interface, and the numerical model was validated by comparing it with previous experimental results.

2. The characteristics around a single large-sized bubble such as vortical structures, were investigated and identified to examine the cause of increased skin friction and critical bubble size to obtain the parameters related to drag reduction for further studies.

3. A numerical model of the intermediate condition between the channel flow and ship surface flow was established to confirm the characteristics of the interfacial deformation of large-sized bubbles from turbulent Couette flow.

4. The numerical model was extended from a single bubble to bubbly flow, allowing observation of the interactions between bubbles and bubble behavior, as well as quantitative evaluation of drag reduction on large-sized bubbly flows under different flow conditions, such as turbulent Poiseuille and Couette flow.
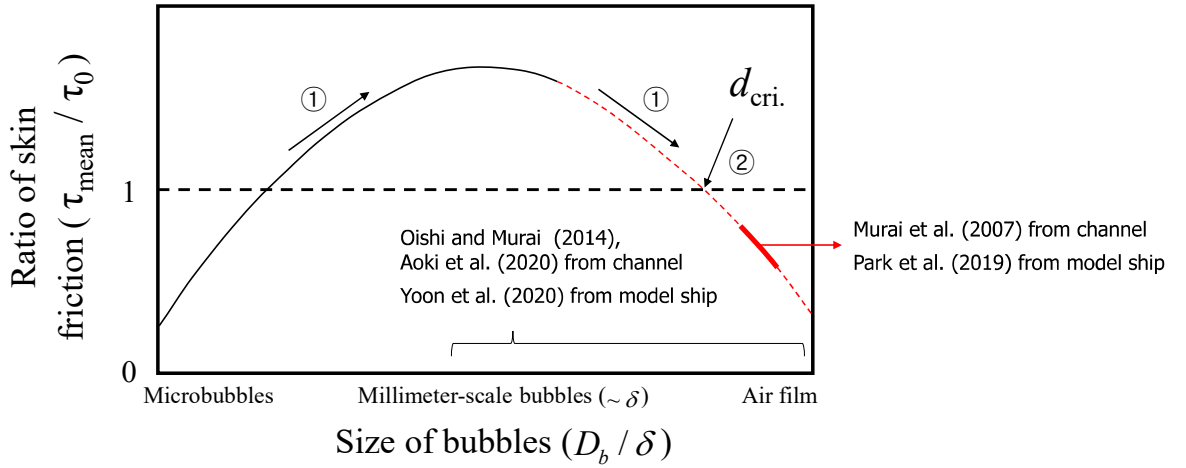
Figure 1.2: Schematic diagram of the skin friction ratio with variations in the diameter of the injected bubbles (Park et al., 2015) to describe previous studies.

1.5 Summary of structures of the thesis

To realize the objective of this study, the study progresses through the stages in each chapter as follows:

In Chapter 2, the mathematical formulation and numerical details are described. To achieve the ultimate goal of modeling large-sized bubble deformation, the author uses the volume of fluid (VOF) method to approach the dynamic motion of the bubble interface influenced by a turbulent flow. Accordingly, the governing equations presented in this chapter can comprise the fundamental conservation equations for mass and momentum under the one-phase model framework. In the case of the interface-sharpening method, the *IsoAdvector* method is introduced as a sub-grid-scale model to estimate the intracellular distribution using the given volume fraction and velocity. This sub-grid-scale model constructs the interface inside the cell and creates sub-cells occupied by each volume fraction. This procedure enables the maintenance of a sharp interface under large deformation conditions. To verify the performance of this method, the most fundamental cases under pure advection of the Rudman-shearing and Rudman–Zalesak solid rotation tests are performed first with a 2-D calculation domain. This provides evidence that the current interface-sharpening method maintains the interface properly under pure advection conditions.

Chapter 3 describes the validation of the numerical models. Before the validation work, the main parts modeled are (1) generation of the turbulent channel flow, (2) location of the large-sized bubble inside the channel, and (3) maintaining the large-sized bubble inside the channel. The procedure for each model is described. Subsequently, the validation results of a large-sized bubble, validation of modeling for large-sized bubble interfaces, and turbulent modulation are presented. The dynamic distribution of instantaneous momentum flux and skin friction on a liquid film is precisely investigated through a comparison with the experiment. Based on the validation, it is concluded that the models for large-sized bubble interfaces and turbulent modulation are qualitatively validated. (This work was published by Kim et al., 2020.)

Consequently, **Chapter 4** shows the dynamic behavior and drag modulation of large-sized bubbles in a turbulent channel flow by exploring various bubble sizes and defining the Weber numbers for different scenarios. In this study, the numerical method for modeling turbulent flow is changed from large-eddy simulation (LES) to DNS to consider the fully resolved boundary layer flow and the interfacial deformation of a large-sized bubble by applying a higher grid resolution than that used in Chapter 3. It is found that the behavior of the bubble interface affects

the drag reduction ratio during its deformation, and this dynamic effect on the drag reduction ratio varies with different Weber numbers. The author observed that the drag contour corresponds to a turbulent flow beginning from the front side of the liquid film. This region is constantly observed although the Weber number increases. In contrast, the absolute value of the skin friction in the spanwise direction is observed to become concentrated on the span edge of the liquid film and then continue to the secondary flow. This trend might not be important for drag reduction in the streamwise direction; however, the instantaneous contours in the spanwise direction show that high skin friction corresponds to this trend in the streamwise direction. The observed skin friction in the spanwise direction is indicated that a high momentum flux occurs in this region. (This work was presented by Kim et al., 2020.)

In **Chapter 5**, by using the same computational configuration as that in Chapter 4, the dynamic behavior of a large-sized bubble in turbulent Couette flow is examined. To generate turbulent Couette flow, the simulation procedure is modified for each stage, modeled with the same frictional Reynolds number as the model described in Chapter 4. The results show that the deformation of the large-sized bubble in turbulent Couette differs from that in turbulent Poiseuille channel flow, with ligament inflation in the case of the one-directional development of the ligament. (This work was presented by Kim and Oshima, 2021.)

In **Chapter 6**, the drag reduction effect on large-sized bubbly flows is investigated under different flow conditions (Poiseuille and Couette flow) to explain the unsteady phenomena involved in the flow conditions and bubble formation. The time-dependent deformation and behavior of large-sized bubbles are visualized together with the frictional drag distribution. Near-zero skin friction contours on the liquid film of the large-sized bubble are observed under both flow conditions when the bubble size approached the film regime. This phenomenon was experimentally predicted and described as the relaminarizing flow in the liquid film; the present numerical model is able to reproduce it.

Finally, in **Chapter 7**, the content in each chapter is reviewed and the conclusions of this thesis are summarized.

References

[1] Tutu, N. K., 1982. Pressure fluctuations and flow pattern recognition in vertical two-phase gas-liquid flows. *Int. J. Multiphase Flow* 8(4), pp. 443-447.

[2] Taitel, Y., Bornea, D., and Dukler, A. E., 1980. Modeling flow pattern transitions for steady upward gas–liquid flow in vertical tubes. *AIChE J.* 26(3), pp. 345-354.

[3] Bilicki, Z., and Kestin, J., 1987. Transition criteria for two-phase flow patterns in vertical upward flow. *Int. J. Multiphase Flow* 13(3) pp. 283-294.

[4] Hibiki, T., and Ishii, M., 2002. Interfacial area concentration of bubbly flow systems. *Chem. Eng. Sci.* 57(18), pp. 3967-3997.

[5] Kitagawa, A., Sugiyama, K., and Murai, Y., 2004. Experimental detection of bubble-bubble interactions in a wall-sliding bubble swarm. *Int. J. Multiphase Flow* 30(10), pp. 1213-1234.

[6] Brücker, C., 1999. Structure and dynamics of the wake of bubbles and its relevance for bubble interaction. *Phys. Fluids* 11(7), pp. 1781-1796.

[7] Fujiwara, A., Danmoto, Y., Hishida, K., and Maeda, M., 2004. Bubble deformation and flow structure measured by double shadow images and PIV/LIF. *Exp. Fluids* 36(1), pp. 157-165.

[8] Harleman, M. J. W., Delfos, R., Terwisga, T. J. C. V., and Westerweel, J., 2011. Dispersion of bubbles in fully developed channel flow. *J. Phys. Conf. Ser.* 318(5), 052007.

[9] Murai, Y., 2014. Frictional drag reduction by bubble injection. *Exp. Fluids* 55(7).

[10] Rust, A. C., and Manga, M., 2002. Effects of bubble deformation on the viscosity of dilute suspensions. *J. Non-Newtonian Fluid Mech.* 104(1), pp. 53-63.

[11] Murai, Y., Oiwa, H., and Takeda, Y., 2008. Frictional drag reduction in bubbly Couette-Taylor flow. *Phys. Fluids* 20(3), 034101.

[12] Meng, J. C. S., and Uhlman, J. S., 1989. Microbubble formation and splitting in a turbulent boundary layer for turbulence reduction. In: Advances in fluid dynamics. *Springer*; New York, pp. 168-217.

[13] Kitagawa, A., Hishida, K., and Kodama, Y., 2005. Flow structure of microbubble-laden turbulent channel flow measured by PIV combined with the shadow image technique. *Exp. Fluids* 38(4), pp. 466-475.

[14] Ceccio, S. L., 2010. Frictional drag reduction of external flows with bubble and gas injection. *Annu. Rev. Fluid Mech.* 42(1), pp. 183-203.

[15] van den Berg, T. H., van Gils, D. P. M, Lathrop, D. P., and Lohse, D., 2007. Bubbly turbulent drag reduction is a boundary layer effect. *Phys. Rev. Lett.* 98(8), 084501.

[16] Murai, Y., Oishi, Y., Takeda, Y., and Yamamoto, F., 2006. Turbulent shear stress profiles in a bubbly channel flow assessed by particle tracking velocimetry. *Exp. Fluids* 41(2), pp. 343-352.

[17] Hara, K., Suzuki, T., and Yamamoto, F., 2011. Image analysis applied to study on frictional drag reduction by electrolytic microbubbles in a turbulent channel flow. *Exp. Fluids* 50(3), pp. 715-727.

[18] den Toonder, J. M. J., Hulsen, M. A., Kuiken, G. D. C., and Nieuwstadt, F. T. M., 1997. Drag reduction by polymer additives in a turbulent pipe flow: numerical and laboratory experiments. *J. Fluid Mech.* 337, pp. 193-231.

[19] Ohlendorf, D., Interthal, W., and Hoffmann, H., 1986. Surfactant systems for drag reduction: Physicochemical properties and rheological behaviour. *Rheol. Acta* 25(2), pp. 468-486.

[20] Walsh, M. J., 1983. Riblets as a viscous drag reduction technique. *AIAA J.* 21(4), pp. 485-486.

[21] Hahn, S., Je, J., and Choi, H., 2002. Direct numerical simulation of turbulent channel flow with permeable walls. *J. Fluid Mech.* 450, pp. 259-285.

[22] Fukagata, K., Kasagi, N., and Koumoutsakos, P., 2006. A theoretical prediction of friction drag reduction in turbulent flow by superhydrophobic surfaces. *Phys. Fluids* 18(5), 051703.

[23] Berger, T. W., Kim, J., Lee, C., and Lim, J., 2000. Turbulent boundary layer control utilizing the Lorentz force. *Phys. Fluids* 12(3), pp. 631-649.

[24] Endo, T., Kasagi, N., and Suzuki Y., 2000. Feedback control of wall turbulence with wall deformation. *Int. J. Heat Fluid Flow* 21(5), pp. 568-575.

[25] Baron, A., and Quadrio, M., 1996. Turbulent drag reduction by spanwise wall oscillations. *Appl. Sci. Res.* 55(4), pp. 311-326.

[26] Hossain, M. Z., Floryan, D., and Floryan, J. M., 2012. Drag reduction due to spatial thermal modulation. *J. Fluid Mech.* 713, pp. 398-419.

[27] McCormick, M. E., and Bhattacharyya, R., 1973. Drag reduction of a submersible hull by electrolysis. Nav. Eng. J. 85(2), pp. 11–16.

[28] Madavan, N. K., Deutsch, S., and Merkle, C.L., 1984. Reduction of turbulent skin friction by microbubbles. *Phys. Fluids* 27(2), pp. 356-363.

[29]Merkle, C.L., and Deutsch, S., 1992. Microbubble drag reduction in liquid turbulent boundary layers. *ASME Appl. Mech. Rev.* 45(3), pp. 103-127.

[30]Kato, H., Iwashina, T., Miyanaga, M., and Yamaguchi, H., 1999. Effect of microbubbles on the structure of turbulence in a turbulent boundary layer. *J. Mar. Sci. Technol.* 4(4), pp. 155-162.

[31]Kodama, Y., Kakugawa, A., Takahashi, T., and Kawashima, H., 2000. Experimental study on microbubbles and their applicability to ships for skin friction reduction. *Int. J. Heat Fluid Flow.* 21(5), pp. 582-588.

[32]Gabillet, C., Colin, C., and Fabre, J., 2002. Experimental study of bubble injection in a turbulent boundary layer. *Int. J. Multiphase Flow* 28(4), pp. 553-578.

[33]Moriguchi, Y., and Kato, H., 2002. Influence of microbubble diameter and distribution on frictional resistance reduction. *J. Mar. Sci. Technol.* 7(2), pp. 79-85.

[34]Kawamura, T., Moriguchi, Y., Kato, H., Kakugawa, A., and Kodama, Y., 2003. Effect of bubble size on the microbubble drag reduction of a turbulent boundary layer. *Proc. ASME/JSME Fluids Eng. Conf. Summer Meeting 2003*, pp. 647-654.

[35]Shen, X., Ceccio, S. L., and Perlin, M., 2006. Influence of bubble size on micro-bubble drag reduction. *Exp. Fluids* 41(3), pp. 415-424.

[36]Fukuda, K., Tokunaga, J., Nobunaga, T., Nakatani, T., Iwasaki, T., and Kunitake, Y., 1999. Frictional drag reduction with air lubricant over super water repellent surface (2nd report) -resistance tests of tanker and high length-to-beam ratio ship models-. *J. Soc. N.A., Japan,* 186.

[37]Matsumura, K., Kaminaga, F., and Saito, H., 2002. Drag reduction on super water repellent surface with air injection method: 2nd report, drag reduction mechanism. *JSME, Trans. B* 68(671) pp. 32-38 (in Japanese).

[38]Katsui, T., Okamoto, Y., Kasahara, Y., Shimoyama, N., Iwasaki, Y., Soejima, S., and Hirayama, A., 2003. A study of air lubrication method to reduce frictional resistance of ship. *J. Kansai Soc. N.A., Japan* 239, pp. 45-53 (in Japanese).

[39]Fukuda, K., Tokunaga, J., Nobunaga, T., Nakatani, T., Iwasaki, T., and Kunitake, Y., 2000. Frictional drag reduction with air lubricant over a super-water-repellent surface. *J. Mar. Sci. Technol.* 5(3), pp. 123-130.

[40]Mäkiharju, S. A., Elbing B. R., Wiggins, A., Schinasi, S., Vanden-Broeck, J. -M., Perlin, M., Dowling, D. R., and Ceccio, S. L., 2013. On the scaling of air entrainment from a ventilated partial cavity. *J. Fluid Mech.* 732, pp. 47-76.

[41] Murai, Y., Fukuda, H., Oishi, Y., Kodama, Y., and Yamamoto, F., 2007. Skin friction reduction by large air bubbles in a horizontal channel flow. *Int. J. Multiphase Flow* 33(2), pp. 147-163.

[42] Oishi., Y., and Murai., Y., 2014. Horizontal turbulent channel flow interacted by a single large bubble. *Exp. Therm. Fluid Sci.* 55, pp. 128-139.

[43] Park, H. J., Tasaka, Y., and Murai, Y., 2019. Bubbly drag reduction investigated by time-resolved ultrasonic pulse echography for liquid films creeping inside a turbulent boundary layer. *Exp. Therm. Fluid Sci.* 103, pp. 66-77.

[44] Sugiyama, K., Takagi, S., and Matsumoto, Y., 2001. Multi-scale analysis of bubbly flow. *Comput. Meth. Appl. Mech. Eng.* 191(6-7), pp. 689-704.

[45] Lu, J., and Tryggvason, G., 2006. Numerical study of turbulent bubbly downflows in a vertical channel. *Phys. Fluids* 18(10), 103302.

[46] Lu, J., and Tryggvason, G., 2007. Effect of bubble size in turbulent bubbly downflow in a vertical channel. *Chem. Eng. Sci.* 62(11), pp. 3008-3018.

[47] Lu, J., and Tryggvason, G., 2008. Effect of bubble deformability in turbulent bubbly upflow in a vertical channel. *Phys. Fluids* 20(4), 040701.

[48] Lu, J., and Tryggvason, G., 2013. Dynamics of nearly spherical bubbles in a turbulent channel upflow. *J. Fluid Mech.* 732, pp. 166-189.

[49] Lu, J., and Tryggvason, G., 2018. Direct numerical simulations of multifluid flows in a vertical channel undergoing topology changes. *Phys. Rev. Fluids* 3(8), 084401.

[50] Lu, J., and Tryggvason, G., 2019. Multifluid flows in a vertical channel undergoing topology changes: Effect of void fraction. *Phys. Rev. Fluids* 4(8), 084301.

[51] Kanai, A., and Miyata, H., 2001. Direct numerical simulation of wall turbulent flows with microbubbles. *Int. J. Numer. Meth. Fluids* 35(5), pp. 593-615.

[52] Kawamura, T., and Kodama, Y., 2002. Numerical simulation method to resolve interactions between bubbles and turbulence. *Int. J. Heat Fluid Flow* 23(5), pp. 627-638.

[53] Xu, J., Maxey, M. R., and Karniadakis, G. E., 2002. Numerical simulation of turbulent drag reduction using micro-bubbles. *J. Fluid Mech.* 468, pp. 271-281.

[54] Ferrante, A., and Elghobashi, S., 2004. On the physical mechanisms of drag reduction in a spatially developing turbulent boundary layer laden with microbubbles. *J. Fluid Mech.* 503, pp. 345-355.

[55] Nierhaus, T., Vanden Abeele, D., and Deconinck, H., 2007. Direct numerical simulation

of bubbly flow in the turbulent boundary layer of a horizontal parallel plate electrochemical reactor. *Int. J. Heat Fluid Flow* 28(4), pp. 542-551.

[56] Lu, J., Fernandez, A., and Tryggvason, G., 2005. The effect of bubbles on the wall drag in a turbulent channel flow. *Phys. Fluids* 17(9), 095102.

[57] Sugiyama, K., Kawamura, T., Takagi, S., and Matsumoto, Y., 2005. Recent Progress of Microbubble Flow Simulation for Elucidating Drag Reduction Mechanism. *Proc. of the 6th Symp. on Smart Control of Turbul.*, pp. 191-202.

[58] Kawamura, T., 2005. Numerical and experimental investigation the mechanism of the microbubble drag reduction. *Proc. 6th Symp. SMART control of turbulence.*

[59] Spandan, V., Verzicco, R., and Lohse, D., 2017. Deformable ellipsoidal bubbles in Taylor-Couette flow with enhanced Euler-Lagrangian tracking. *Phys. Rev. Fluids* 2(10), 104304.

[60] Pang, M. J., Wei, J. J., and Yu, B., 2014. Numerical study on modulation of microbubbles on turbulence frictional drag in a horizontal channel. *Ocean Eng.* 81, pp. 58-68.

[61] Zhang, X., Wang, J., and Wan, D., 2020. Euler–Lagrange study of bubble drag reduction in turbulent channel flow and boundary layer flow. *Phys. Fluids* 32(2), 027101.

[62] Komen, E., Shams, A., Camilo, L., and Koren, B., 2014. Quasi-DNS capabilities of OpenFOAM for different mesh types. *Comput. Fluids*, 96, pp. 87-104.

[63] Aoki, R., Park, H. J., Tasaka, Y., and Murai. Y., 2020. Design of bubble splitter device for drag reduction of vessels by bubble injection. *Proc. Fluid Eng. Div.,* 2020.

[64] Yoon, D. I., Park, H. J., Tasaka, Y., Murai, Y., 2020. Characteristics of bubble behavior inside boundary layers beneath a tilted plate. *Proc. Fluid Eng. Div.,* 2020.

[65] Park, H. J., Tasaka, Y., Oishi, Y., and Murai, Y., 2015. Drag reduction promoted by repetitive bubble injection in turbulent channel flows. *Int. J. Multiphase Flow* 75, pp. 12-25.

[66] Kim, S. W., Oshima, N., Murai, Y., and Park, H. J., 2020. Numerical investigation of a single intermediate-sized bubble in horizontal turbulent channel flow. *J. Fluid Sci. Technol.* 15(3).

[67] Kim, S. W., Oshima, N., Murai, Y., and Park, H. J., 2020. Direct numerical simulation for drag reduction effect of a single intermediate-sized bubble, *Proc. Fluid Eng. Div.,* 2020.

[68]Kim, S. W., and Oshima, N., 2021, Numerical flow visualization of large-sized bubble in turbulent Couette channel flow using OpenFOAM, *Proc. 19th* Int. *Sym. On Flow Visualization*.

Numerical approach

Contents

Preface

The aim of this chapter is to present and compare several numerical methods for achieving numerical simulations of large-sized bubbles. The evaluation of effective phase advection based on two famous cases of Rudman–shearing and Rudman–Zalesak solid rotation testing, were performed, and the characteristics of interface compression were compared. The selected method was universally used in this thesis.

2.1 Introduction

This section introduces the numerical method used in the present study. The development of HPCs has enabled the application of DNS in a broad range of research. Recently, various open-source codes have been made available online that can be employed in our studies with proper modifications. These codes can shorten development time and even surpass some of the in-house code with code quality and regular maintenance. Among these open-source codes, OpenFOAM is a widely used finite-volume method written in C++, originally developed by Imperial College London. The biggest advantage of OpenFOAM is that it has the largest user group of the available open-source codes; its reliability has been proven by many researchers worldwide, demonstrating its convenience for use. Therefore, we developed a numerical model based on this method.

2.2 Governing equations

The flow condition was assumed to be an unsteady, turbulent, incompressible, and isothermal two-phase flow. The fluids were assumed to have no mass transfer across the interface. The governing momentum and continuity equations are presented in Equations (2.1) and (2.2), respectively.

$$\frac{\partial \rho \mathbf{u}}{\partial t} + \rho \nabla \cdot (\mathbf{u}\mathbf{u}) = -\nabla p + \nabla \cdot \mathbf{T} + \rho \mathbf{f} + \mathbf{f}_{\sigma} \qquad (2.1)$$

$$\nabla \cdot \mathbf{u} = 0 \qquad (2.2)$$

where ρ is the fluid density, t is the time, $\mathbf{u}$ is the velocity vector, p is the pressure, $\mathbf{T}$ is the viscous stress tensor, $\mathbf{f}$ is the body force, which include gravity and the averaged pressure gradient for the pressure driving force in the streamwise direction in the case of Poiseuille flow, and $\mathbf{f}_{\sigma}$ is the surface tension force.

2.3 Volume-of-fluid (VOF) method

The volume-of-fluid (VOF) method, a one-fluid approach, was used to model the two-phase flow in this study. This approach requires the solving of a single momentum equation for both phases, as shown in equation (2.1), and the volume fraction α is introduced in the continuity equation, as shown in equation (2.3).

$$\frac{\partial \alpha}{\partial t} + \nabla \cdot (\alpha \mathbf{u}) = 0 \qquad (2.3)$$

The volume fraction α represents the proportion of one of the two fluids to the total amount of fluid, and the density is defined by the mathematical average, as shown in equation (2.4):

$$\rho = \alpha \rho_1 + (1 - \alpha)\rho_2 \qquad (2.4)$$

where ρ_1 and ρ_2 represent the first (water) and second (air) phase densities, respectively, and α denotes the volume fraction of the water phase. The viscosity μ can be defined similarly. Generally, α in equation (2.3) requires a special method to prevent smearing into neighboring regions while simultaneously remaining between 0 and 1.

2.3.1 Advantages of the VOF method compared to other methods

Figure 2.1 shows different two-phase modeling classes and their prominent methods (Mirjalili et al, 2017). VOF is one of the classes of interface-capturing approaches in one-fluid models, which are currently of great interest in the research community. In this section, the advantages of VOF are compared with those of several methods of the one-fluid model.

The first is the front-tracking method (Tryggvason et al., 2011), which is a class of interface-tracking approaches; it introduces additional computational points to track the interface advected in a Lagrangian method, along with the two-phase interface, which allows for a highly accurate interface representation. This method is best suited for well-defined interfaces that are easily detectable in the initial condition and remain as such for the entire simulation.
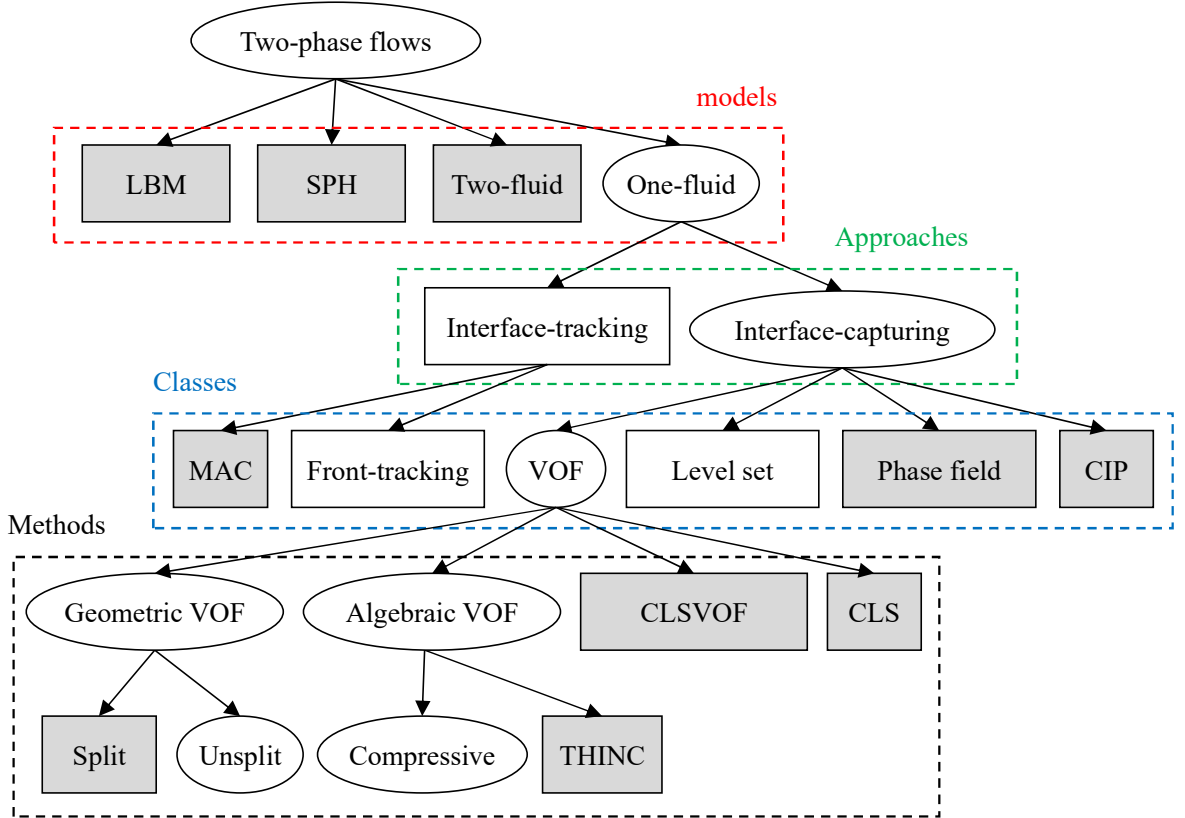
Figure 2.1: Classification of numerical methods for two-phase flows (Mirjalili et al., 2017). The VOF methods employed in this study are enclosed in ellipses. The methods that are compared with the VOF methods have white backgrounds, while the others have gray backgrounds. Abbreviations: LBM: Lattice Boltzmann Method; SPH: Smoothed-Particle Hydrodynamics; MAC: Marker-And-Cell; CIP: Constrained Interpolation Profile (Yabe et al., 2001); CLSVOF: Coupled Level-Set and VOF method (Sussman and Puckett, 2000); CLS: Conservative Level-Set (Olsson et al., 2007); THINC: Tangent of Hyperbola INterface Capturing (Xiao et al., 2005)

In the front-tracking method, large deformation, breakup and coalescence of bubbles require nontrivial algorithms of point redistributions, additions, or eliminations. These procedures also add further steps to the total computations. Compared with the front-tracking method, the Eulerian framework of the VOF method allows the handling of large deformations and topological changes without requiring additional numerical algorithms. This simply results in a different indicator field distribution whenever bubble coalescence or breakup occurs. This is a significant advantage of the VOF method for simulating large-sized bubbles that frequently show large deformations at the interface.

The level-set method follows the same approach as the VOF method, where the indicator field is replaced by the signed distance function from the interface. In the volume fraction field, the VOF method varies abruptly from one phase to the other because it is a numerical approximation of the Heaviside function at the interface. In contrast, the distance function of the level-set method varies smoothly across the interface, which simplifies the advection algorithm of the level-set function. Furthermore, the curvature field from the derivatives of the indicator function of the level-set method leads to a more accurate evaluation of the curvature than the VOF method. These advantages of the level-set method, such as the less complex advection algorithm and supposedly accurate computation of the surface tension, have led to its popularity; the level-set method has often been adopted instead of the VOF method.

However, the distance function advected in the level-set method is prone to high-frequency aliasing errors (Sharen et al., 2005) which deteriorate the convergence with grid refinement and leads to erroneous curvature values. Furthermore, the level-set method is not mass-conserving; mass conservation must be implemented by a periodic reinitialization of the distance function. Meanwhile, the VOF method conserves mass by construction. This is a crucial point for addressing the long-period calculation of bubbly flow and the relatively large area of the interface of large-sized bubbles.

2.3.2 Algebraic VOF with the interface compression method

Algebraic VOF methods are probably one of the oldest classes of interface capturing methods. The first of the VOF-type methods (Hirt and Nichols, 1981) computes the fluxes algebraically without the need for geometric reconstruction of the interface. In this chapter, the algebraic VOF method based on the interface compression method is employed. The interface compression method uses the orientation of the interface relative to the cell face. In this subsection, the

interface compression method is derived. The VOF equation in equation (2.3) can be distinguished in two fluids, as shown in equations (2.5) and (2.6):

$$\frac{\partial \alpha_l}{\partial t} + \nabla \cdot (\alpha_l \mathbf{u}_l) = 0 \tag{2.5}$$

$$\frac{\partial \alpha_g}{\partial t} + \nabla \cdot (\alpha_g \mathbf{u}_g) = 0 \tag{2.6}$$

where α_l and α_g are the volume fractions of the liquid and air phases, respectively. It is sufficient to consider the evolution in time of one of the two volume fractions, such as liquid-phase α_l advected by liquid-phase velocity $\mathbf{u}_l$; the velocity at the interface is assumed to be equal to the total velocity $\mathbf{u}$ for maintaining a sharp interface.

However, the sharp interface scenario is not accurate, because the interface is always smeared out over a few computational cells. This phenomenon is controlled by an additional compression term and is derived as follows. First, the total velocity $\mathbf{u}$ in each cell is defined as the effective velocity by the weighted average, as shown in equation (2.7):

$$\mathbf{u} = \alpha_l \mathbf{u}_l + \alpha_g \mathbf{u}_g \tag{2.7}$$

and the relative velocity $\mathbf{u}_r$ is:

$$\mathbf{u}_r = \mathbf{u}_l - \mathbf{u}_g \tag{2.8}$$

Adding equation (2.7) multiplied by α_l to equation (2.8) multiplied by $\alpha_l(1 - \alpha_l)$, we obtain equation (2.9).

$$\alpha_l \mathbf{u}_l = \alpha_l \mathbf{u} + \alpha_l(1 - \alpha_l)\mathbf{u}_r \tag{2.9}$$

Inserting (2.9) into equation (2.5) yields

$$\frac{\partial \alpha_l}{\partial t} + \nabla \cdot (\alpha_l \mathbf{u}) + \nabla \cdot [\alpha_l(1 - \alpha_l)\mathbf{u}_r] = 0 \tag{2.10}$$

The third term is the interface compression term, which is a similar function to the sharp interface for the level-set approach proposed by Olsson et al. (2007) and is only activated in the vicinity of the interface because of the product $\alpha_l(1 - \alpha_l)$. Thus, this term partially compresses the interface, which is insufficiently sharp, and smearing it over a few cells. Meanwhile, the

relative velocity $\mathbf{u}_r$ is not available from the one-fluid approach, which solves for the total velocity $\mathbf{u}$. The numerical implementation of the relative velocity at the cell faces is based on the maximum velocity magnitude at the interface region and its direction, as determined from the gradient of the phase fraction, as follows:

$$(\mathbf{u}_r)_f = \min\left(c_r \frac{|\phi|}{|S_f|}, \max \frac{|\phi|}{|S_f|} \right)(\mathbf{n}_f \cdot S_f) \qquad (2.11)$$

where ϕ and S_f are the volume flux from face $\mathbf{u}_f \cdot S_f$ and the cell-face-oriented area, respectively, and c_r is a user-specified value to control the intensity of the interface compression. Model (2.11) relies on the definition of $\mathbf{u}_r$; if the velocities of both phases are of the same order of magnitude, the constant c_r controls the intensity of the additional term in equation (2.10).

For all simulations, this value was chosen as $c_r = 1$ following the recommendation of the OpenFOAM user guide because a value of c_r considerably lower than 1 indicates excessive smearing out from the interface, whereas a constant c_r greater than 1 distorts the interface, yielding inaccurate advection or undesirable interfacial features, which may cause numerical instability. The magnitude of $(\mathbf{u}_r)_f$ is bounded to the maximum face velocity in the flow field, and its direction is aligned with the normal to the interface $\mathbf{n}_f$, calculated at the cell faces in the interface region using the phase fraction gradient at the cell faces, as follows:

$$\mathbf{n}_f = \frac{(\nabla f)_f}{|(\nabla f)_f + \delta_n|} \qquad (2.12)$$

where δ_n is the stabilization factor. Equation (2.10) is solved explicitly by a flux limiter implemented by the multidimensional universal limiter solver (*MULES*), which is designed to preserve the boundedness of the volume fraction independent of the mesh topology and the numerical scheme of the convective terms.

2.3.3 Geometric VOF with unsplit (*IsoAdvector*) method

The transport equation of volume fraction α in equation (2.4) is solved using the *IsoAdvector* geometric VOF scheme (Roenby et al., 2016), which can capture extremely sharp interfaces. It was implemented to overcome the drawbacks of the interface compression method, such as inaccurate advection and undesirable features on the interface owing to the additional compression term. This method implements new concepts for the reconstruction and advection of the interface.

For the reconstruction step, efficient isosurface calculations are used to compute the distribution of fluids in each cell. For the advection step, the physical time step is divided into sub-time steps, such that the flux of α through a cell face can be calculated analytically, assuming that the interface moves steadily across the field during the interval.

As shown in Fig. 2.2, the detailed procedure for constructing an interface can be summarized as follows: (1) The surface cells that contain a volume fraction ranging from $0 < \alpha < 1$ are found, as shown in Fig. 2.2(a). (2) The volume fraction of a vertex of the surface cells from all surrounding cells is interpolated, as shown in Fig. 2.2(b). (3) The face–interface intersection points between the two vertices are calculated. Subsequently, as shown in Fig. 2.2(c), the interface is constructed from the intersection points and lines in the surface cell. (4) As shown in Fig. 2.2(d), the cell is split, and the volume fraction is redistributed such that the sub-cells occupy either $\alpha = 0$ or 1. (5) Velocity field data are used to estimate the interface motion during the time interval.
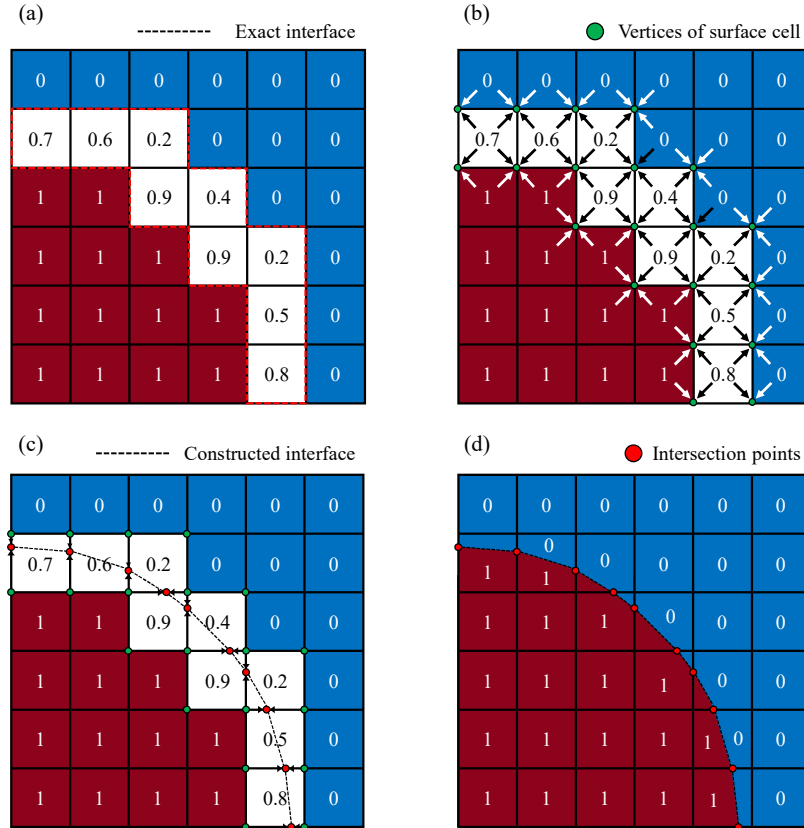

Figure 2.2: Schematic procedure of the *IsoAdvector* method. (a) Surface cells (white) selected based on the exact interface. (b) Volume fraction of vertices from the centroid values around the cells is interpolated. (c) Interface is constructed based on the intersection points, which are calculated between the two vertices. (d) The volume fraction is distributed to the sub-cells.

2.4 Validation work for the interface tracking method

2.4.1 2D Rudman-shearing and Rudman–Zalesak solid rotation tests

To demonstrate the performance of the interface capturing method, the Rudman-shearing and Rudman–Zalesak solid rotation tests (Rudman, 1998) were conducted, as shown in Fig. 2.3. The results obtained using *IsoAdvector* and the conventional method, that is, *MULES*, were compared. The numerical conditions retained the resolution of the grid (800 × 800, physical dimensions 1 m × 1 m) while maintaining an interface Courant–Friedrichs–Lewy (CFL) number below 0.4.

In the Rudman–Zalesak solid rotation test, a slotted disk was rotated around the center of the computational domain with two revolutions. The shape obtained by *MULES* is severely distorted on the upper side of the disk, whereas the shape obtained by *IsoAdvector* preserves the original shape other than a slight deformation in the high-curvature regions. In the Rudman-shearing test, a disk was sheared clockwise to stretch a long filament during the first half-period by a spiraling flow.

The filament was then sheared again counter-clockwise until the end of the period, when it merged into the original disk. This situation is similar to a real problem with stretching, shearing, fluid merging, and breakup. The shape obtained by *MULES* is severely deformed in a zigzag manner from the long filament, and the left and right sides of the disk are scattered into small parts when merging into the original disk. In contrast, using *IsoAdvector* preserves the shape much better. Thus, it is expected that the *IsoAdvector* method would be more suitable for further research, such as the DNS of large-sized bubbles.

2.4.1 2D interface compression test

Rudman-shearing tests and the Rudman–Zalesak solid rotation tests are generally used to demonstrate the performance of the interface capturing method (Roenby et al., 2019; Wang et al., 2019); however, the performance of interface compression, which is important in suppressing the smearing fraction, has not been evaluated. Two verification tests were conducted. The initial and boundary conditions are shown in Fig. 2.4. The two solvers of *interFoam* with implemented *MULES* and *interIsoFoam* with *IsoAdvector* were used.

The resolution of the mesh was 100 × 100, and the time step was set to maintain the interface CFL number below 0.4. The region where $0 < \alpha < 1$ is assumed to be near the bubble interface

with smearing occurring towards the water region. The results were compared to evaluate the compression of the interface using both methods. Figure 2.5 shows time sequences of simulations (left to right) obtained with *IsoAdvector* and *MULES*, and the two methods are compared with a static initial condition to investigate the behavior of the two methods in the pure compression of this region.

Both methods entailed the displacement of the volume fraction of neighboring cells to occupy either $\alpha = 0$ or 1. However, the two methods differed in the compression speed. *IsoAdvector* quickly solved the displacement of the volume fraction and the smeared region ($0 < \alpha < 1$) disappeared at $t = 0.1$ s, whereas *MULES* gradually compressed the smeared region but did not complete the compression until $t = 1.5$ s.

Based on these results, we can deduce that the sub-grid model of *IsoAdvector* suppresses the smeared region and even accelerates the compression by displacing the volume fraction to the face, where volume fractions of either $\alpha = 0$ or 1 are assigned.
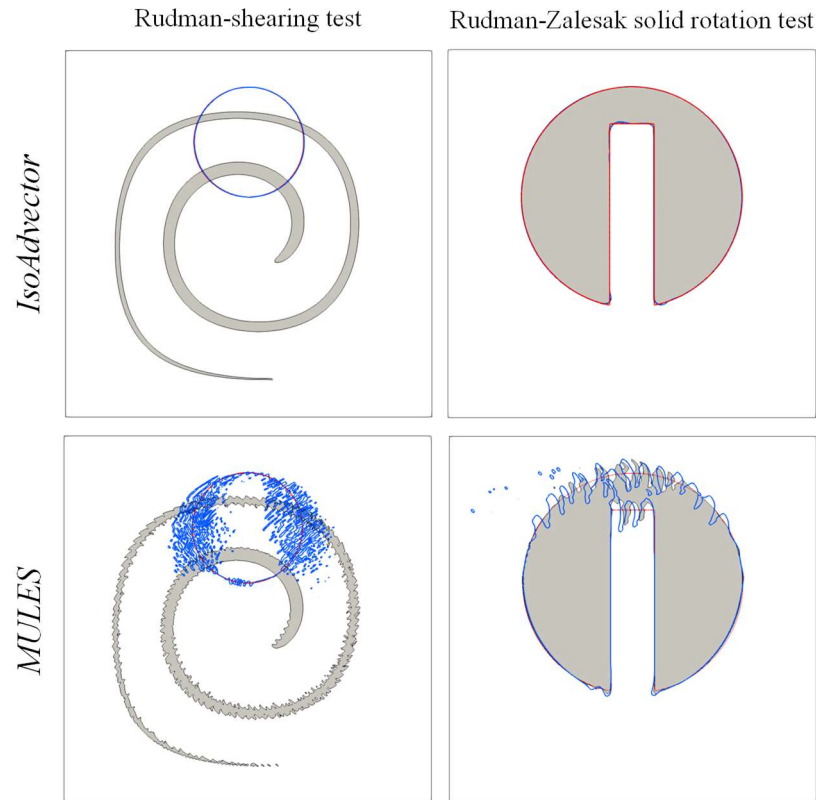
Figure 2.3: Rudman-shear test and Rudman–Zalesak solid rotation test results. The red and blue lines represent outlines of initial and final shapes, respectively. The grey contours indicate the shape after half of a period in the case of the Rudman-shear test and that after one period in the case of the Rudman–Zalesak solid rotation test.

Thus, the verification tests showed that the *IsoAdvector* method not only improved the shape but also suppressed the smeared region ($0 < \alpha < 1$) faster, facilitating better study of the evolution of large-sized bubbles and to prevent smearing at the interface of the bubble. This characteristic of the *IsoAdvector* is suitable for directly calculating the solution. It is expected that the *IsoAdvector* method is more affordable for further studies, such as the DNS of large-sized bubbles.
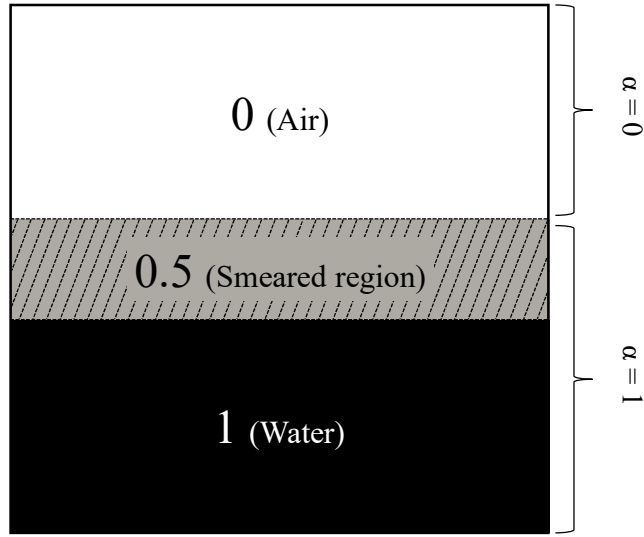
Figure 2.4: Schematic representation of the numerical domain. The wall boundary condition as presented on the right side generates initial fluctuation from the static condition.
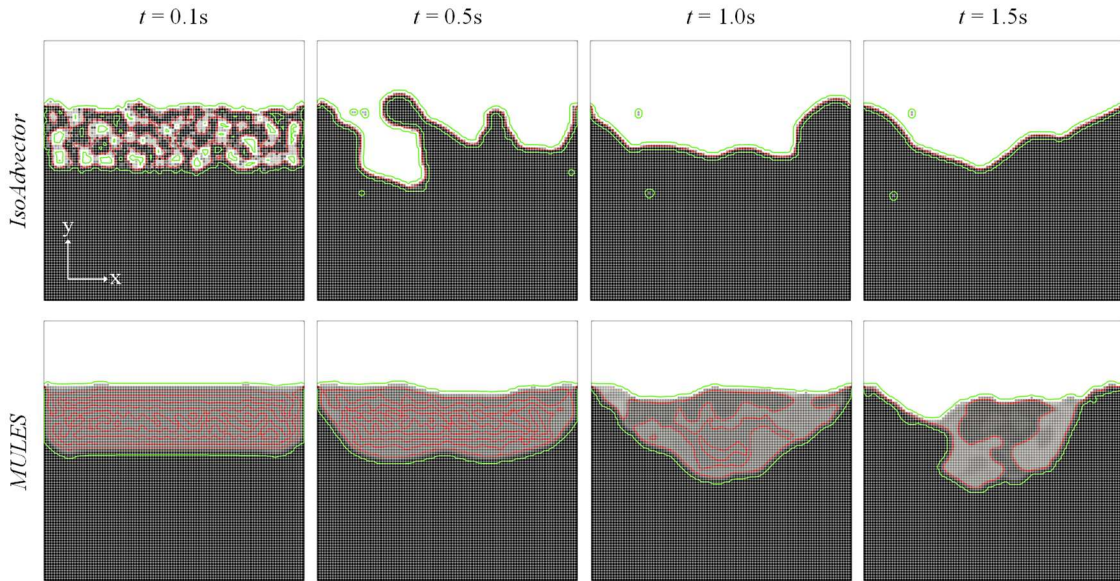
Figure 2.5: Static ($x = 0$, $y = 0$) flow conditions for 0.1 s $\leq t \leq$ 1.5 s; the volume fractions are shown in grey. The contours of $\alpha = 0.5$ are shown in red, and the contours of $\alpha = 0.01$ and 0.99 are shown in green.

2.5 Verification on HPC performance of current solver

In this section, the parallel computational performance is discussed. The hardware utilized for computation is "Fugaku", located at the RIKEN Center for Computational Science. Fugaku is the first ARM architecture-based exascale supercomputer, which comprises 158,976 compute nodes. Each node has 48 ARM processors (A64FX, 48 cores) and 32 GiB memory; the nodes are interconnected by Tofu Interconnect D.

In domain decomposition, the load balance of each computational core and the total number of communication faces should be considered. The parallel strong scalability of the current numerical solver was tested on the Fugaku platform, as shown in Fig. 2.6. The number of nodes varied from six to 48, and the speedup was calculated using the reference performance of each node. Under the condition of the present mesh size (30 million cells), the solver shows a linear or even superlinear speedup at six nodes.
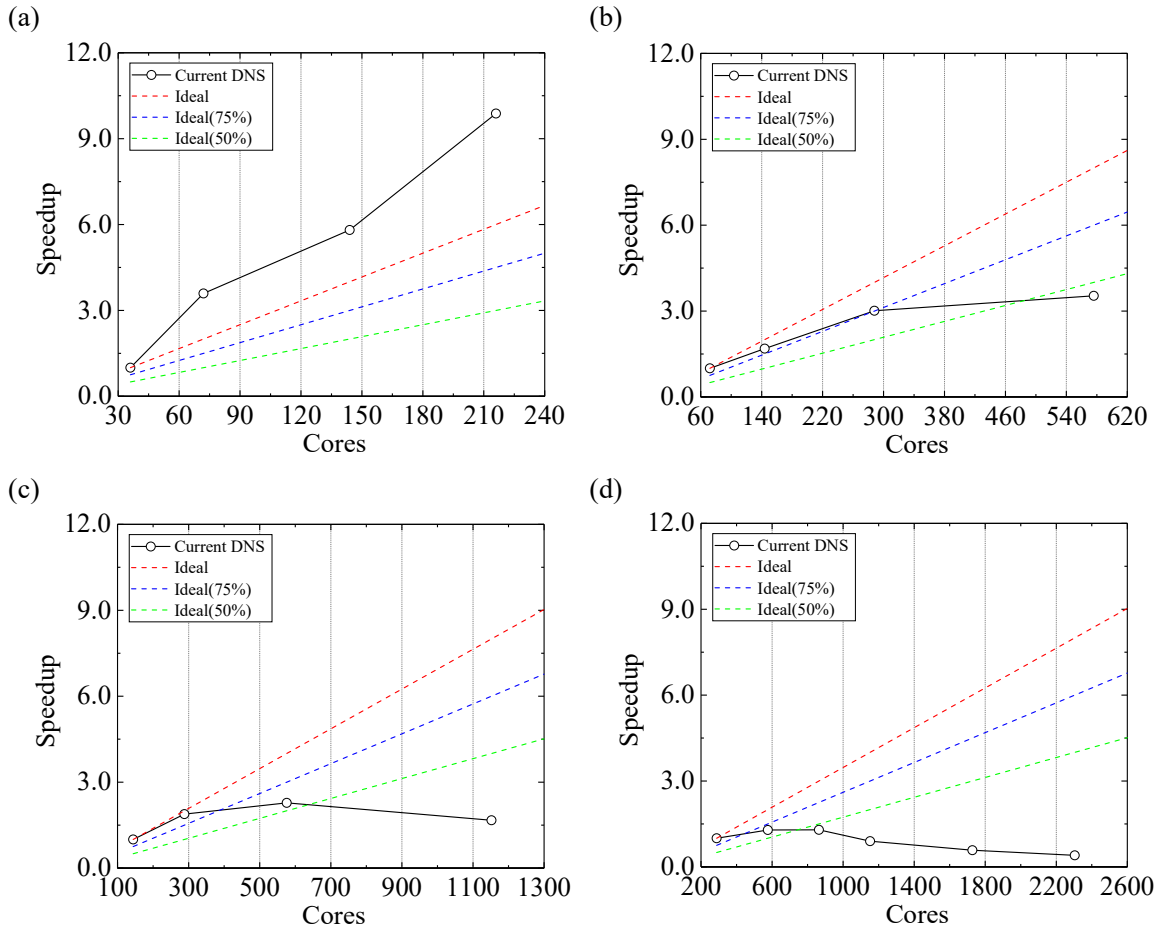
Figure 2.6: HPC performance of current DNS case (30 million cells) with: (a) 6 nodes, (b) 12 nodes, (c) 24 nodes, (d) 48 nodes.

However, the speedup ratio gradually decreased as the number of nodes increased. Thus, a considerable speedup was determined up to 1000 cores, at which point the speedup gradient becomes negative, as shown in Fig. 2.7. With the current decomposition method, the number of cores used is not guaranteed to occupy a full number of cores on a single computational node in Fugaku, owing to the relatively small size of the memory. Thus, the solver should be tuned for the hybrid parallel method (OpenMP and MPI) to use all available cores in the computational node.
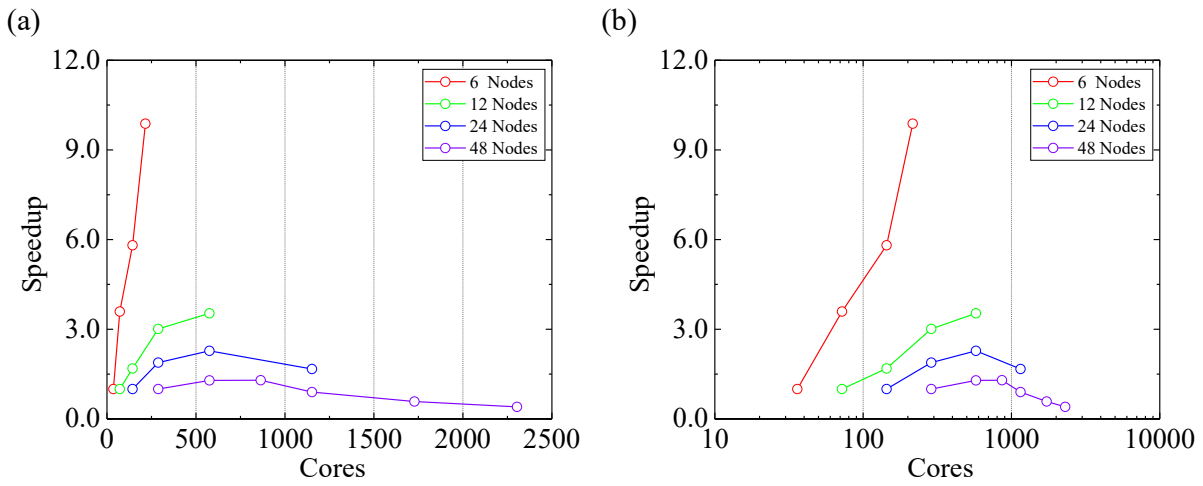
Figure 2.7: Comparison of HPC performance for current DNS case (30 million cells) as a function of the number of nodes.

References

[1] Mirjalili, S., Jain, S., Dodd, M., 2017. Interface-capturing methods for two-phase flows: an overview and recent developments, *Center for Turbulence Research, Annual Research Briefs,* pp. 117-135.

[2] Tryggvason, G., Scardovelli, R., and Zaleski, S., 2011. Direct Numerical Simulations of Gas–Liquid Multiphase Flows. *Cambridge: Cambridge University Press*.

[3] Yabe, T., Xiao, F., and Utsumi, T., 2001. The constrained interpolation profile method for multiphase analysis. *J. Comput. Phys.* 169(2), pp. 556-593.

[4] Olsson, E., Kreiss, G., and Zahedi, S., 2007. A conservative level set method for two phase flow II. *J. Comput. Phys.* 225(1), pp. 785-807.

[5] Sussman, M., and Puckett, E.G., 2000. A coupled level set and volume-of-fluid method for computing 3D and axisymmetric incompressible two-phase flows. *J. Comput. Phys.* 162(2), pp. 301-337.

[6] Xiao, F., Honma, Y., and Kono, T. 2005. A simple algebraic interface capturing scheme using hyperbolic tangent function. *Int. J. Numer. Methods Fluids* 48(9), pp. 1023-1040.

[7] Sharen, J.C., Marianne, M.F., and Douglas, B.K., 2005. Estimating curvature from volume fractions. *Comput. Struct.* 83(6), pp. 425-434.

[8] Roenby, J., Bredmose, H., and Jasak, H., 2016. A computational method for sharp interface advection. *R. Soc. Open Sci.* 3(11), 160405.

[9] Rudman, M., 1998. A volume-tracking method for incompressible multifluid flows with large density variations, *Int. J. Numer. Meth. Fluids* 28(2), pp. 357-378.

[10] Wang, Z., Yan, W., Liu, K. W., Liu, M., 2019. Powder-scale multi-physics modeling of multi-layer multi-track selective laser melting with sharp interface capturing method. *Comput*. Mech. 63(4), pp. 649-661.

Flow field around a single large-sized bubble in turbulent channel flow

Contents

Preface

At present, no study exists on the numerical simulation of large-sized bubbles in horizontal channels for drag reduction, as mentioned in **Chapter 1,** because of the numerical diffusion of the conventional method and the high deformability of the bubbles. In this chapter, we establish the numerical procedure by dividing it into three stages to minimize numerical errors. Using with the numerical results, we validate the accuracy of the solver by comparison with experiments. This work was previously published in Kim et al., *J. Fluid Sci. Technol.* (2020).

Abstract

Air lubrication systems have gained considerable popularity as a promising drag reduction technology in recent years. However, numerical simulations of large-sized bubbles are quite challenging because of the numerical diffusion of the conventional method and the high deformability of the bubbles. This hinders the study of the physical mechanisms involved in a variety of phenomena in such types of bubbles, such as the bubble–liquid interaction effect, high bubble deformation, and flow in the liquid film generated above the bubble. In this study, a solver, *viz. interIsoFoam* of *OpenFOAM*, which is directly captured by the improved volume of fluid method, was applied to solve the gas–liquid interface problem. We established the numerical procedure by dividing it into three stages and validating the accuracy of the given solver to minimize numerical errors such as smearing the volume fractions. The numerical results for variables such as the bubble shape, the skin friction of the liquid film, and the instantaneous momentum flux display trends similar to those observed in the experiments. The calculated bubble shows high skin friction in the secondary flow, which corresponds to the distribution of streamwise vortices in the secondary flow.

3.1 Introduction

To address the increasing concern regarding global warming, the International Maritime Organization (IMO) regulated the requirements regarding greenhouse gas emissions from ships. To reduce these emissions, air lubrication systems are being used as this is an energy-saving technology developed to adhere to industry requirements (ABS, 2019). Air lubrication systems can be divided into two main categories based on the size of the bubbles.

One category is the microbubble method developed by McCormick and Bhattacharyya (1973), and the other is the air film method, which has been found to be practically viable in the last two decades (e.g., Fukuda et al., 1999, 2000). Meanwhile, large-sized bubbles have recently attracted significant research interest, as bubble deformation plays a key role in the process of drag reduction, as studied by Moriguchi and Kato (2002) and Kitagawa et al. (2005). The large-sized bubbles negatively contribute to the drag reduction performance in the downstream region of the microbubble and air film methods. However, Murai et al. (2006) investigated the drag reduction mechanism for these bubbles (10–50 mm) and discovered that a calm region is generated behind the bubble. This feature is quite different from those of the microbubble and air film methods.

This previous research has proven to be a turning point in studies related to large-sized bubbles and is being considered as a new technique for improving drag reduction. An additional advantage is that supplying large-sized bubbles is much easier than generating a high flow rate of microbubbles or stabilizing an air film over a wide area. Murai et al. (2007) and Oishi and Murai (2014) rigorously investigated and described influential characteristics such as the velocity gradient and $u'v'$ contours related to the drag reduction of a single large-sized bubble. In numerical studies, Lu et al. (2005), Sugiyama et al. (2005), Kawamura (2005), and Spandan et al. (2017) also confirmed the positive role of deformable bubbles in the process of drag reduction. Although the deformability of the bubbles is considered to significantly affect the drag reduction in large-sized bubbles, the above studies are confined to small bubbles or microbubbles, while no research has been conducted on large-sized bubbles.

In this study, we established a numerical procedure for the injection of large-sized bubbles in turbulent channel flows. Subsequently, the behavior of these bubbles was investigated to verify that the numerical results followed the experimental trends.

3.2 Characteristics of large-sized bubbles

The large-sized bubbles have sizes between those of microbubbles and air films. Although the definition of the size of the bubble is not a specific size of bubbles, it ranges from medium to large. The definition of this range depends on the authors, for instance, 10–90 mm by Murai et al. (2006), 2–90 mm by Murai et al. (2007), and 6.7–15.5 mm by Oishi and Murai (2014). Figure 3.1 shows a large-sized bubble migrating to the right side with the liquid flow, where τ_w/τ_0 is the local skin friction ratio. Murai et al. (2007) described the bubble characteristics as follows. (1) The large-sized bubbles considerably reduce the local skin friction ratio during their passage. (2) The skin friction on the liquid film gradually decreases from the front to the rear of the bubbles, regardless of their size. (3) The skin friction after the passage of the bubbles increases and oscillates significantly. large-sized bubbles also face a limitation in terms of the drag reduction performance because they generally show a negative performance, as shown in Fig. 3.2. It can be observed that the skin friction ratio decreases when the size of bubbles becomes equal to that of a microbubble or an air film. Meanwhile, the skin friction of some bubbles in the intermediate region exceeds that of the single-phase flow.

The large-sized bubbles are included in this region, which indicates that the inclusion of these bubbles should be avoided. It is important to understand the reason for the increase in the skin friction to obtain a stable drag reduction performance. As depicted in Fig. 3.1, it can be assumed that the secondary flow causes an increase in the average skin friction. In numerical simulations, the spatial relationship between the local skin friction and the vortical structures of the secondary flow has been investigated.
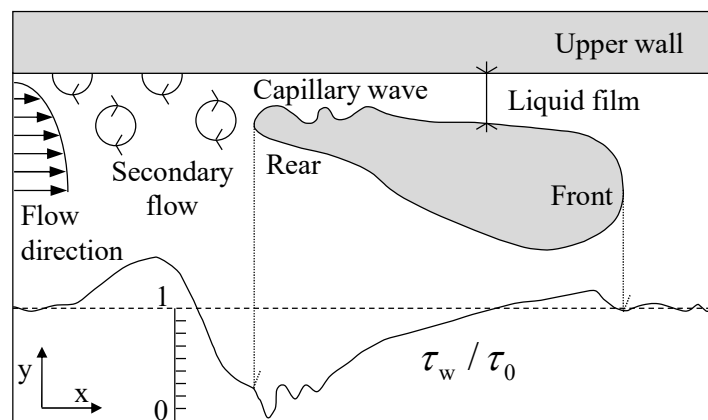
Figure 3.1: Characteristics of the large-sized bubble. Mainly divided into liquid film, capillary wave, and secondary flow, where τw and $\tau 0$ are the local skin friction and the mean skin friction of single-phase flow (Murai et al., 2007).
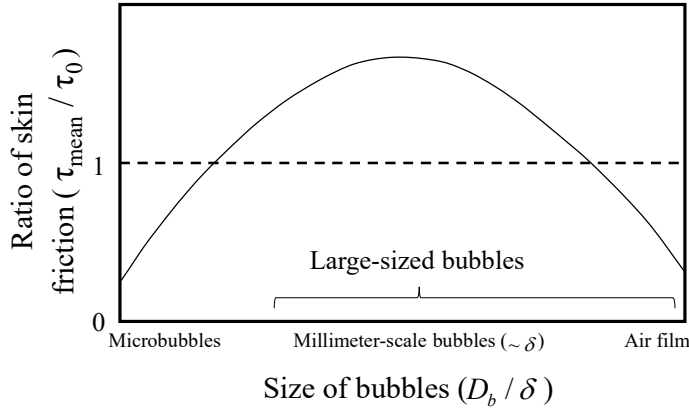
Figure 3.2: Schematic representations of the skin friction ratio as the diameter of bubble (D_b) normalized by boundary layer thickness (δ), which is modified by bubble injection (Park et al., 2015).

3.3 Numerical setup and conditions

In this study, the computations were performed using the open-source CFD software OpenFOAM® version 1812. This code is based on cell-center finite-volume discretization, and the key components of the finite-volume method are the spatial interpolation and time integration schemes. Some of the discretization schemes and models are presented to aid the understanding of the forthcoming analysis in this subsection, as described in Table 3.1. The time discretization scheme specifies how the time derivative $\partial/\partial t$ is handled in the momentum equations. In this study, the *Backward* scheme corresponds to a second-order accurate backward-differencing scheme that utilizes the current and two previous time-steps, and it can be expressed by equation (3.1).

$$\frac{\partial}{\partial t}(\phi) = \frac{1}{\Delta t}(\frac{3}{2}\phi - 2\phi^o + \frac{1}{2}\phi^{oo}) \tag{3.1}$$

where ϕ is the field variable and ϕ^o and ϕ^{oo} are the field variables in two previous time-steps. The global time step is 10^{-5} s for satisfying the Courant-Friedrichs-Lewy (CFL) condition that the CFL number is below 1 and the interface CFL number is below 0.4. Divergence schemes specify how the convective terms are handled in equations (2.1) and (2.2). In this study, total variation diminishing (TVD) schemes were used to calculate the face value by utilizing combined upwind and central differencing schemes, as shown in equation (3.2).

$$\phi_f = (1 - \Gamma)\phi_{f,UD} + \phi_{f,CD} \tag{3.2}$$

where ϕ_f is an approximation of the face-averaged field value, $\phi_{f,UD}$ is the upwind estimate of ϕ_f, and ϕ_{CD} is the central differencing estimate of ϕ_f. Γ is the blending factor, which is a function of variable r representing the ratio of successive gradients, as shown in equation (3.3).

$$r = 2\frac{\boldsymbol{d} \cdot (\nabla \phi)_P}{\phi_N - \phi_P} \qquad (3.3)$$

in the above equation, ϕ_P and ϕ_N are the approximations of the face-averaged field value at the cell center P and the neighbor cell center N; $\boldsymbol{d}$ is the vector connecting the cell center P and the neighbor cell center N. The definition of Γ changes according to the TVD scheme. The momentum flux is handled by the *limitedLinear* scheme, in which the blending factor is calculated using equation (3.4), where k is the input provided by the user. In this study, k was 0.1. The mass flux was handled by the *vanLeer* scheme, which calculates the blending factor using equation (3.5).

$$\Gamma = \max[\min(2r/k, 1), 0] \quad \text{for } \textit{limitedLinear} \qquad (3.4)$$

$$\Gamma = (r + |r|)/(1 + |r|) \quad \text{for } \textit{vanLeer} \qquad (3.5)$$

In the case of the gradient and Laplacian terms, a *Gaussian linear* scheme was used. The turbulence model was large eddy simulation (LES) with the dynamic one-equation eddy-viscosity model as a subgrid-scale model. Pressure-velocity coupling was treated by *Pimple* algorithms that combine the pressure implicit with splitting of operators (PISO) and semi-implicit method for pressure-linked equations (SIMPLE) algorithms.

Table 3.1 Base setup of Numerical scheme and model.

	Scheme/Model
Time discretization scheme	*Backward*
Divergence schemes	Gauss *limitedLinear,* Gauss *vanLeer*
Gradient schemes	Gauss *linear*
Laplacian schemes	Gauss *linear corrected*
Pressure-velocity coupling	*Pimple* Algorithm
Turbulence model	Large eddy simulation
Subgrid-scale model	Dynamic one equation eddy-viscosity model

The numerical condition was constructed based on the experiment of Oishi and Murai (2014), as shown in Table 3.2. In addition, the geometrical configuration of the computational domain is presented in Fig. 3.3. The dimensions of the domain were 10 mm height ($2h$), where h is the half-height of the channel, 75 mm width and 200 mm length between the two horizontal walls. The length and width of the channel were made shorter than in the experiment by using periodic boundary conditions in the stream and spanwise directions. The mean velocity in the current simulation was slightly modified to maintain the same friction velocity (u_τ), and all dimensionless numbers were calculated from the single-phase flow.

Table 3.2 Numerical condition based on experiment.

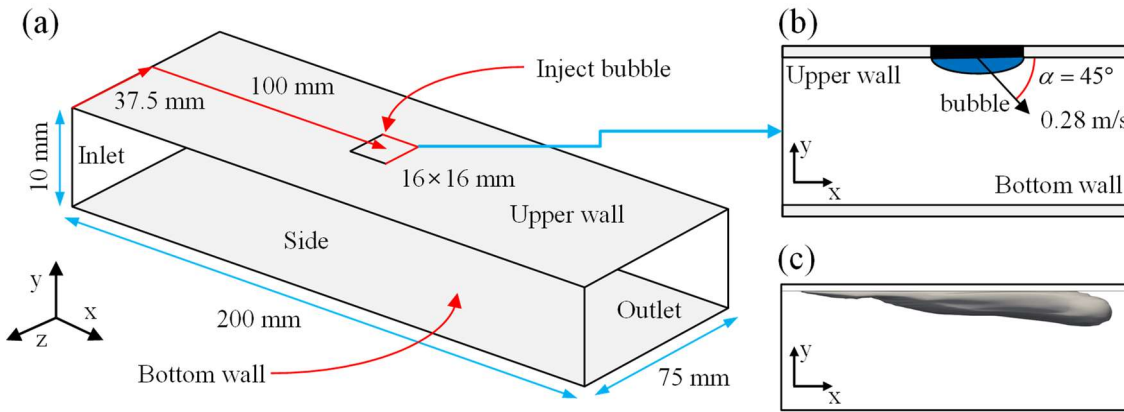| Channel	Experiment	Present CFD	Constant properties	
Size [mm]	$6000 \times 10 \times 100$	$200 \times 10 \times 75$	Fluid	Water [17 °C]
U_{mean} [m/s]	1.0	1.06	ρ [kg/m^3]	998.7
$Fr = U_{mean}/(2hg)^{0.5}$	3.19	3.37	v [m^2/s]	1.08×10^{-6}
$Re = U_{mean}2h/v$	9260	9783	$Re_\tau = u_\tau h/v$	260

Figure 3.3: (a) Computational domain and boundary conditions. (b) Schematic representation of the injection condition. (c) The numerical result of the bubble injection.

3.4 Calculation process

In this study, the procedure of the numerical simulation was divided into three stages, which are as follows. (1) Generation of turbulent channel flow, (2) injection of large-sized bubbles, and (3) maintaining turbulent channel flow with the injected large-sized bubble, as shown in Fig. 3.4. The reason for the division of the total simulation is that the computational domain with periodic conditions is a closed system.

In this system, some inlet conditions, such as the injection of bubbles without the outlet condition, can cause continuity error. Table 3.3 describes the solvers and boundary conditions for each stage. Two solvers distributed with *OpenFOAM®* version 1812 were employed. *PimpleFoam* is a large time-step transient solver for incompressible flow using the *Pimple* algorithm. In this study, this solver was used for turbulent channel flow in stage 1.

InterIsoFoam is a modified version of the solver *interFoam*, which is a solver for incompressible, immiscible, and isothermal two-phase flows using the VOF method for stages 2 and 3. In *interIsoFoam*, the *IsoAdvector* method is implemented for interface capturing instead of *MULES*. At the inlet and outlet, periodic conditions, also called *cyclic* conditions, were applied to the coupling condition between them. This coupling was treated implicitly using the cell values adjacent to each pair of cyclic boundaries with the same topology. For all simulations, the *cyclic* condition was used on the side boundaries.

At the bottom and top walls, the *NoSlip* condition was utilized to set the velocity to zero. In stage 2, the *Codestream* was used to temporarily establish the injection condition on the top. This tool is a dictionary entry that contains the C++ OpenFOAM code that is compiled to generate the entry itself. The *ConstantAlphaContactAngle* condition was additionally applied in stage 3 to ensure that the bubble was detached from the wall and prevented the dispersion on the walls.

Table 3.3 Boundary conditions and solvers in each stage.

	Stage 1		Stage 2		Stage 3
Solver	*PimpleFoam*	→	*InterIsoFoam*		
Inlet	*Cyclic*	→	*Fixedvelocity* (1.06m/s, 0, 0)	→	*Cyclic* (Inlet ↔ Outlet)
Outlet	(Inlet ↔ Outlet)	→	*InletOutlet*	→	
Side			*Cyclic* (Left ↔ Right)		
Bottom	*NoSlip*	→	*NoSlip*	→	*NoSlip,*
Top		→	*NoSlip* , *Codestream* (Inject)	→	*ConstantAlphaContact Angle* (1°)
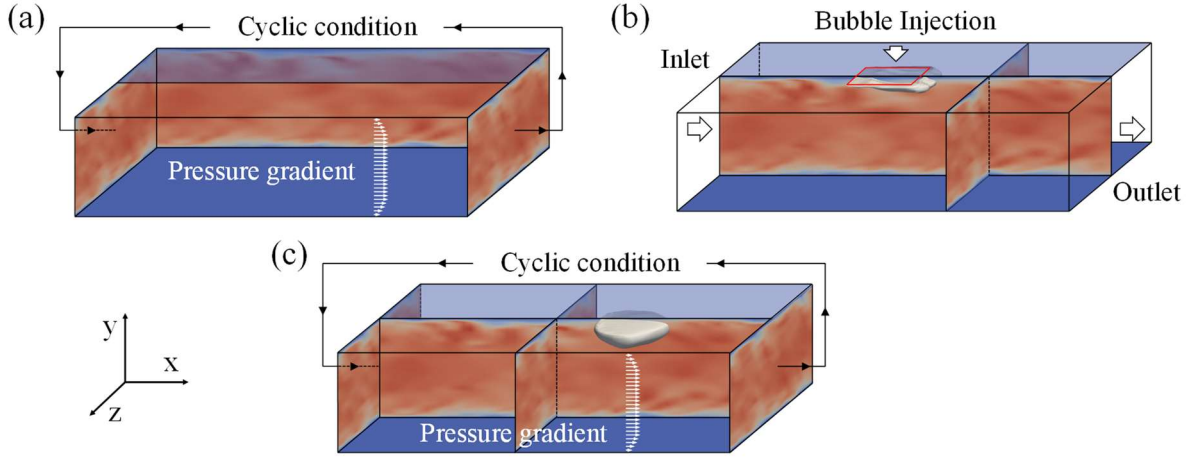
Figure 3.4: The process of generating turbulent channel. (a) Generation of turbulent channel flow. (b) Injection of large-sized bubble. (c) Maintaining turbulent channel flow with the injected large-sized bubble.

3.4.1 Fully developed turbulent channel flow

In stage 1, a fully developed boundary layer was prepared in the channel. The flow was driven in the whole region by a pressure gradient calculated to create a mean velocity of 1.06 m/s. The grid resolution parameters used in this study are provided in Table 3.4. The dimensionless thickness in each direction (Δx^+, Δy^+, Δz^+) is defined as:

$$\Delta x^+ \equiv \frac{u_\tau \Delta x}{v}, \quad y^+ \equiv \Delta y^+ \equiv \frac{u_\tau \Delta y}{v}, \quad \Delta z^+ \equiv \frac{u_\tau \Delta z}{v} \tag{3.6}$$

here, Δx, Δy, and Δz denote the thickness of a mesh-layer in each direction. Meanwhile, Δy is the distance between certain points in the normal direction and the wall for the dimensionless distance from the wall, y^+. Figure 3.5 shows the mean velocity profile and turbulence ratio in each direction and the Reynolds shear stress, which were normalized by the friction velocity.

As the mean velocity was modified for the current simulation, the velocity profile below y^+ = 20 was well resolved but showed a slight deviation beyond that point. This phenomenon is similar to that of turbulent fluctuations, where u' and v' showed deviations after y^+ = 20. From these properties, it can be considered that the current mesh conditions were well resolved in the viscous sublayer and the buffer layer. However, the mesh was not sufficiently refined to resolve it accurately in the log-law region. Despite this, the overall trend of $u'v'$, which is one of the important indicators for estimating large-sized bubble effects, followed the experimental results reasonably well.

Table 3.4 Numerical parameters of computational domain.

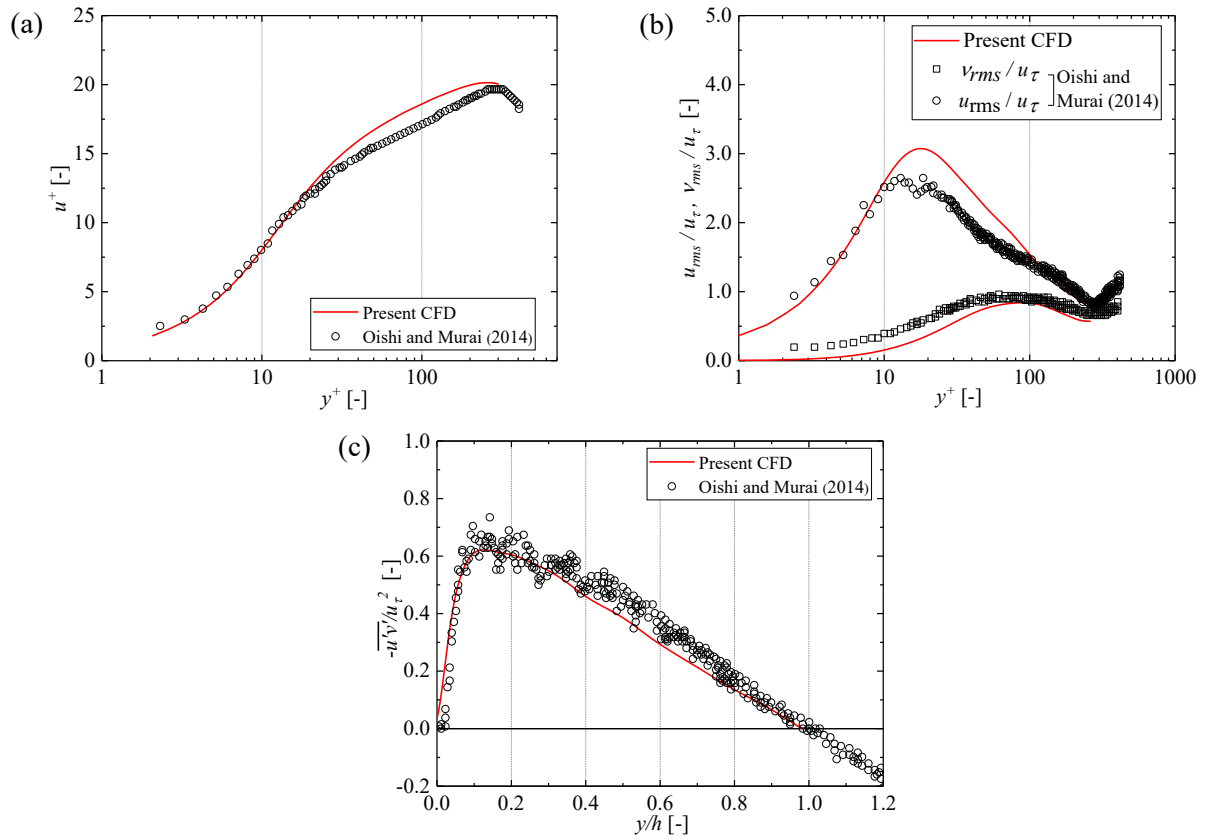|	Size [mm]	Δx^+, Δy^+ and Δz^+	No. of cell
Streamwise	0.494	38.52	405
Spanwise	0.893	46.48	84
Normal	0.032–0.256	0.83–6.69	92
Total no. of cell	6,259,680 ($\approx$ 6.26 M)		

Figure 3.5: Comparison of turbulent properties between the simulation and the experiment results. (a) Mean velocity. (b) Turbulence intensities. (c) Reynolds shear stress.

3.4.2 Large-sized bubble injection in the channel flow

In stage 2, the injection condition on the top was implemented by *Codestream*, as shown in Fig. 3.3(b). A uniform injection velocity was set up for 0.28 m/s to maintain the interface CFL number below 0.4. The angle between the *x*-axis and the injection direction was set to 45° to safely inject the bubble.

The *cyclic* condition in inlet and outlet condition was switched to *Fixedvelocity* condition temporarily to avoid the continuity error in the closed system as described the stage 2 in Table 3.3. In addition, the gravitational acceleration acted downward in the normal direction in order to gain buoyancy. Consequently, the bubble was injected, and its shape was maintained successfully, as shown in Fig. 3.3(c).

3.4.3 Stabilization of large-sized bubble in the channel flow

In stage 3, the bubble was tried to float successfully in the channel. In this stage, volume fractions with the value $\alpha = 0.99$ (referred to as noise fractions in this study) were observed, as shown in the left panel in Fig. 3.6(a). In the case of these noise fractions in front of the bubble, this noise fraction remained in the wake region when the bubble made a lap around the computational domain because of the *cyclic* condition between the inlet and outlet.

When the noise fractions were stuck on the upper wall, such as the red fraction in the left panel in Fig. 3.6(a), the skin friction ratio, which was in the range of $0 - 1$, corresponded to the location of the noise fraction, as shown in the right panel in Fig. 3.6(a). In addition, this resulted in nonphysical values of variables such as pressure and velocity, and was considered to be a specific error for the *IsoAdvector* method. These noise fractions mostly escaped from the rear parts of the bubble in the initial stage before the interface stabilized.

Therefore, the *SetFields* utility was used, which is an auxiliary tool for *OpenFOAM* and is used to set the values of the fields in specific regions. By setting these volume fractions to $\alpha = 1$, the abnormal skin friction was removed, as shown in the right panel in Fig. 3.6(b). A small number of noise fractions remained, but they had no effect on the skin friction when these fraction values existed throughout the channel without stuck noise on the upper wall, such as the green fraction values in the left panel of Fig. 3.6(b).
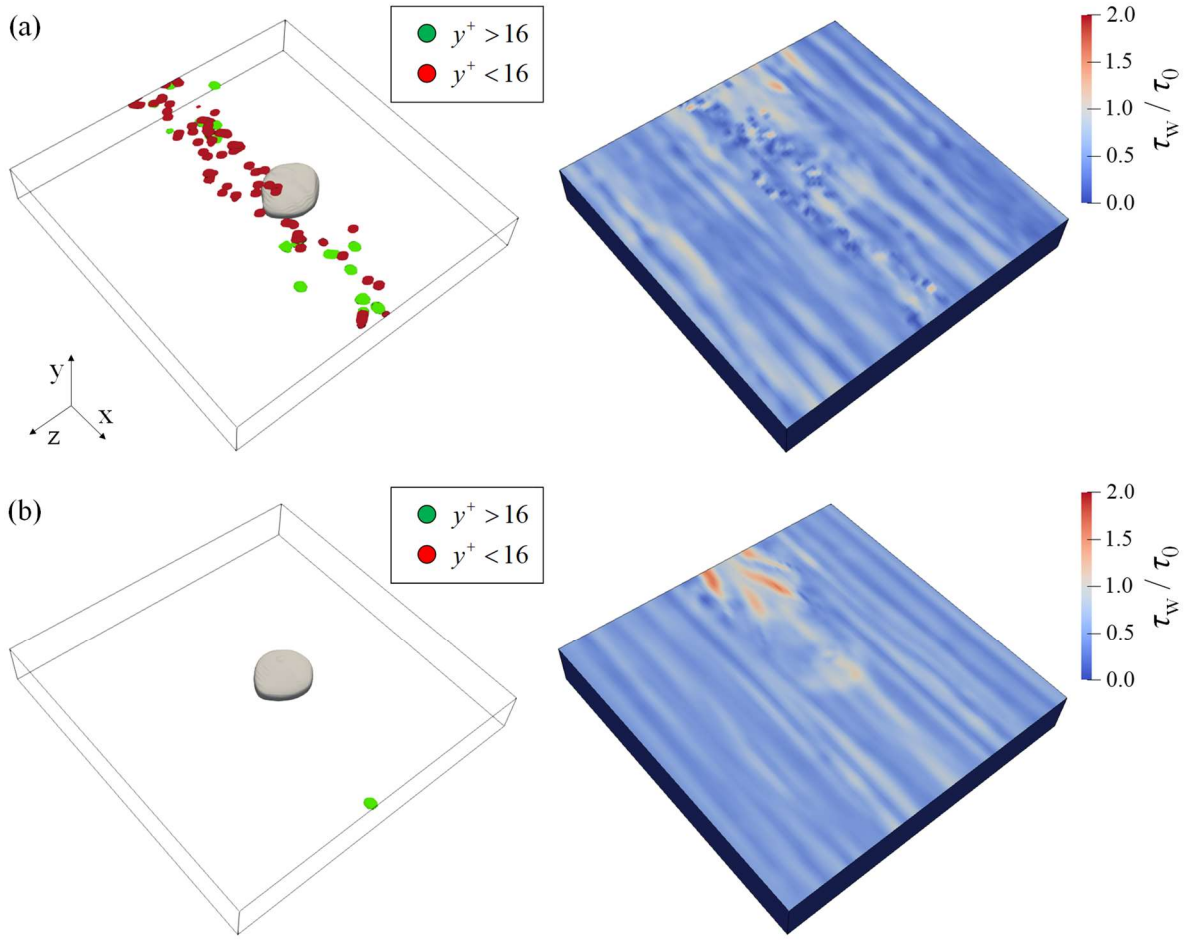
Figure 3.6: Iso-surface of $\alpha = 0.99$ and contours of the skin friction ratio (a) before using *setFields*, (b) after using *setFields*. Iso-surfaces are divided into two categories; near the upper wall ($y^+ < 16$) and main flow layer ($y^+ > 16$).

3.5 Numerical results of large-sized bubble characteristics

3.5.1 Bubble shape and flow field around the interface

In this study, the numerical results were verified to check whether the trends were similar to those of the experiments. The first part was compared with the experimental results of parameters such as the bubble shape, instantaneous momentum flux, and skin friction from Oishi and Murai (2014). Table 3.5 lists the physical parameters of the present bubble. In the table, the diameter is calculated using the bubble volume obtained from the numerical simulation. In both the experiment and the present study, the Weber numbers are similar, with minor differences. The bubble velocity in the current study was 4.7% higher than that in the experiment owing to the modification of the mean velocity. The normalized bubble velocity is similar in both cases, which shows that the simulation result matches the experimental trends. However, the

equivalent diameter of the bubble in the simulation was approximately 34% smaller than that in the experiment. Hence, some trends such as the bubble shape, skin friction, and the development of the liquid film are expected to vary.

Figure 3.7 shows the trajectories of the bubble centroid. Here, T_1–T_4 were selected from the trajectories shown in Fig. 3.7 to compare the parameters at constant time intervals. The trajectory in the streamwise direction increases steadily and is similar to the approximated trajectory calculated from the bubble velocity in the experiment [see Fig. 3.7(a)]. When viewed from the trajectory in the spanwise direction, it shows a constant state. The dimensionless amplitude which is normalized by the equivalent diameter from $t = 1.7$ s to 4.2 s reached approximately 0.1 [see Fig. 3.7(b)]. In addition, it is observed that the bubble bounces in the normal direction and converges to $y/h = 1.4$. However, the dimensionless amplitude is smaller than that in the spanwise direction [see Fig. 3.7(c)]. From the results of the trajectory in each direction, it is concluded that the bubble in this simulation assumes a quasi-steady state. Figure 3.8 presents the evolution of the bubble shape in T_1–T_4, and the fluctuation of the capillary wave of the upper surface is observed to be the same as that in the experiment.

The bubble shape of the top view gradually approaches the experimental result, and the bottom of the bubble stretches to the same position as that reached by the bubble in the experiment. However, the trend in the shape of the bubble from the side view differs from that in the experiment, as shown in the side view in Fig. 3.8. For instance, the front side of the bubble tilts less on the *x*-axis as compared to that in the experiment. In addition, the bubble shape is close to a compressed spheroid in the normal direction than the bubble shape in the experiment, and the direction of the capillary wave seems to be different between experiments and numerical calculations. This is because the effect of the surface tension enhanced by the *IsoAdvector* method and the coarse mesh resolution in the stream and spanwise directions neglected the extensional deformation and capillary wave. Thus, the investigation of these factors will be carried out in future studies.

To compare the evolution of the bubble in T_1–T_4, the shape factors are described in Table 3.6. The shape factors that were calculated based on the parameters l_1, l_2, b, and Δ_{film}, are defined in T_1 in Fig. 3.8. On one hand, l_1/l_2 approaches the experimental results, and the difference between the simulation and the experiment is approximately 1–3%, except at T_1. On the other hand, l_1/b and l_2/b show larger ratios as compared to the value in the experiment and the differences in both the shape factors reach 25–43% relative to that of l_1/l_2. The reason is that l_1

and l_2 are larger than those in the experiment. In addition, the thickness of the liquid film occupies approximately 11% of the bubble height, while the thickness of the liquid film in the experiment was approximately zero. Thus, it is inferred that the bubble shape in the stream and spanwise direction is affected to a greater degree by its physical parameters such as the Weber number as compared to the bubble shape in the normal direction, even if the volumes of the bubble in the simulation and experiment are different.

Table 3.5 Physical parameters of the present bubble.

	Weber number $(\mathrm{We} = \rho U_b^2 D_{\mathrm{equiv.}}/\sigma)$	Equivalent Diameter $(D_{\mathrm{equiv.}})$ [mm]	Bubble velocity	
			U_b [m/s]	U_b/U_{mean}
Present CFD	168	9.6	1.11	1.05
Oishi and Murai (2014)	175	11.0	1.06	1.06
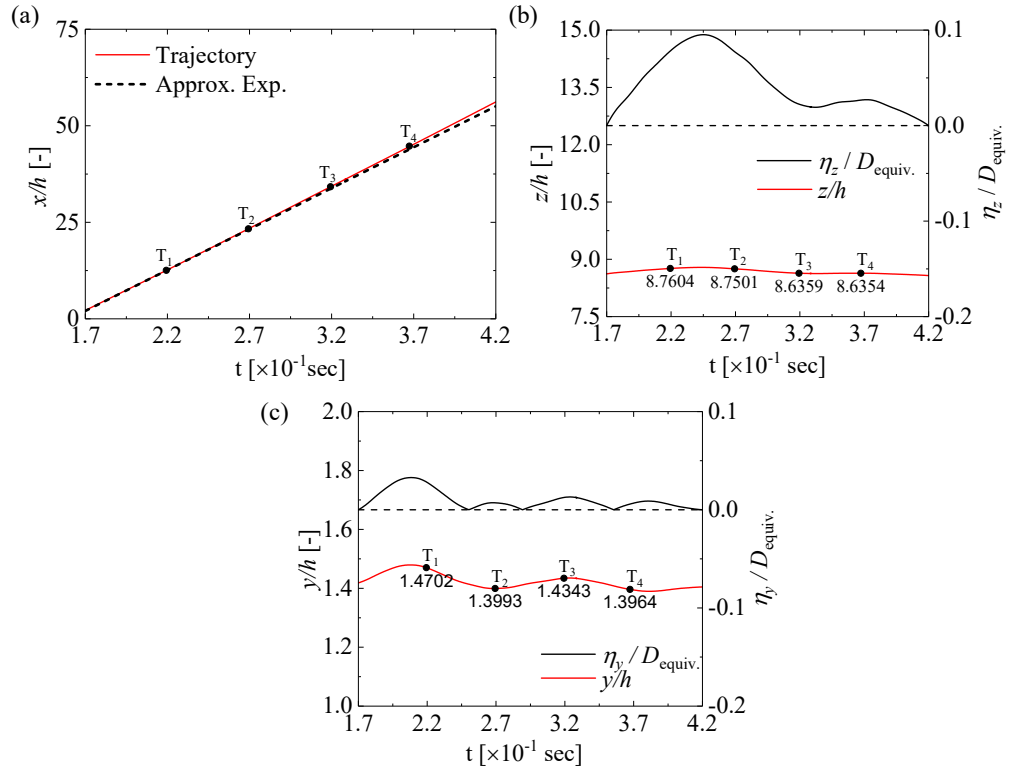
Figure 3.7: Trajectories of the bubble centroid in each direction (Red lines) and the selected points T_1–T_4. (a) Streamwise direction. Black dotted line is approximated by the velocity of the experiment. (b) Spanwise direction. The amplitude in spanwise direction (η_z) normalized by the equivalent diameter ($D_{\mathrm{equiv.}}$) is presented. (c) Normal direction. The amplitude in normal direction (η_y) normalized by the equivalent diameter ($D_{\mathrm{equiv.}}$) is presented.
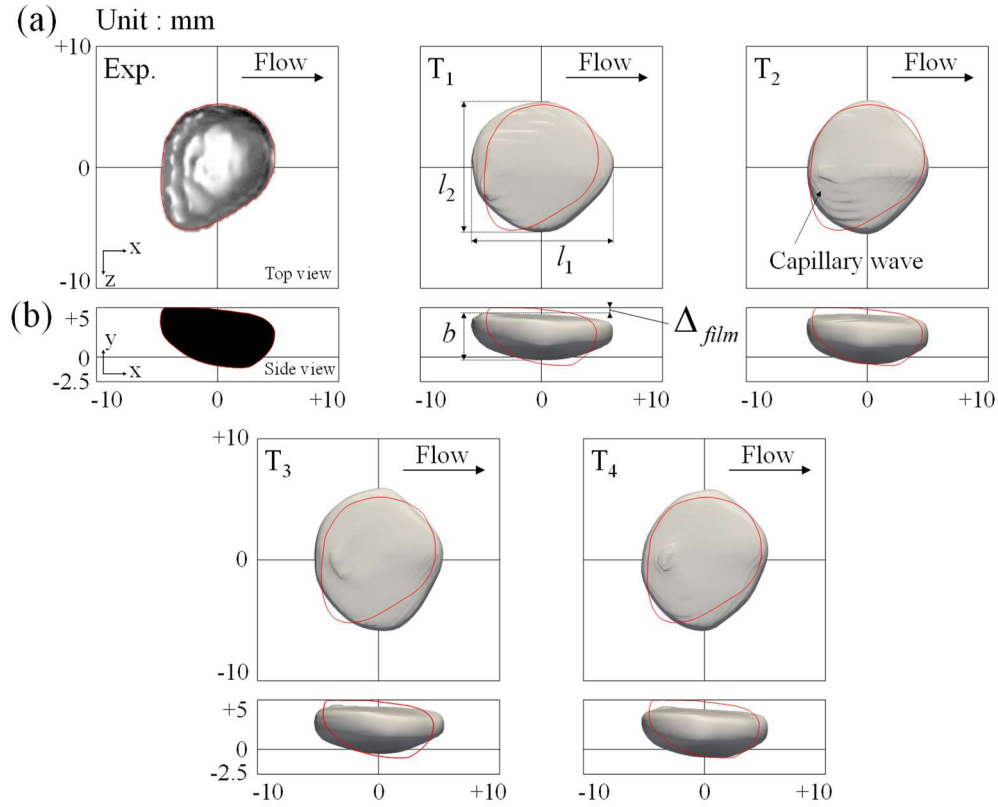
Figure 3.8: Evolution of the bubble shape compared to the experimental result. The red line represents outline of the experiment; (a) Top view, (b) Side view. Here, b is the height of the bubble, l_1 and l_2 are stream and spanwise length, and Δ_{film} is thickness of the liquid film, respectively.

Table 3.6 Shape factor of the present bubble.

	Oishi and Murai (2014)	Present CFD			
Time	-	T_1	T_2	T_3	T_4
l_1 [mm]	11.46	14.25	12.43	12.84	12.58
l_2 [mm]	12.67	13.09	13.64	14.26	14.05
b [mm]	5.74	4.72	4.16	4.86	5.10
l_1/l_2	0.88	1.09	0.91	0.90	0.89
Diff.	-	24 %	3 %	2 %	1 %
l_1/b	1.86	3.04	2.39	2.66	2.47
Diff.	-	63 %	28 %	43 %	33 %
l_2/b	2.11	2.79	2.64	2.97	2.78
Diff.	-	32 %	25 %	41 %	32 %
Δ_{film} [mm]	-	0.479	0.590	0.561	0.591

3.5.2 Instantaneous momentum flux

Figure 3.9 shows the profiles of the instantaneous momentum flux $u'v'$ along the iso-surface of a single bubble at the bubble centroid. The quantity $u'v'$ indicates not only the dependence of the liquid behavior around the bubble shape relative to that of single-phase flow, but also the local instantaneous source of the momentum flux. Each u' and v' component is obtained from equations (3.7) and (3.8).

$$u'(x, y, z) = u(x, y, z) - \overline{u_0}(x, y, z) \tag{3.7}$$

$$v'(x, y, z) = v(x, y, z) - \overline{v_0}(x, y, z) = v(x, y, z) \tag{3.8}$$

where, $u(x,y,z)$ and $v(x,y,z)$ are the instantaneous velocities in the stream and wall-normal directions, respectively. $\overline{u_0}(x,y,z)$ and $\overline{v_0}(x,y,z)$ are the mean velocities in the respective directions of the single-phase flow. Here, $\overline{v_0}(x,y,z)$ is considered to be zero in equation (3.8). The instantaneous momentum flux is obtained on the interface as a function of the angle from the top of the bubble. The angle is defined based on the centroid of the bubble and is positive in the counterclockwise direction. In general, the region of the profile can be divided into two categories based on the angle, this is, the upper surface ($\theta < 90°$, $\theta > 270°$) and the bottom surface ($90° < \theta < 270°$). The present data in the liquid film region show the momentum flux in the region, which is consistent with the experimental result.

However, the tendency of the instantaneous momentum flux $u'v'$ is different from the results seen in Fig. 3.9, as shown in Fig. 3.10, in which the region of the negative momentum flux appears over the side of the liquid film at all times. This implies that the local velocity in this region experiences backward acceleration. In contrast, the rear parts of the bubble show a spike in the graph of the momentum flux, as in the experiment. These regions correspond to the capillary wave and are close to the experimental value. Oishi and Murai (2014) explained this positive momentum flux by the induction of a high-speed sweep in the rear part for the migration of a large bubble.

In addition, these positive and negative momentum fluxes are considered to be the reason for the bouncing of the bubble with time. Meanwhile, the bottom surface ($135° < \theta < 225°$) was not affected by the momentum flux in the simulation but was affected by it in the experiment. This fluctuation is due to the interfacial curvature that determines the position of the separation point. The bubble of the present data has a flat bottom, while that of the experiment has a high

curvature and the front is tilted down in the *x*-axis, as shown in Fig. 3.8. Finally, we can observe an increasing momentum flux in the front part of the bottom surface ($235° < \theta < 270°$) during both the experiment and numerical simulation. However, an overestimation of the momentum flux can be observed. This is considered to be a numerical error due to the large size of the mesh in the streamwise direction.
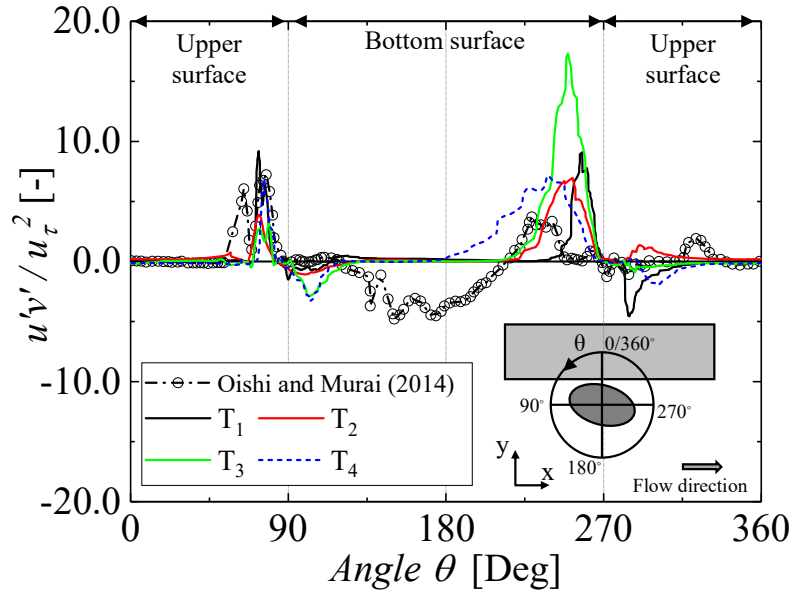

Figure 3.9: Instantaneous momentum flux on bubble surface by the angle, normalized by square of the friction velocity.
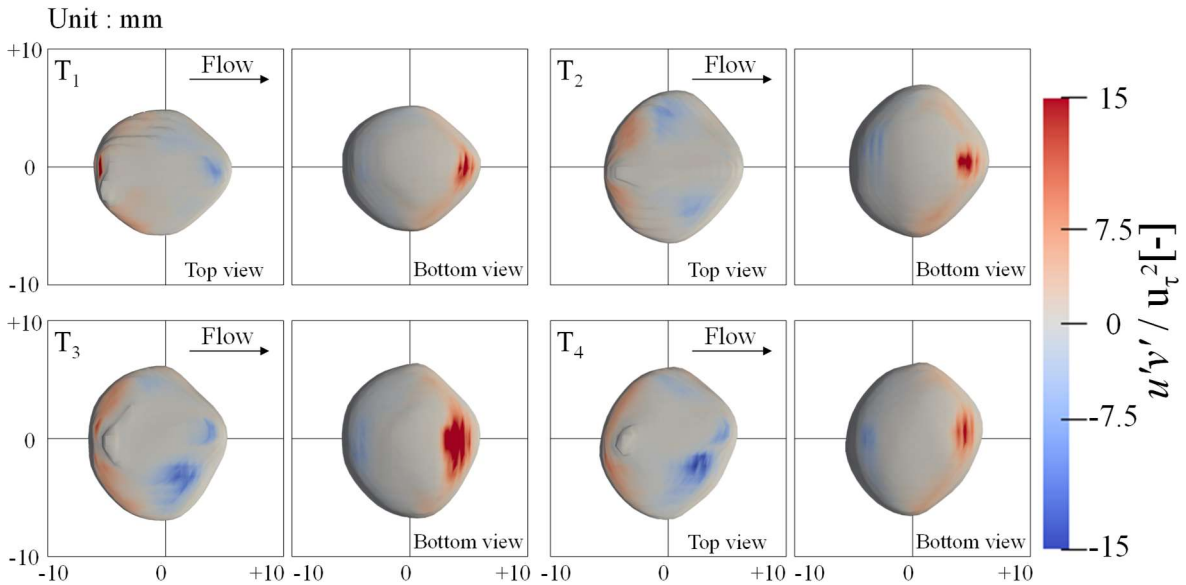

Figure 3.10: Contours of the instantaneous momentum flux on the iso-surface of the bubble in T_1-T_4.

3.5.3 Skin friction profile along the liquid film and secondary flow

Figure 3.11 shows the local skin friction ratio of the liquid films. The front side of the bubble is on the right side of the graph, which is based on a sample from time T_1–T_4. The sampling location corresponds to the centerline of the bubble in the spanwise direction. As described by Murai et al. (2007), the present results show that the skin friction ratio initially increases because the instantaneous momentum flux moves backward from the front part of the bubble. After increasing the skin friction ratio, this ratio starts to decrease in the middle of the liquid film, after which it rapidly decreases to reach the minimum value in the rear part. The rapid decreases in the rear parts occurred even when the capillary wave was neglected.

Thus, the positive momentum flux is considered to be the reason for the rapid decrease in the rear part because it is universally distributed in this region, as shown in Fig. 3.10. This also shows that there is similar thickness development between the wall and the top interface of the bubble. However, the value of the skin friction ratio varied. The skin friction ratios in T_1 and T_2 are greater than one in the whole region, while those in T_3 and T_4 become smaller than those in the rear part of the liquid film. This shows that the shape of the bubble approaches a quasi-steady one, and the flow condition around the bubble continues to develop until T_3. Therefore, it is concluded that the current method of numerical simulation using the *OpenFOAM* solver has sufficient capability and reproducibility to allow us to commence further studies on large-sized bubbles.
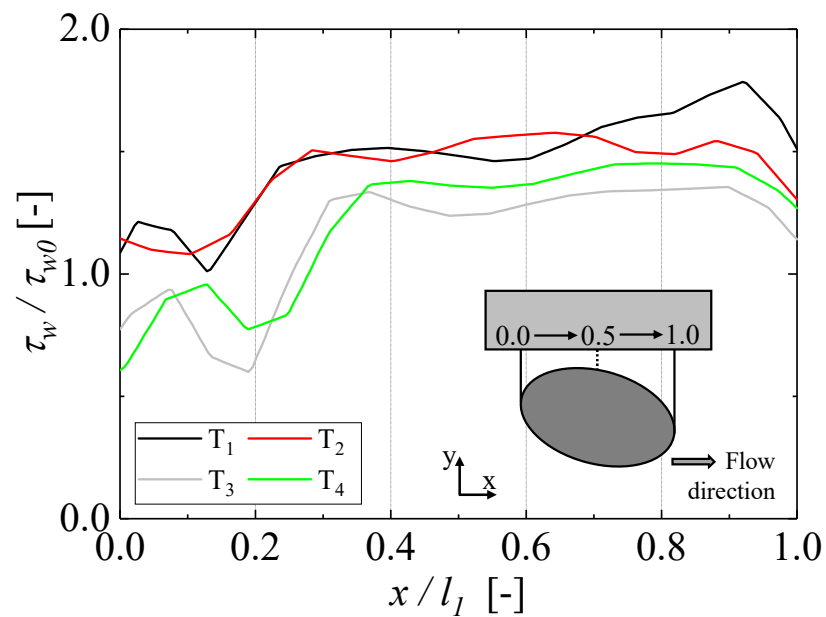

Figure 3.11: Profile of local skin friction normalized by that of single-phase flow.

To investigate the behavior of the secondary flow, Figure 3.12 presents the profiles and contours of the skin friction ratio at three locations. The profiles are extracted from the front side of the bubble to the calmed wake region where the skin friction ratio approached one, and the extracted length was 0.075 m. The skin friction of the secondary flow shows the fluctuations that increase more than that of the liquid film and forms a horseshoe shape. This is considered to be the reason for the greater increase in the average skin friction ratio in the present result compared to that in single-phase flow. Therefore, the vortical structure of the secondary flow is visualized to show its development after passing the bubble.
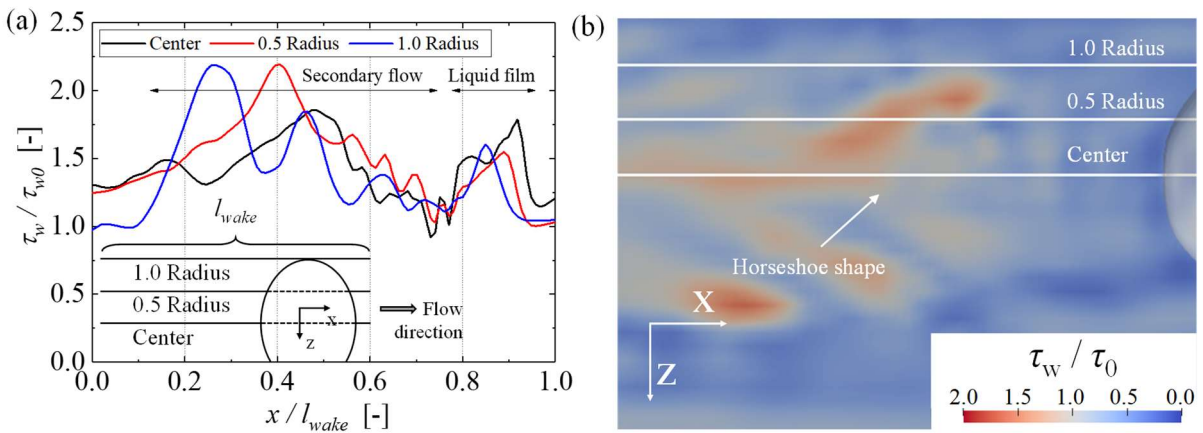
Figure 3.12: (a) The profile of the skin friction ratio in the secondary flow and the liquid film. (b) The contour of the skin friction ratio on the secondary flow. Three locations (1.0 and 0.5 Radius, Center) were selected for the skin friction ratio.

3.5.4 Vortical structure in the wake of a large-sized bubble

Figures 3.13 and 3.14 show the iso-surfaces of the streamwise vortices around the bubble in T_1–T_4. The vorticity values were ±330 s^{-1} as visualized from the side and bottom views. The counter-rotating vortices developed a bilateral symmetry. Simultaneously, the counter-rotating vortices developed on the same side; however, the sizes of the vortices were unequal. The generation of vortices is explained by the instantaneous velocity from the sectional view of the bubble. Figure 3.15 shows the velocity vector contours on the front view obtained from the centroid of the bubble. The vector originates from the relative velocity obtained from the v' component in equation (3.8) and the w' component, as follows:

$$w'(x,y,z) = w(x,y,z) - \overline{w_0}(x,y,z) = w(x,y,z) \tag{3.9}$$

where $w(x,y,z)$ and $\overline{w_0}(x,y,z)$ are the instantaneous and mean velocities in the spanwise directions, respectively. Here, $\overline{w_0}(x,y,z)$ is also considered to be zero.

Four vortices are clearly observed inside the bubble, as shown in Fig. 3.15(b). Based on the rotating direction, the pair of vortices at the same height that rotates in the counter-direction causes instantaneous velocity heads outside of the bubble, whereas the pair of vortices at the same width generated instantaneous velocity heads at the center of the bubble. Thus, the extension of large-sized bubbles in the spanwise direction is understood. In the case of the velocity contour at the liquid film, the velocity head in the spanwise direction for the outside is shown in Fig. 3.15(a). In addition, its magnitude increases as the location changes to the outside in the spanwise direction.
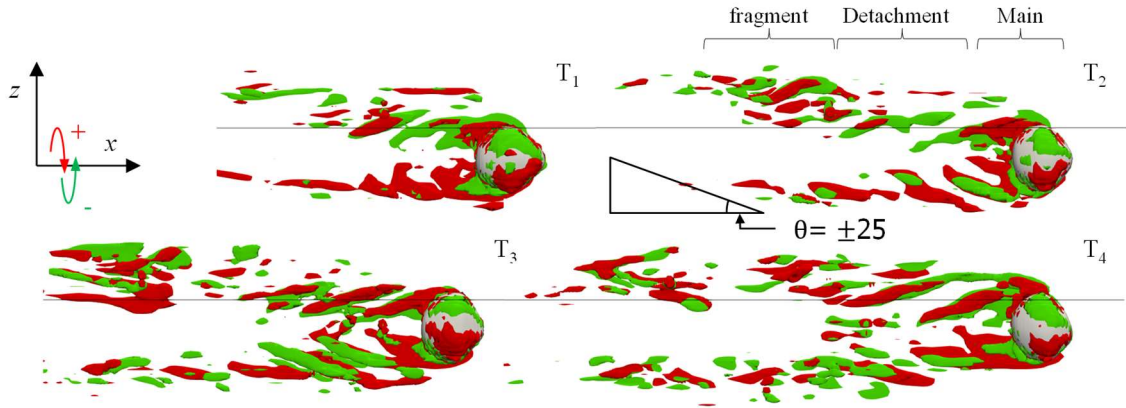
Figure 3.13: Top view of Snapshots on the iso-surface of the streamwise vortices. ($\omega_x = \pm 330$ s^{-1})
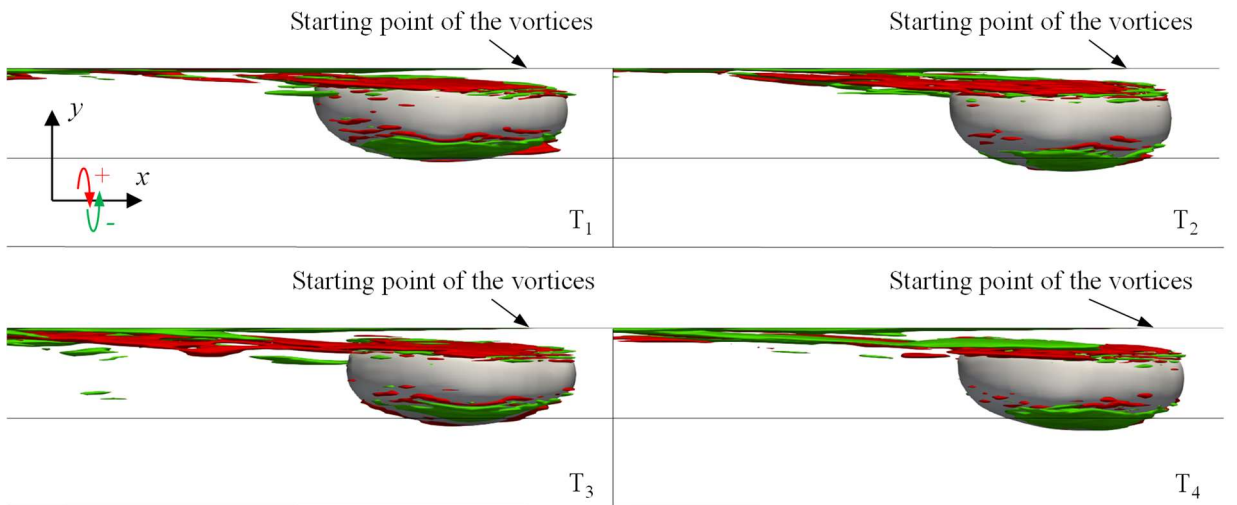
Figure 3.14: Side view of Snapshots of the iso-surface of the streamwise vortices. ($\omega_x = \pm 330$ s^{-1})

This generates vortices in a streamwise direction near the liquid film, which is in the opposite direction of the velocity vectors inside the bubble. Subsequently, the separated vortices move to the outer side of the bubble and fragment into small-scale vortices. When viewed from the side, these vortices originate either from the upper wall or the upper surfaces of the bubble. In addition, the smaller vortex of the unequal pair of vortices on the same side originates from the upper surfaces of the bubble.
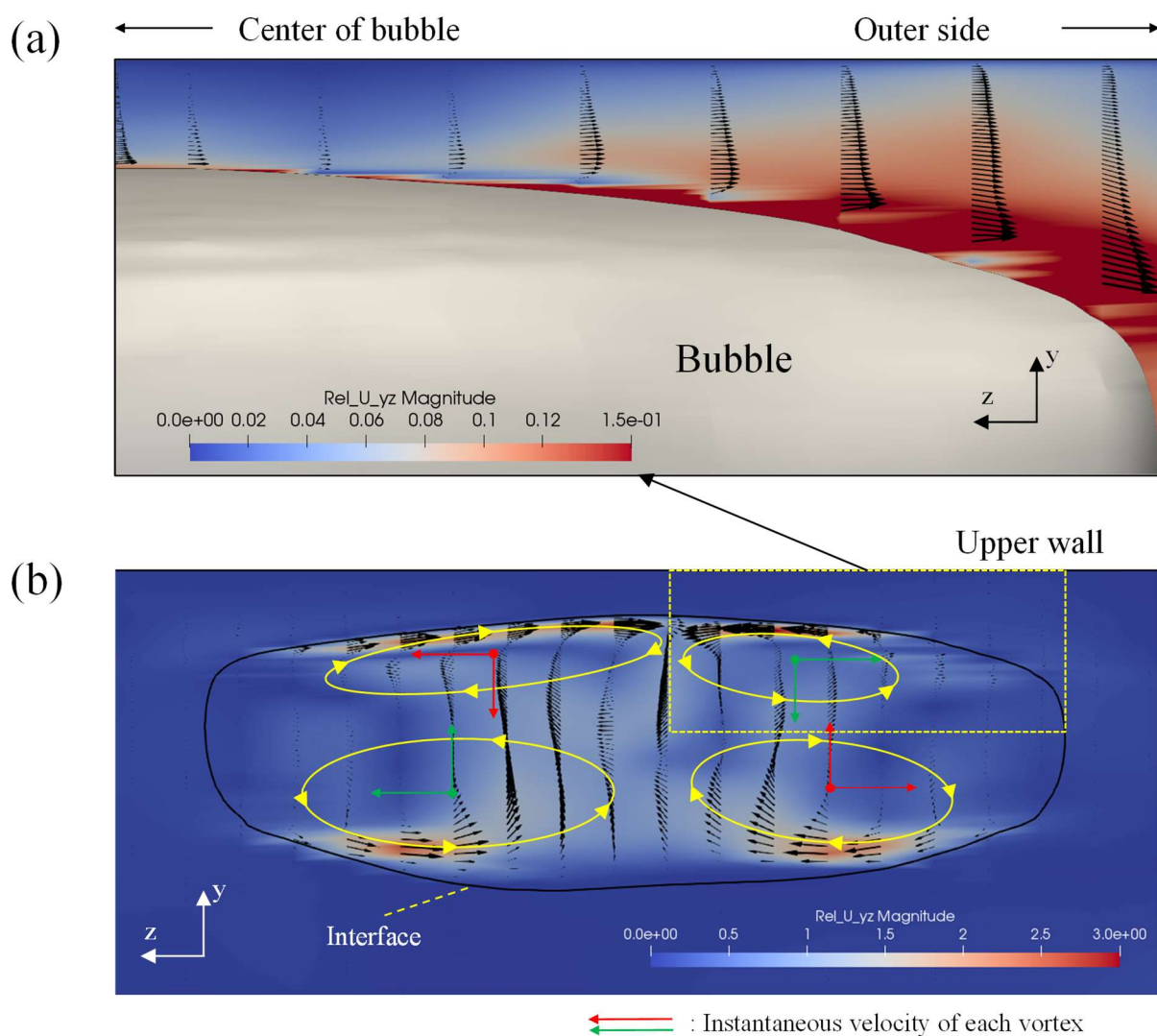
Figure 3.15: Velocity contours from the front view: (a) liquid film region, (b) internal region of the bubble.

Figure. 3.16 shows the schematic views of the vortical structures around the bubble based on the behavior of the vortices acquired from Figs. 3.13 and 3.14. There are four vortical structures between the bubble and the upper wall, and each neighboring structure rotates in a counter direction [see Fig. 3.16(a)]. The vortices that originate near the upper wall are wider and thinner than those originating from the upper surface of the bubble.

The vortices that originate from the upper surface of the bubble approach the upper wall as it moves away from the bubble [see Fig. 3.16(b)]. The location where these vortices are in contact with the upper wall changes depending on the bouncing period. These vortical structures are not generated continually but show three sequences. In the first sequence, the vortical structures are generated as crescent shapes and are still connected to the main structures [see Fig. 3.16(c-1)]. Moreover, this sequence corresponds to the region that does not have the horseshoe shape and the region behind the bubble in Fig. 3.12(b). In the next sequence [see Fig. 3.16(c-2)], the counter-rotating pillar vortices are separated and accompanied by each other in the wake region. These pillar vortices are tilted on the outer side along the x-axis, similar to the horseshoe shapes, and also show a similar shape on the contours of the skin friction ratio.

Figure 3.16: Schematic view of the vortical structures (a) Rear view. (b) Side view on right side of the bubble. (c) Bottom view as the sequences of the vortices.

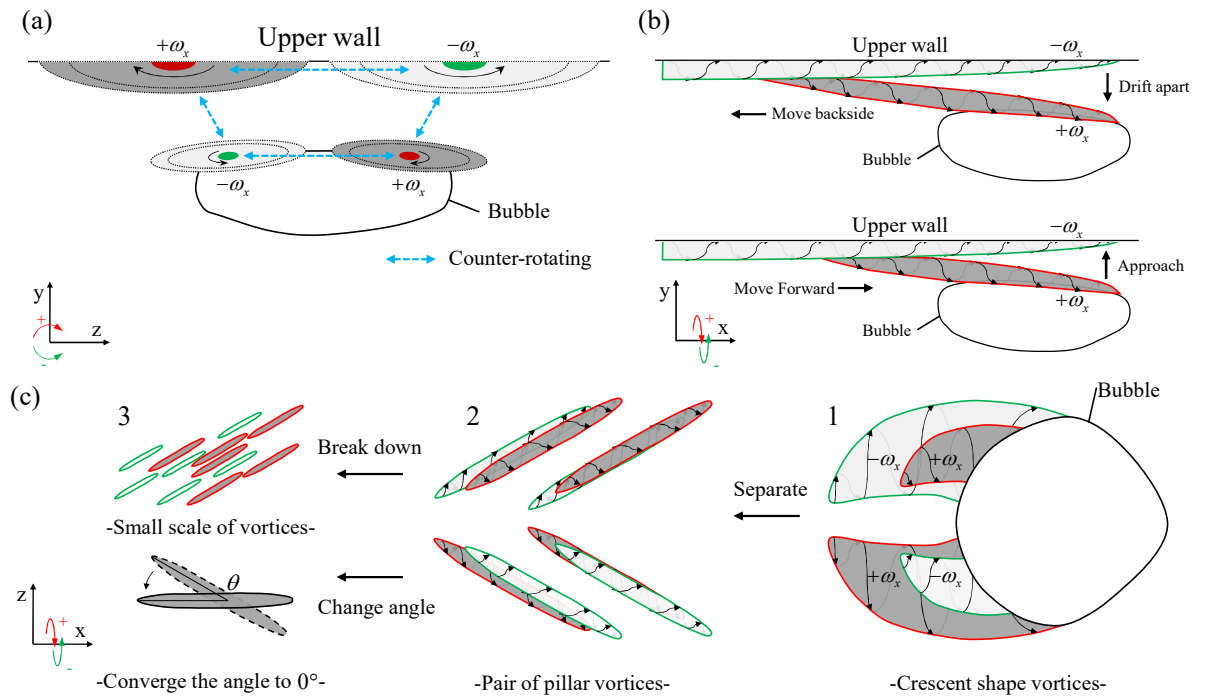In the third sequence [see Fig. 3.16(c-3)], the pillar vortices became the source of disturbance for the main flow with the same mechanism as in the case of single-phase flow. Thus, the pillar vortices are divided into vortices of small scale. If this does not occur, the angle of the vortices gradually decreases. This causes a continuous high skin friction ratio on the downstream.

The sequences that generate streamwise vortices correspond with the trend of the skin friction ratio in the secondary flow, which is expected. Thus, it is considered that the understanding of each sequence to generate the vortices can elucidate the trend of the skin friction ratio in the secondary flow. To understand the behavior of the vortical structures, their instantaneous velocities originating from the vortical structure were reviewed based on the study by Leweke et al. (2016).

The instantaneous velocities of the vortical structures can be evaluated based on the direction of rotation and the strength of the vortices. Figure 3.17 shows the vorticity profiles in the vertical direction at the two locations (P_1 and P_2). Here, $y/h = 2.0$ and 0.0 represent the upper and bottom walls, respectively. As a result, the vorticity near the upper wall ($y/h = 2.0$) is twice as large as that originating from the upper surface of the bubble ($y/h = 1.8$). This difference in vorticity strength is responsible for the angular velocity of both vortical structures. In other words, the vorticity center of the pair is located on the upper wall, and the angular velocity of each pair of the vortical structures reaches to the outer side of the wake region. Based on this description, the behavior of the vortical structures during the first and second sequences can be explained schematically as shown in Fig. 3.18.
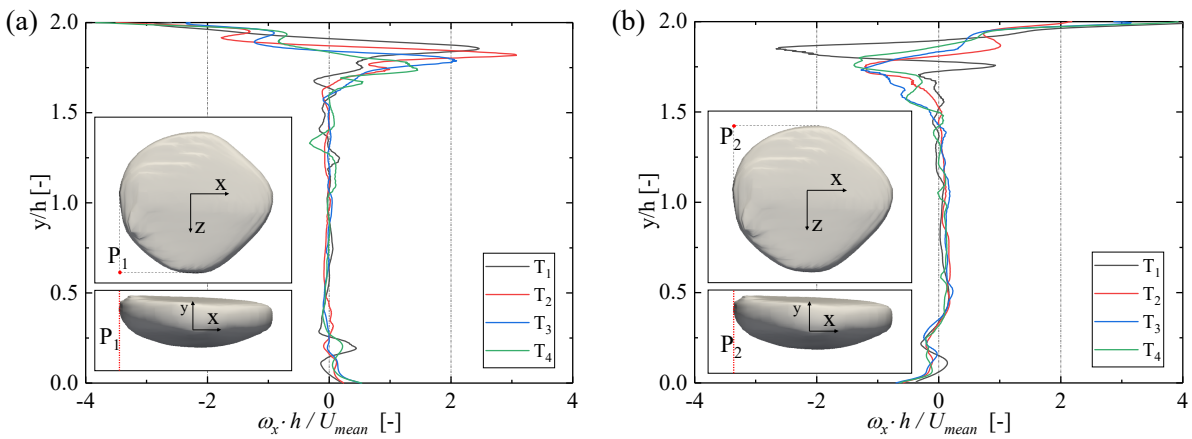

Figure 3.17: The normalized vorticity profile by the half height of the channel (a) P_1 (b) P_2. Both the locations are presented on left side of the picture (The bottom view of the bubble).

First, the vortical structures from the upper surface of the bubble approached the upper wall because of the instantaneous velocity due to the pair of vortices [see Fig. 3.18(a)]. This behavior results in no interaction between the vortices on the upper wall and those on the upper surface of the bubble because of the long distance between them.

Thus, the vortical structures develop into a crescent shape without separation in the first sequence, as shown in Fig. 3.16(c-1). Thereafter, the vortical structures on the upper surface of the bubble converge towards the vortical structures originating from the upper wall. The angular velocity induced by the difference in the strength of the vortices moves the vortical structures of the upper surface of the bubble to the outer side, separated from the main structures [see Fig. 3.18(b)]. In addition, it is expected that this process may be accelerated due to the bouncing of the bubble, as observed in Fig. 3.7(c).

Finally, the angles of the vortices in the two sequences in Fig. 3.16(c-2) were reviewed by Park et al. (2014) to understand the high skin friction ratio in this region. The angles of the streamwise vortices near the wall of the single-phase flow are mainly distributed near 0°, and the angles of these structures increase with increasing y^+.

Based on this notation, the characteristics of the vortical structures originating from the upper surface of the bubble are consistent with those observed in the previous study of Park et al. (2014). However, the present data also show that the angles of the vortices near the wall, which are expected to be near 0° from the *x*-axis, are approximately ±25°, as shown in Fig. 3.14. This implies that the current size of the bubble turns the flow condition below the buffer layer into a turbulent flow with increasing skin friction ratio in this region.
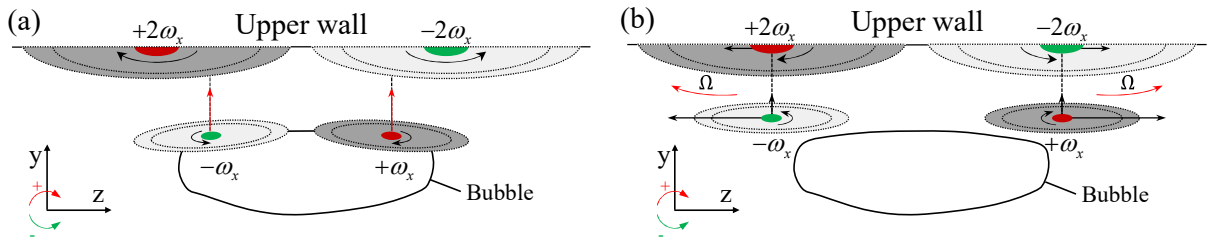
Figure 3.18: Schematic representation on the instantaneous velocity of the vortical structures from the rear viewpoint (a) The instantaneous velocity of the vortical structure that originated from the upper surface of the bubble (b) The instantaneous and the angular velocity of the vortical structure of the upper surface of the bubble when approaching to the upper wall.

3.6 Conclusion

In this study, we investigated the behavior and properties of a large-sized bubble in a turbulent wall flow in a horizontal channel. The following conclusions were drawn.

(a) The numerical procedure was established by dividing the numerical simulation into three stages. Based on the current solver (*interIsoFoam*, which implements *IsoAdvector*), the numerical results show trends similar to those observed in the experiment.

(b) In the current bubble, high skin friction is generated at the secondary flow, which corresponds to the distribution of the streamwise vortices in the secondary flow. Thus, the secondary flow was divided into three sequences, describing the shapes of the vortices. In addition, the behavior of the secondary flow can be described by the interaction between the pair of vortices generated on the upper wall and on the upper surface of the bubble.

(c) The large-sized bubble in this study had a large skin friction. This allowed identification of the reason for the increase in drag, but it was not possible to determine the consistency of this phenomenon without changing the size of the bubbles. Later, the sizes of the bubbles are varied to investigate their drag reduction effects and perform direct numerical simulations by refining the mesh conditions.

References

[1] Kim, S.W., Oshima, N., Murai, Y., and Park, H.J., 2020. Numerical investigation of a single intermediate-sized bubble in horizontal turbulent channel flow. *J. Fluid Sci. Technol.* 15(3).

[2] American Bureau of Shipping, 2019. Air Lubrication Technology, pp.1-15.

[3] McCormick, M., and Bhattacharyya, R., 1973. Drag reduction of a submersible hull by electrolysis. Nav. Eng. J. 85(2), pp. 11–16.

[4] Fukuda, K., Tokunaga, J., Nobunaga, T., Nakatani. T., Iwasaki, T., and Kunitake, Y., 1999. Frictional Drag Reduction with Air Lubricant over Super Water Repellent Surface (2nd Report) -Resistance Tests of Tanker and High Length to beam ratio Ship Models-, *J. Soc. N.A. Japan* 186.

[5] Fukuda, K., Tokunaga, J., Nobunaga, T., Nakatani, T., and Iwasaki, T., 2000. Frictional drag reduction with air lubricant over a super-water-repellent surface, *J. Mar. Sci. Technol.* 5, pp. 123-130.

[6] Moriguchi, Y., and Kato, H., 2002. Influence of microbubble diameter and distribution on frictional resistance reduction, *J. Mar. Sci. Technol.* 7, pp.79-85.

[7] Kitagawa, A., Hishida, K., and Kodama, Y., 2005. Flow structure of microbubble-laden turbulent channel flow measured by PIV combined with the shadow image technique, *Exp. Fluids* 38, pp. 466–475.

[8] Murai, Y., Fujii, H., Tasaka, Y., and Takeda, Y., 2006. Turbulent bubbly channel flow investigated by ultrasound velocity profiler. *J. Fluid Sci. Technol.* 1(1), pp. 12–23.

[9] Murai, Y., Fukuda, H., Oishi, Y., Kodama, Y., and Yamamoto, F., 2007. Skin friction reduction by large air bubbles in a horizontal channel flow, *Int. J. Multiphase Flow* 33(2), pp.147-163.

[10] Oishi, Y., and Murai, Y., 2014. Horizontal turbulent channel flow interacted by a single large bubble, *Exp. Therm. Fluid Sci.* 55, pp.128-139.

[11] Lu, J., Fernandez, A., and Tryggvason, G., 2005. The effect of bubbles on the wall drag in a turbulent channel flow. *Phys. Fluids* 17(9), 095102.

[12] Sugiyama, K., Kawamura, T., Takagi, S., and Matsumoto, Y., 2005. Recent Progress of Microbubble Flow Simulation for Elucidating Drag Reduction Mechanism. *Proc. of the 6th Symp. on Smart Control of Turbulence*, pp. 191-202.

[13] Kawamura, T., 2005. Numerical and experimental investigation the mechanism of the microbubble drag reduction, *Proc. 6th Symposium Smart Control of Turbulence.*

[14] Spandan, V., Verzicco, R., and Lohse, D., 2017. Deformable ellipsoidal bubbles in Taylor-Couette flow with enhanced Euler-Lagrangian tracking. *Phys. Rev. Fluids* 2(10), 104304.

[15] Park, H.J., Tasaka, Y., Oishi, Y., and Murai, Y., 2015. Drag reduction promoted by repetitive bubble injection in turbulent channel flows. *Int. J. Multiphase Flow* 75, pp. 12-25.

[16] Leweke, T., Dizès, S.L., and Williamson. C.H.K., 2016. Dynamics and Instabilities of Vortex Pairs, *Annu. Rev. Fluid Mech.* 48, pp. 507-541.

[17] Park, H.J., Tasaka, Y., Murai, Y., and Oishi, Y., 2014. Vortical structures swept by a bubble swarm in turbulent boundary layers, *Chem. Eng. Sci.* 116, pp. 486-496.

Drag modulation of a single large-sized bubble injection in turbulent channel flow

Contents

Preface

The aim is to investigate Weber number dependency of large-sized bubbles based on and improved the numerical model in **Chapter 2**. The detailed drag modulation using DNS shows evidence of improvement of drag reduction by large-sized bubbles. This work was presented at Kim et al. (2020).

Abstract

In this study, we analyzed the drag modulation effects of large-sized bubbles, especially high-Weber number bubbles, on the horizontal turbulent channel flow using direct numerical simulation. The Weber number (*We*) was varied from 130 to 337 based on the equivalent diameter and bubble velocity. To study the drag modulation mechanism of large-sized bubble, the skin friction profile along the centerline of the bubble and local mean ratio of skin friction were analyzed at different Weber numbers. The bubble length was found to have a significant effect on drag reduction toward the rear region of the bubble. Based on this observation, we analyzed the influence of the bubble regions on drag modulation by confining each region. The numerical results indicated that the skin friction was sensitive to the bubble size and bubble regions, the changes in the skin friction profile, contour, and local averaged values with the variation in the Weber number were analyzed. Considering the relationship between the bubble regions and skin friction, most bubbles exhibited an increase in drag on the liquid film until *We* = 337. Furthermore, the area of drag reduction in the secondary flow increased with an increasing Weber number. These results afford new insights into bubble-induced drag modulation in different regions of horizontal flow.

4.1 Introduction

Direct numerical simulation (DNS) has been used to obtain significant insights into bubbly flows, which occur in a wide variety of industrial processes. For channel flows, the DNS study of bubbly flows can be divided into the vertical and horizontal types.

In the case of vertical channels, the buoyancy of the bubbles acts along the streamwise direction, resulting in a clear difference in the distribution of the void fraction and flow pattern according to the flow direction. This phenomenon is important for applications related to heat exchangers, such as nuclear reactors and power plants (Hibiki and Ishii, 2002). Numerous representative DNS studies on bubbly flows in vertical channels have been reported by Lu and Trygvasson. The turbulent bubbly downflows in the vertical channel as the number of the spherical bubble were examined, and they confirmed that the bubbles concentrated on the core region, similar flow characteristics on wall region with single-phase flow, and dependence of turbulent properties as bubble size (Lu and Trygvasson, 2006, 2007).

From further studies, J. Lu and G. Trygvasson (2008, 2013) confirmed that the spherical bubble was close to the wall while deformable bubbles were distributed on the core region on the channel for upflow. The velocity fluctuation and vorticity are also enhanced from deformable bubbles while suppressed from the spherical bubbles. In their most recent studies, they examined the effects of surface tension and void fraction on the structure of multiphase flow in a vertical channel (Lu and Trygvasson, 2018, 2019).

In the case of horizontal channels, buoyancy acts in the wall-normal direction of the channel. Consequently, air bubbles are present on the upper wall regardless of the bubble size or void fraction. These bubbles cause unbalanced flow characteristics in the channel center that hinders heat exchanges or mass transfer between the liquid-phase and the wall. Meanwhile, bubbly flow in the horizontal channel modifies the turbulent boundary layer, thereby reducing the frictional drag on the upper wall. This characteristic is called bubble drag reduction (BDR) and is applied to liquid transport in pipelines and ship surfaces in water. Since McCormick and Bhattacharyya (1973) achieved BDR using microbubbles, and the first DNS study on the BDR of microbubbles was conducted by Kanai and Miyata (2001). Subsequently, other researchers (Xu et al., 2002; Ferrante and Elghobashi, 2004; Pang et al., 2014; Zhang et al., 2020; etc.) have conducted DNS studies to investigate the mechanism of BDR on microbubbles in horizontal channel.

In the last two decades, detailed investigations have been conducted to understand BDR in turbulent flows. Moriguchi and Kato (2002) and Kawamura et al. (2003) reported that there was

no change in drag reduction over a range of injected bubble sizes that were significantly larger than the viscous length, and Shen et al. (2006) revealed that the BDR effect is mostly independent of bubble size. Lu et al. (2005), Sugiyama et al. (2005), Kawamura (2005), and Spandan et al. (2017) confirmed the positive role of deformable bubbles in the BDR process through numerical simulation. The deformability of bubbles leads to a different BDR mechanism. For shear-induced deformation (i.e., the capillary number regime), the local shear stress field around the bubble is modified. For buoyancy-induced deformation (i.e., the Froude number regime), the bubble wake alters the ambient stress field.

Both effects interact to replace the local turbulent characteristics around the bubble (i.e., the Weber number regime). Additional details of the flow physics were reported by Murai (2014). This knowledge has motivated BDR studies in the horizontal channel to be extended to the case of large deformable bubbles. Although these large-sized bubbles are easily generated in experiments, their simulation by computational fluid dynamics (CFD) analysis is difficult because of the sensitive deformability of gas-liquid interfaces subject to both turbulent shear and buoyancy. This is the challenge and motivation for the present study.

From experimental investigations, Murai et al. (2006) reported that large-sized bubbles provided a velocity gradient that calmed the wake region. The performance of large-sized bubbles with respect to BDR was later found to be dependent on the bubble length by Murai et al. (2007) and Oishi and Murai (2014). In addition to the velocity gradient in the wake region, it is supposed that the liquid film between these bubbles and the wall also reduces skin friction by relaminarizing flow in the film. From this point of view, recently a relationship between the film thickness and BDR was experimentally investigated by Park et al. (2019). However, some large-sized bubbles often increase the drag, resulting in larger skin friction than that under single-phase flow.

We considered that the increase in drag associated with large-sized bubble was based on the findings of Murai et al. (2007) who reported that large-sized bubbles show the common spatial relationship between drag modulation (drag increment and reduction) and the bubble location. In the present study, DNS of a turbulent horizontal channel flow with a single large-sized bubble of varying size was performed to investigate the spatial relationship between skin friction and different flow regions. These DNS results afford a new understanding of bubble-induced drag modulation, which will be explained in detail in this paper.

4.2 Numerical setup and conditions

The numerical simulations were performed using OpenFOAM® v1906; Table 4.1 shows the solvers and methods used in this study. *PimpleFoam* was used to develop the turbulent channel flow, whereas *interFoam* and *InterIsoFoam* were used for two-phase flow. Both of the two-phase flow solvers are based on the VOF method, but they implement different interface sharpening methods. Both solvers use the *Pimple* algorithm for pressure-velocity coupling in a segregated manner, which computes a velocity field to satisfy equations (2.1) and (2.2) using an iterative procedure. The continuum surface force (CSF) method proposed by Brackbill et al. (1992) was implemented for the surface tension force in both two-phase solvers.

The discretization schemes and models used in this study are presented in Table 4.2; all the schemes provide second-order accuracy. The *backward* scheme—an accurate second-order backward-differencing scheme—was used for time discretization in the momentum equations. The global time step was set to 5.0×10^{-6} s to ensure that the Courant–Friedrichs–Lewy (CFL) number remained below 0.8; the interface CFL number less than below 0.4 in each simulation case. The divergence schemes employed were composed of two total variation diminishing (TVD) schemes, which is utilized the combined upwind and central differencing schemes, were used for the convective terms in equations. (2.1) and (2.2). The first TVD scheme, *limitedLinear*V, was used for the momentum flux. The second TVD scheme, *vanLeer*V, was used for the mass flux.

Table 4.1 Summary of the numerical simulation setup.

Term	Description
Solver names	*pimpleFoam* (single-phase flow), *interIsoFoam* *interFoam* (compared with *interIsoFoam*)
Time dependence	Transient
Two-phase flows	VOF (interface capturing method)
Pressure–velocity coupling	*Pimple* algorithm (coupled PISO[*] and SIMPLE[**])
Surface tension model	CSF method
Sharp interface model	*IsoAdvector* (*interIsoFoam*), *MULES* (*interFoam*)

[*]PISO: pressure-implicit with splitting of operators; [**]SIMPLE: semi-implicit method for pressure-linked equations.

The 'V' in both scheme names indicates that these are specialized versions designed for vector fields. A Gaussian *linear* scheme was used for gradient and Laplacian terms. Additional details regarding the various numerical schemes in OpenFOAM are provided in the OpenFOAM user guide.

Table 4.3 lists the experimental and numerical conditions of present work and previous studies (Oishi and Murai, 2014, Kim et al., 2020). The Reynolds and Froude numbers were obtained from the single-phase flow condition, and the mean velocity of the fluid in the channel (U_{mean}) was slightly modified to maintain the same friction velocity (u_τ). Figure 4.1 shows the geometrical configuration of the computational domain used in this study. The dimensions of the domain are as follows: height ($H = 2h$) = 10 mm, where h is the half-height of the channel; length (L) = 100 mm; and width (W) = 70 mm. Note that the length and width of the computational domain can be shortened than that of Oishi and Murai (2014) by the periodic condition in the streamwise and spanwise direction, and it used in this study were selected to be smaller than those used by Kim et al. (2020) to save computational resource.

Table 4.4 lists the boundary conditions of the computational domain. The numerical procedure was divided into three stages owing to the required changes in the solvers and boundary conditions: Stage 1 conducted fully developed turbulent channel flow, Stage 2 conducted bubble injection and stabilization, and Stage 3 conducted turbulent channel flow with a single injected large-sized bubble. Further details regarding this numerical procedure have been reported by Kim et al. (2020).

Table 4.2 Summary of discretization schemes.

Term	Scheme, Type / Model	Description
Time discretization scheme	*Backward*	Second-order, implicit, potentially unbounded
Divergence schemes	Gauss *limitedLinear*V 1, *vanLeer*V 1	Second-order, bounded 'V'-scheme
Gradient schemes	Gauss *linear*	Second-order, unbounded
Laplacian schemes	Gauss *linear corrected*	Second-order, unbounded

Table 4.3 Comparison of experimental and numerical conditions.

Channel property	Oishi and Murai (2014)	Kim et al. (2020)	Present study
$L \times H \times W$ [mm]	$6000 \times 10 \times 100$	$200 \times 10 \times 75$	$100 \times 10 \times 70$
ρ [kg/m^3]	998.7	998.7	998.7
v [m^2/s]	1.08×10^{-6}	1.08×10^{-6}	1.08×10^{-6}
U_{mean} [m/s]	1.0	1.06	1.039
Fr	3.19	3.37	3.31
Re	9260	9783	9620
Re_τ	260	260	260
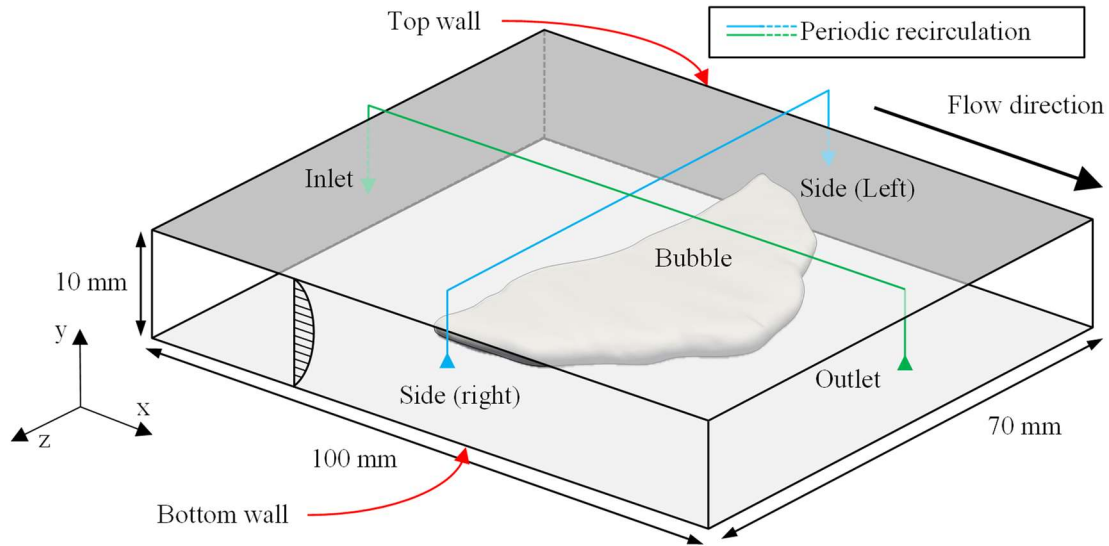
Figure 4.1: Computational domain and boundary conditions.

Table 4.4 Boundary conditions and solvers used in each stage.

Term	Stage 1	Stage 2	Stage 3
Solver	*pimpleFoam*	*interIsoFoam, interFoam*	
Bottom/Top	*NoSlip*	*NoSlip, ConstantAlphaContactAngle* (71°)	
Inlet/Outlet		*Cyclic* (Inlet ↔ Outlet)	
Side		*Cyclic* (Left ↔ Right)	
Velocity		Pressure gradient (streamwise direction)	

4.3 Mesh dependency of turbulent properties

4.3.1 Establishment of test cases

The convergence of the channel flow results was investigated with respect to the grid by examining the profile of the dimensionless mean velocity in the streamwise direction $u^+ = u/u_\tau$ and the root-mean square (RMS) velocity fluctuations in the streamwise and wall-normal directions, as shown in equation (4.1). In addition, the dimensionless Reynolds shear stress, $-\overline{u'v'}/u_\tau^2$, which was represented as a function of wall distance $y^+ = yu_\tau/v$ and y/h, was examined.

$$u_{rms}^+ = \sqrt{\overline{u'^2}} \, / u_\tau \; ; \quad v_{rms}^+ = \sqrt{\overline{v'^2}} \, / u_\tau \qquad (4.1)$$

Table 4.5 lists the main parameters in each simulation case based on the total number of grids, n_{total}. This number was obtained from the effective grid refinement ratio, τ_e, introduced by Roache (1998), which is defined as $\tau_e = (N_1/N_2)^{(1/D)}$, where N_1 and N_2 are the n_{total} of the finer and coarser grids, respectively, and D is the dimension of the computational domain. Here, the grid refinement ratio, r, was set to greater than 1.1 to allow the discretization error to be differentiated from other error sources, such as the iterative convergence or computer round-off. The function of the dimensionless distance of the grid as Δx^+, Δy^+, and Δz^+ was presented, as defined in equation (4.2).

$$\Delta x^+ = u_\tau \Delta x \, / v \; ; \quad \Delta y^+ = u_\tau \Delta y \, / v \; ; \quad \Delta z^+ = u_\tau \Delta z \, / v \qquad (4.2)$$

Table 4.5 DNS of channel flows at varying grid resolutions, showing the dimensionless distance of the grid, Δy_w^+ and Δy_c^+, in the wall-normal direction at the wall and center of the channel, respectively.

Case	1.46M	3.99M	10.93M	29.97M
n_{total}	1,461,600	3,994,848	10,937,088	29,970,336
τ_e		1.398		
Δx^+	36.11	24.99	18.05	12.87
Δy_w^+	1.40	1.07	0.76	0.54
Δy_c^+	33.27	25.39	17.95	12.84
Δz^+	17.91	12.49	8.99	6.47
r		0.0424		
$n_x \times n_y \times n_z$	144 × 25 × 203	208 × 33 × 291	288 × 47 × 404	404 × 66 × 562

4.3.2 Numerical results of fully developed turbulent channel flow

Figure 4.2 shows the numerical results for various grid resolutions. Below $y^+ = 15$, the mean velocity and RMS velocity fluctuation gradually tended to approach the experimental results with increasing n_{total}. The 29.97M case almost perfectly matched the experimental results, except for the RMS velocity fluctuation in the wall-normal direction, Over and underestimation of the RMS still occurred above $y^+ = 15$.

However, the Reynolds shear stress—an important parameter for investigating drag modulation—followed the experimental results reasonably well. In addition, the flow characteristics below $y^+ = 15$, where drag modulations occur, also resolved well. Consequently, present study was performed using 29.97M case.
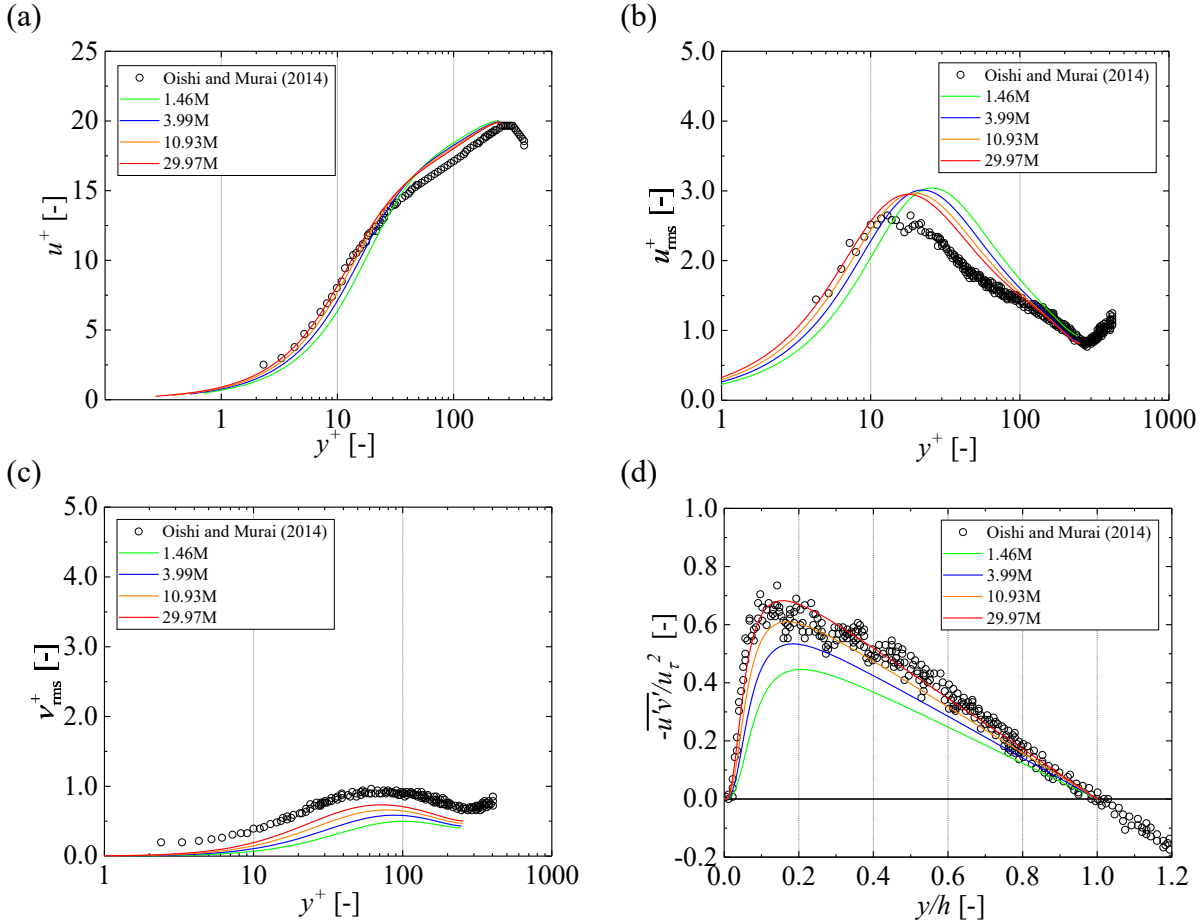

Figure 4.2: Comparison of turbulent properties for various grid resolutions: (a) Mean velocity, (b) RMS velocity fluctuation in streamwise direction, (c) RMS velocity fluctuation in wall-normal direction, and (d) Reynolds shear stress.

4.4 Validation work of interface tracking method

4.4.1 Initial condition of validation cases

The smearing of α into the channel must be prevented because this changes the fluid properties, affecting the skin friction on the upper wall and hindering the conservation of the bubble volume. In this study, smearing was prevented using the interface sharpening method. Indeed, two different interface sharpening methods (*MULES* and *IsoAdvector*) were evaluated to determine which prevents interface smearing to the channel side in the turbulent flow condition better.

To evaluate the degree of interface sharpening provided by each method, the outer interface region in the range of $0.5 < \alpha < 1$, defined in Fig. 4.3(a), was evaluated by dividing it into several layers, as described in Table 4.6. The volume of each of these layers (V_l) was confirmed during the calculations. The initial condition of the verification work is shown in Fig. 4.3(b). The fully developed turbulent channel flow was generated as described in Section 2.4 (Stage 1), and the stabilization calculations were performed (Stage 2). Here, Weber number of the bubble was 87.
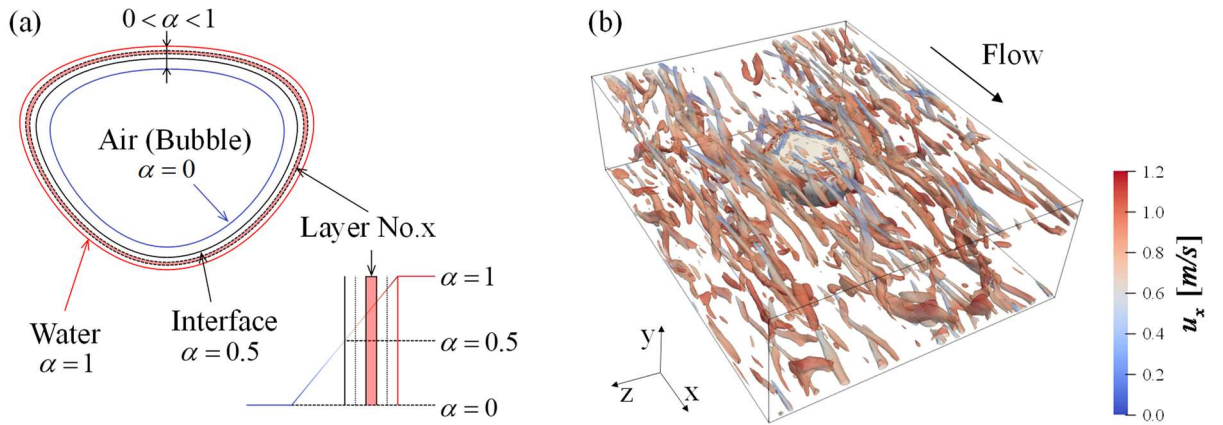

Figure. 4.3: (a) Definition of an interface layer; (b) Initial conditions of the verification work; the coherent turbulent structure is visualized by the iso-surface of Q-criterion (Q = 30000).

Table 4.6 Parameters of interface layers, where the volume of each layer is V_l, and the volume of layer No. 1 is V_{l0}. The volume ratio of each layer was obtained from the initial condition.

Layer	No.1	No.2	No.3	No.4	No.5	No.6
Range of α_{air} $(= 1 - \alpha)$	$0.5 - 0.1$	$0.1 - 0.1^2$	$0.1^2 - 0.1^3$	$0.1^3 - 0.1^4$	$0.1^4 - 0.1^5$	$0.1^5 - 0.1^6$
V_l/V_{l0} [-]	1	0.49	0.21	0.10	0.06	0.03

4.4.2 Validation results : 3D bubble test in turbulent channel flow

Figure 4.4 shows the volume ratio of each layer with each solver, where t is the instantaneous calculation time, and T represents the total calculation time. Using the *MULES* method, the volume ratio of each layer increased significantly from the beginning of the calculation, resulting in a rapid increase in the volume ratio of each layer and a constant tendency to increase in the total calculation. In contrast, using the *IsoAdvector* method, the volume ratio of each layer fluctuated slightly but remained relatively uniform.

Figure 4.5 shows the iso-surface of the interface at $t/T = 0.55$. Using the *MULES* method, iso-surface of $\alpha_{air} = 0.1^6$ was observed from the wake region, whereas under the *IsoAdvector* method, except for small regions, it exhibited similar tendencies. The results shown in Figs. 4.4 and 4.5 indicate that the interface region provided by the *MULES* method gradually smeared from the bubble to the outside, whereas that provided by the *IsoAdvector* method was not in the turbulent flow condition.

This is important information because Stage 3 will be performed at a higher Weber number for the bubble over a longer calculation time which is expected to lead to more smearing situation than in this verification. Consequently, the main simulations were performed using the *IsoAdvector* method to inhibit numerical diffusion effectively.
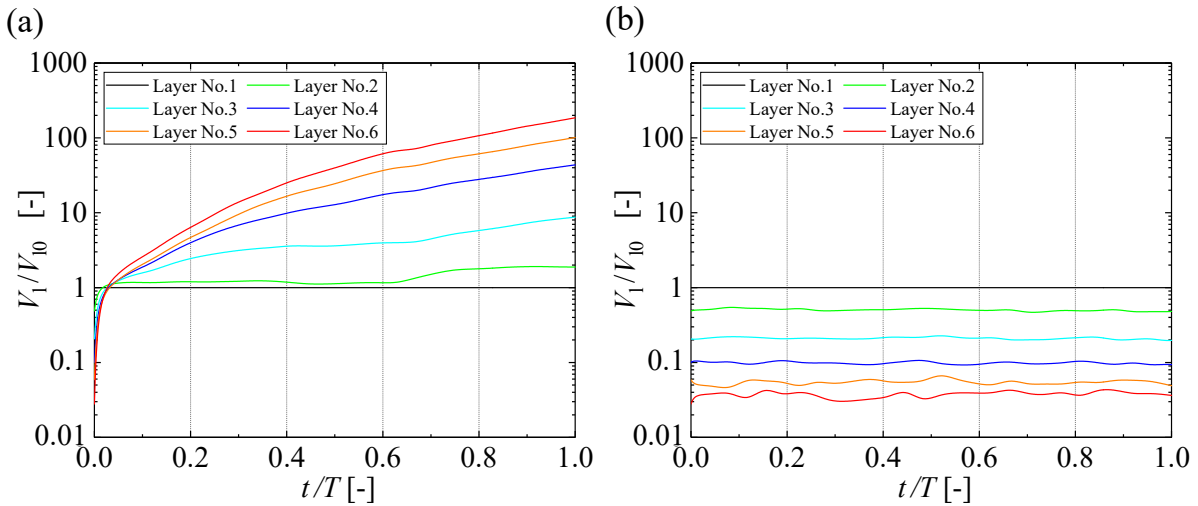

Figure 4.4: Comparison of volume ratio of layers with different interface sharpening methods: (a) *MULES* and (b) *IsoAdvector* methods.
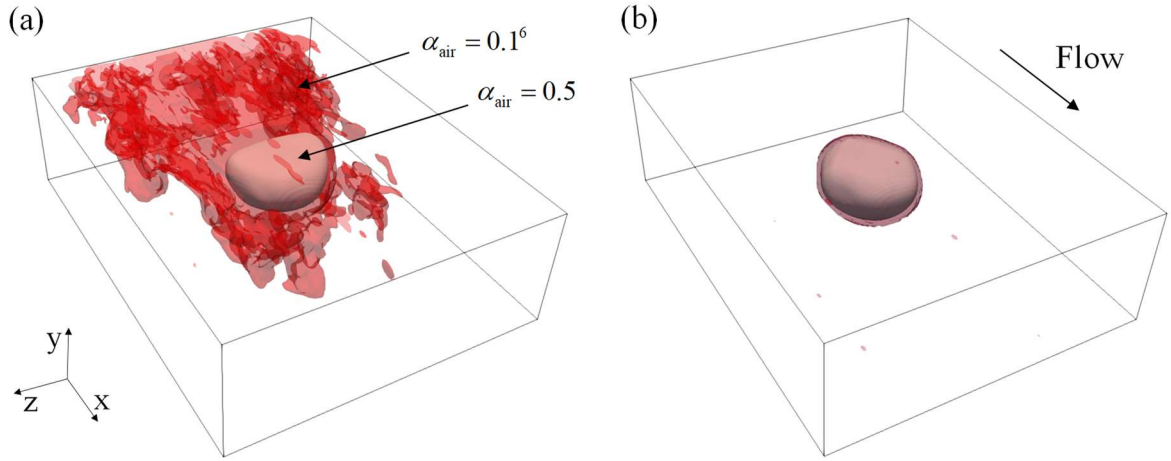
Figure 4.5: Comparison of iso-surface at t/T = 0.55 with different interface sharpening methods: (a) *MULES* and (b) *IsoAdvector* methods; the gray iso-surface indicates that $\alpha_{air} = 0.5$ and the red iso-surface indicates $\alpha_{air} = 0.1^6$.

4.5 Numerical results of large-sized bubble as Weber numbers

4.5.1 Development of bubble shape

Figure 4.6(a) illustrates the aspect ratio between the bubble diameters in the streamwise (d_{st}) and spanwise (d_{sp}) direction as various Weber numbers. Each Weber number (*We*) is based on the bubble properties, as summarized in Table 4.7. The equivalent bubble diameter (d_e) was calculated from the bubble volume (V_b). For all bubbles, d_{st} was longer than d_{sp}; in particular, at Weber numbers of 219–274, d_{sp} extended significantly with a constant d_{st}. At higher Weber numbers, the trend of the aspect ratio was similar to that at Weber numbers of 130–219.

Figure 4.6(b) shows four cases of bubbles that exhibited changes in their aspect ratio trend. The image of each case shows the instantaneous shape when the streamwise length was larger than that of the other sampling bubbles. These bubble shapes also show that the geometrical similarity was lost as the Weber number increased. In Case 1, a nearly round and symmetrical bubble shape was formed with respect to the streamwise direction. In Case 2, the front shape of the individual bubble became unstable, creating an asymmetrical shape in the main flow direction and rotating irregularly.

Meanwhile, Cases 3 and 4 exhibited different unstable features; for instance, the bubble length in the middle region showed fluctuations in Case 3, and the edge shape showed a strong curvature in the spanwise direction in Case 4. In addition, for higher Weber numbers in Case 3, the rear shape of the individual bubble was flat. The large development in streamwise and

spanwise direction over around $We = 200$ is due to constant trend of d_n as shown in Fig. 4.6(b). Furthermore, Oishi and Murai (2014) observed this feature for $We = 250$ and attributed it to the shortening of the wavelength of the capillary wave on the rear part of the bubble. This fact is consistent with our observations in Cases 3 and 4.

Table 4.7 Comparison of bubble parameters with varying Weber number; The equivalent bubble diameter, d_e, was calculated from the bubble volume, V_b.

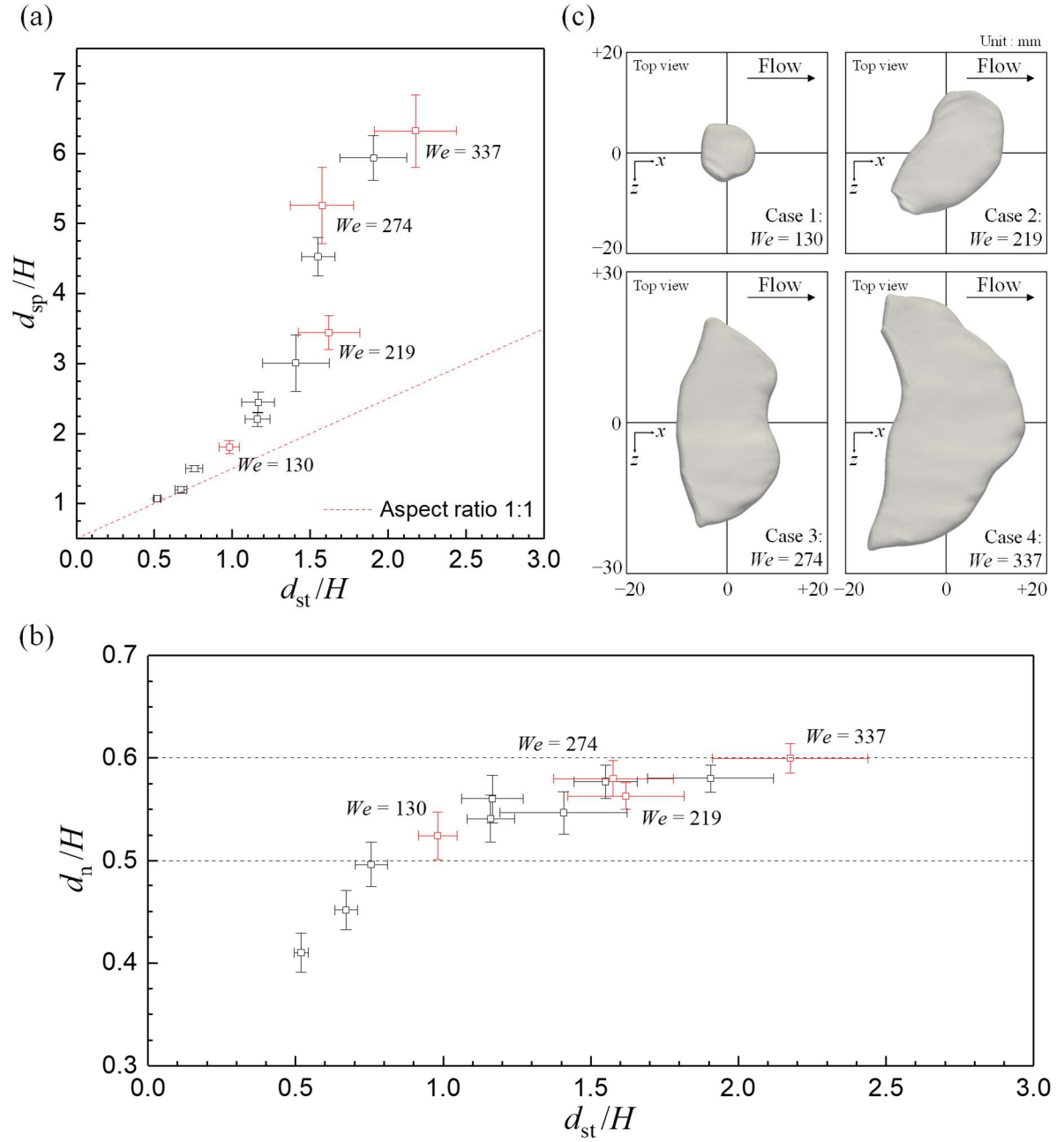| We [-]	V_b [mm^3]	d_e [mm]	U_b [m/s]	U_b/U_{mean} [-]	Name
69	63.7	4.96	0.982	0.946	
86	116.3	6.06	0.998	0.960	
106	215.7	7.44	1.007	0.970	
130	371.2	8.92	1.011	0.973	Case 1
154	585.1	10.38	1.018	0.980	
162	685.6	10.94	1.020	0.982	-
192	1035.2	12.55	1.033	0.995	-
219	1462.3	14.08	1.044	1.005	Case 2
250	2070.5	15.82	1.054	1.015	-
274	2678.0	17.23	1.056	1.016	Case 3
308	3652.1	19.11	1.063	1.023	-
337	4412.9	20.35	1.077	1.037	Case 4

Figure 4.6: (a) Bubble length ratios in streamwise and spanwise direction at different Weber numbers; (b) Bubble length ratios in streamwise and normal direction at different Weber numbers, where the error bars indicate the standard deviation of the data, and (c) Top view of four bubbles corresponding to the red point in (a) and (b).

4.5.2 Profile and local mean value of skin friction

The local skin friction profile in the streamwise direction was analyzed by averaging the local areas. Figure 4.7 shows an example of the local skin friction analysis similar to the method used by Murai et al. (2007). The local area was 10 mm in width and 10 mm in length, which is similar to the sensing area of the shear transducer in their experiment. The streamwise coordinate was defined as distance x from the rear edge of the bubble, and the dimensionless value is obtained by dividing d_{st}. So, it was between 0 and 1 on the liquid film and below 0 on the secondary flow of the bubble. A series of profiles were obtained with the bubble in the center of the channel ($L/H = 4.5$–5.5 in the streamwise direction) to avoid the pressure gradient regions near the inlet and outlet. The magnitude of skin friction (τ_w) on the xz-plane is defined by $\tau_w = (\tau_x^2 + \tau_z^2)^{0.5}$, which was divided by the skin friction of single-phase flow (τ_{w0}) to obtain a dimensionless value.

As shown in Figs. 4.8 and 4.9, several common features can be observed in all bubbles. The skin friction initially increased in the front region of the liquid film at approximately $\tau_x/\tau_{x0} = 1.2$ and then gradually decreased to achieve a minimum value between the rear part of the liquid film and front part of secondary flow. This trend is similar to that reported by Murai et al. (2007). Notably, as the Weber number increased, the minimal values of skin friction gradually decreased and reached constant range $0.6 < \tau_x/\tau_{x0} < 0.8$ for We ≥ 274. Meanwhile, the variation of the skin friction profile increased from the front side of the liquid film and the rear side of the secondary flow. This observation is attributable to the large variation in d_{st} with the increase in Weber number, as shown in Fig. 4.6(a). This also implies that the drag reduction effect on the central region of the bubble may be less than that on the overall bubble.
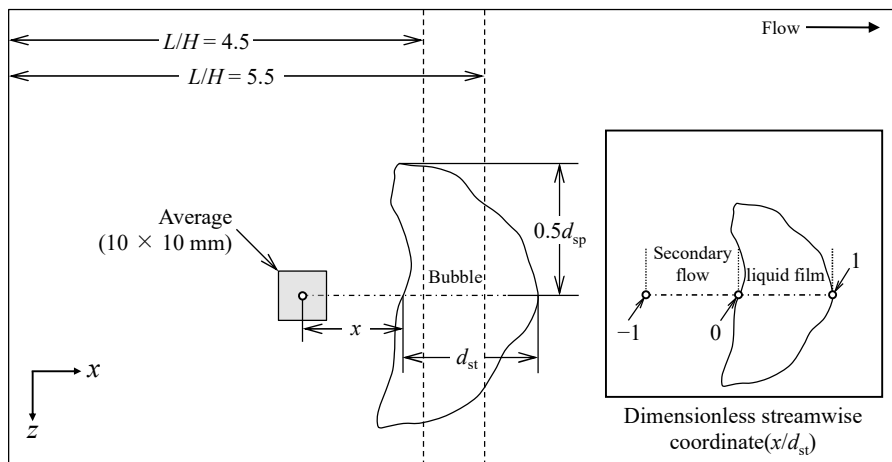

Figure 4.7: Sketch of measurement and calculation area of local skin friction; representative coordinates around the bubble are shown in the inset.
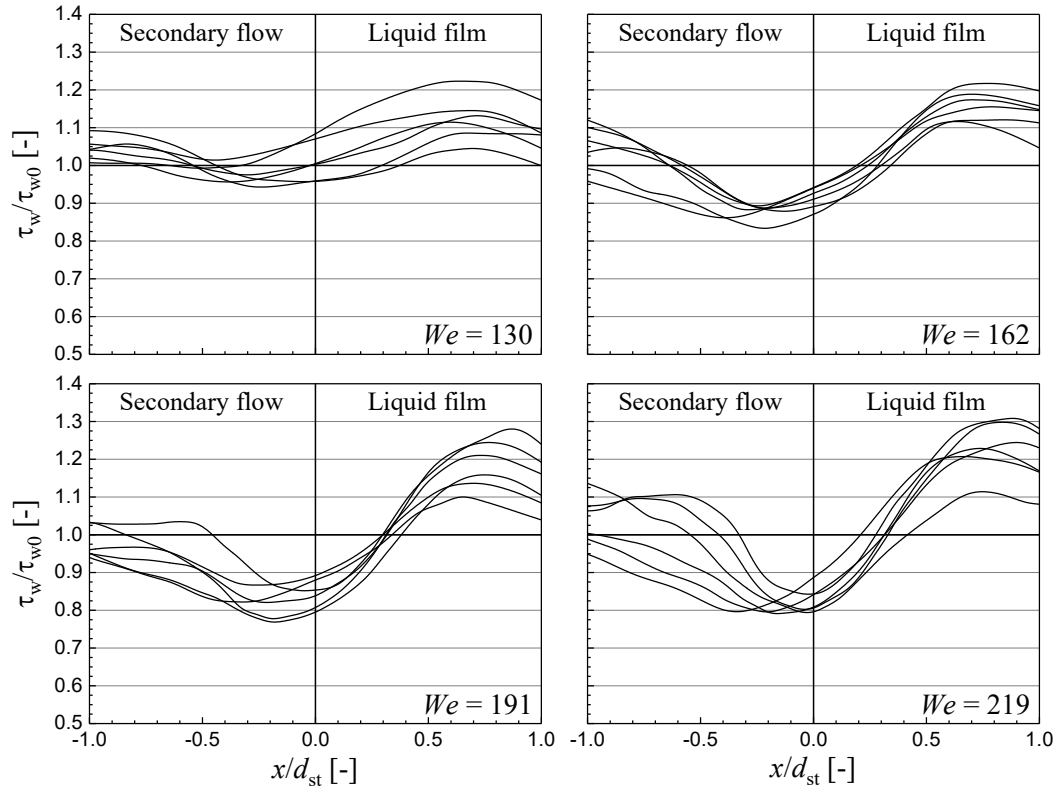
Figure 4.8: Skin friction profile along Weber numbers of 130–219 at the center of the bubble.
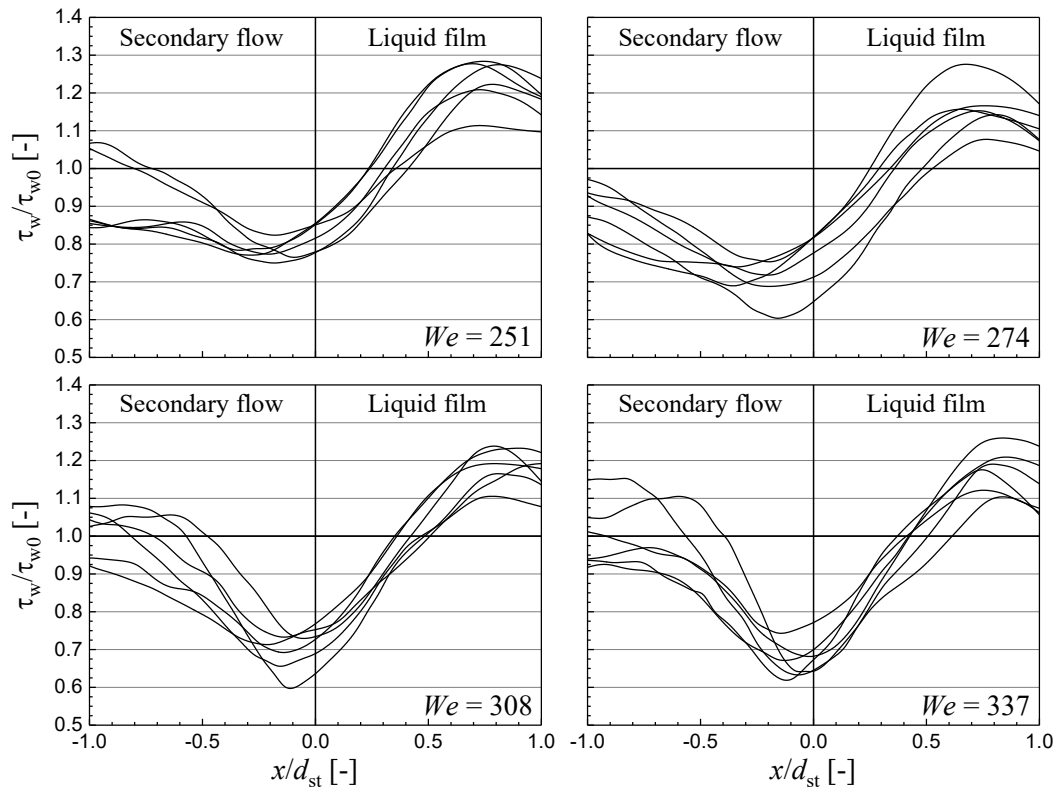

Figure 4.9: Skin friction profile along Weber numbers of 251–337 at the center of the bubble.

The effect of span location of individual bubble was examined through considering local mean ratio of skin friction in spanwise direction. Figure 4.10 shows an example analysis of the mean ratio of skin friction in a local area. Each local area was derived by dividing the entire bubble region into ten parts along the spanwise direction.

As revealed by Murai et al. (2007) who reported that the drag reduction effect is proportional to d_{st}, the length of the local area in the streamwise direction is set to twice the local bubble length in streamwise direction (λ_{lo}). The spanwise coordinate was defined as the distance z from bubble center, and the dimensionless value was obtained by dividing d_{sp}, and was set at zero on the bubble center and to 0.5 and −0.5 on the upper and bottom sides, respectively, of the bubble edge in the spanwise direction, as shown in Fig. 4.10(b).

Based on the above method, the local mean ratio of skin friction was obtained at different Weber numbers as shown in Figs. 4.11 and 4.12. In general, the local mean ratio of skin friction was higher from the span edge regions ($|z/d_{sp}| \geq 2.5$), while the center of the bubbles ($|z/d_{sp}| \leq 2.5$) showed lower mean ratio of skin friction with a smaller deviation. These trends enhance as increasing Weber number. Nevertheless, the degree of drag reduction at the center of the bubbles was found to be irregular and is considered to be the reason for the observed irregular bubble deformation. Thus, except the enhanced drag reduction as increasing Weber number, it is hard to figure out other common trends at different Weber number.

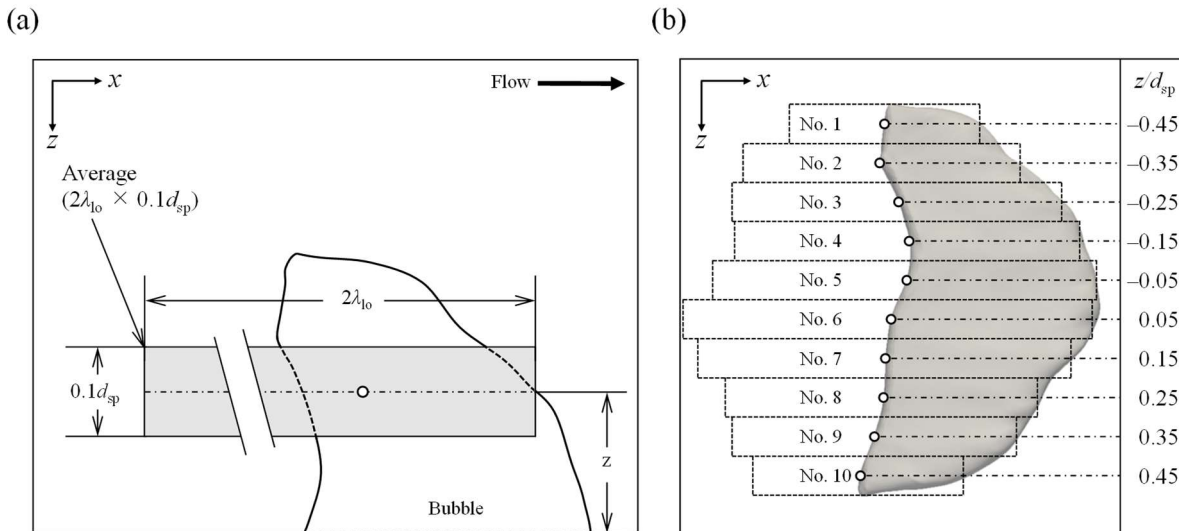Figure 4.10: (a) Sketch of measurement and calculation of local area; and (b) Example of the local areas of the entire bubble region.
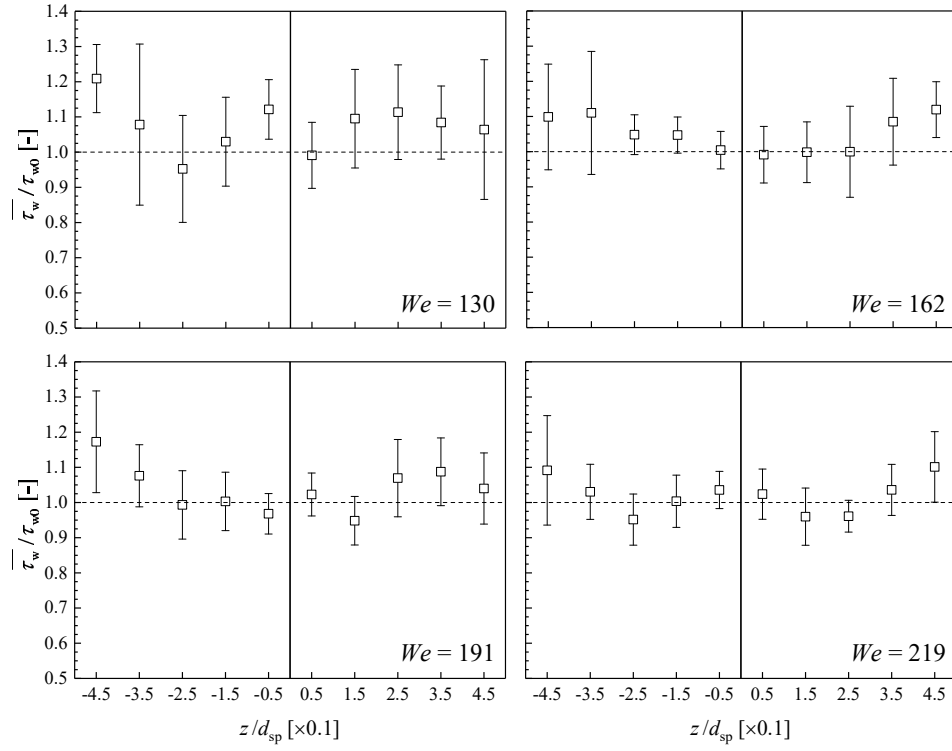
Figure 4.11: Local mean ratio of skin friction along Weber numbers of 130–219, where the error bars indicate the standard deviation of the data.
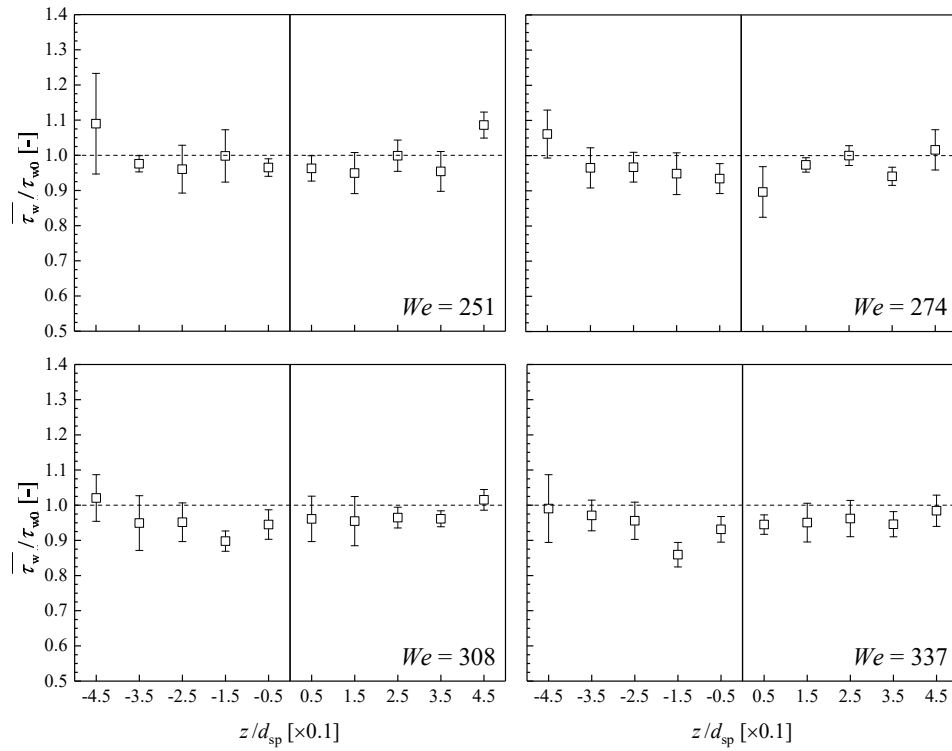

Figure 4.12: Local mean ratio of skin friction along Weber numbers of 251–337, where the error bars indicate the standard deviation of the data.

Figure 4.13 depicts the data in Figs. 4.11 and 4.12 as a scatter plot of the relationship between the local bubble length in streamwise direction and the local mean ratio of skin friction. First of all, all local bubble lengths in streamwise direction show drag reduction but the deviations between these points can be observed, especially the mean ratio of these points below $\lambda_{lo}/H = 1.0$ reached 1.4. These deviations trends decrease with an increase in λ_{lo}, and drag reduction can be considered to be achieved above the dimensionless bubble length of $\lambda_{lo}/H = 2$. This tendency is similar to the results obtained by Murai et al. (2007).
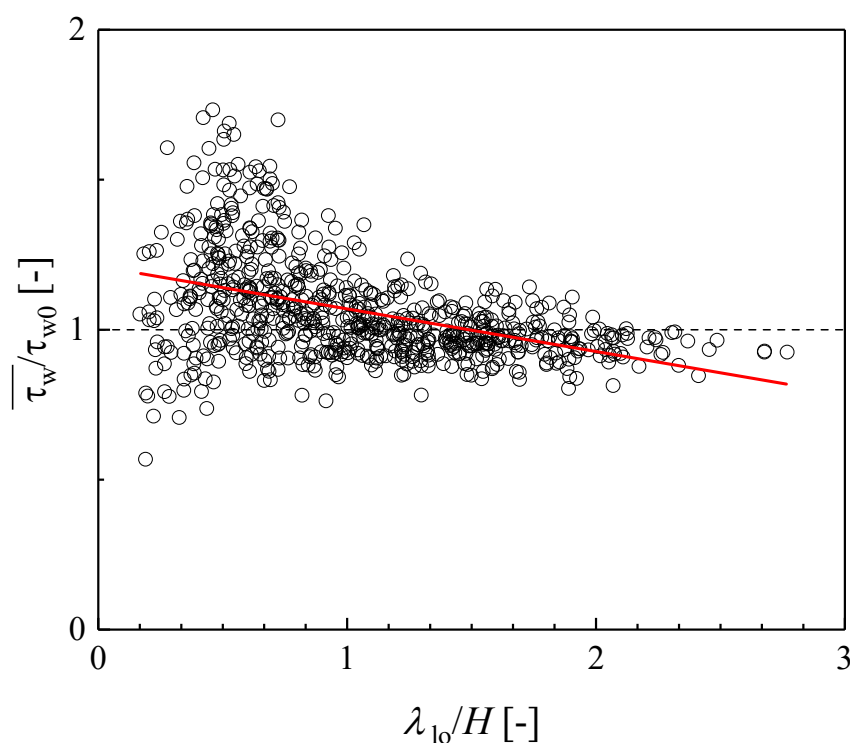

Figure 4.13: Local mean ratio of skin friction vs. bubble length; H represents the height of the channel

4.5.3 Skin friction characteristics on liquid film

Although the skin friction profile and bubble length can be used to evaluate the drag modulation, they cannot be used to analyze the characteristics of individual bubbles with irregular deformations of the bubble. Moreover, the local data do not accurately represent the entire area of the bubble at higher Weber numbers. Therefore, this section introduces an alternative approach to evaluate the general trends of drag modulation by dividing the evaluated areas, such as the liquid film and secondary regions.

First, the mean ratio of skin friction along individual bubbles in the liquid film are discussed, and Figs. 4.14(a)–(c) present a typical example of post-processing to measure the skin friction on a liquid film. The global skin friction contour in Fig. 4.14(b) is cut-off outside the outline of the projected bubble area in Fig. 4.14(a) to obtain a skin friction contour of the liquid film, as shown in Fig. 4.14(c).

The skin friction is divided into the streamwise direction (τ_x) and spanwise direction (τ_z), and the absolute values of skin friction in the spanwise direction ($|\tau_z|$) are considered because the average value of skin friction in the spanwise direction becomes near zero. Figure 4.15(a) shows that the mean ratio of skin friction in the streamwise direction of the liquid film decreased gradually with increasing Weber number. However, all cases yielded a mean ratio of skin friction greater than 1.0, except for the case with $We = 347$, wherein the mean ratio of skin friction reached the unit value.
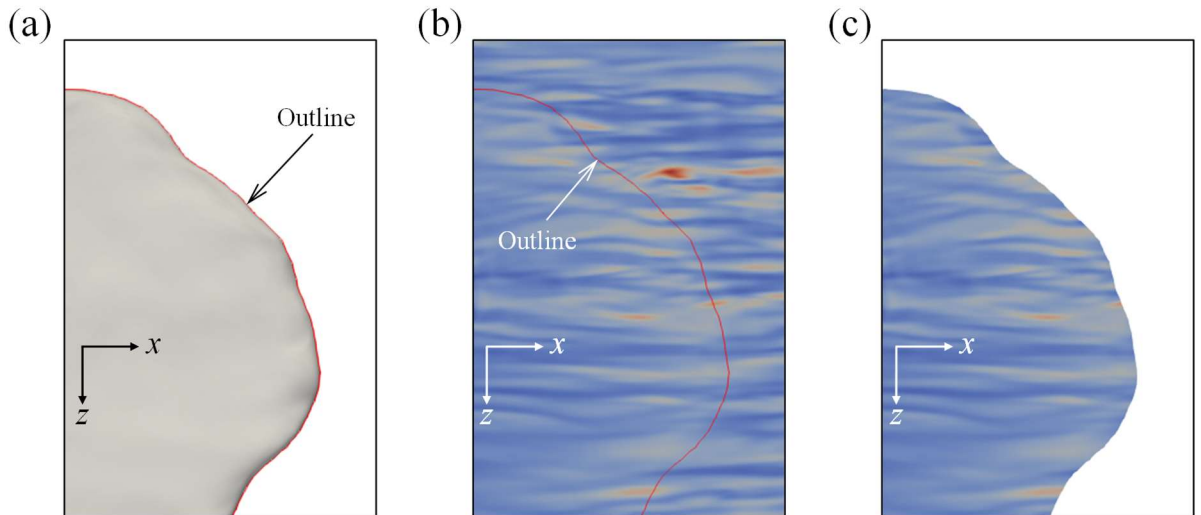

Figure 4.14: Definition of skin friction in post-processing showing: (a) and (b) the outline of the bubble and skin friction contour on the upper wall, respectively; and (c) the skin friction contour on the liquid film.

These tendencies can be deduced from Figs. 4.9 and 4.10, which show significant increases in skin friction near the front of the bubble. Meanwhile, the mean ratio of the skin friction linearly decreases from $We = 251$, this mean that assumption of the mean ratio of the skin friction at the liquid film may be able to assume based on the Weber number of the bubble if further studies are conducted greater Weber number than present work. Figure 4.15(b) shows that overall values of the mean ratio of skin friction in the spanwise direction of the liquid film were larger than those for the single-phase flow, and the mean ratio of skin friction tended to become constant at approximately 1.5 as the Weber number increased.

Figure 4.16 shows the instantaneous contour of skin friction in the streamwise direction at the liquid film for four cases. Starting with the front region of the liquid film, the turbulent flow was introduced from the front of the bubble without any disturbance. This corresponded to the increase in skin friction observable near the front region in Figs. 4.9 and 4.10. This effect persisted up to the rear part of the bubble in Case 1 and Case 2. However, the drag reduction was manifested in the rear region in Case 3 and Case 4. Therefore, it can be inferred that the drag reduction region increased with the increase in Weber number, and the increase and decrease in skin friction were offset by each other at $We = 337$. Interestingly, along the edge of the rear part of the bubble where is formed like a string-shaped drag reduction region, τ_x/τ_{x0} reached a value of almost zero independent of the size of the bubble, and the area exhibiting an increase in drag was fragmented from this region.
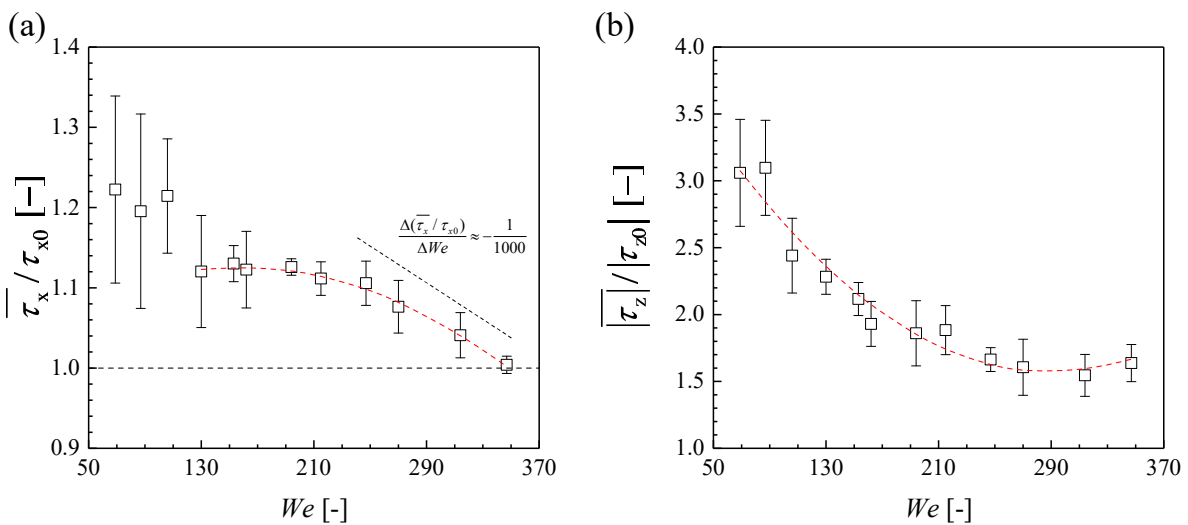

Figure 4.15: Mean ratio of skin friction at the liquid film, where the error bars indicate the standard deviation of the data: (a) streamwise direction and (b) spanwise direction.

This is consistent with the characteristics of the Taylor bubble in the stagnant flow of vertical pipe that the skin friction in the Taylor bubble rear shows a noticeable peak value reported by Araújo et al. (2012) and Massoud et al. (2018).   This Taylor bubble has a thin liquid film with the respect to the diameter of the pipe and the rear shape is a flat or convex shape. The flow condition in the present study is different from the Taylor bubble in the vertical pipe but the gravity in the wall-normal direction induced liquid film of the bubble thinner as the Weber number increase.

Figure 4.17 shows the instantaneous contour of skin friction in the spanwise direction at the liquid film for four cases. The decreasing trend of the skin friction enhanced the center of the bubble, as shown in Fig. 4.16, whereas the edge region in the spanwise direction exhibited significant skin friction. This tendency is consistent with the distribution of vortices in the streamwise direction of a liquid film observed by Kim et al. (2020).

In contrast, the edge of the rear part of the bubble, where the skin friction in the streamwise direction reached a value of almost zero, showed an increase in drag for all four cases. Especially in Case 4, the increases in drag on the rear edge of the center and even middle regions of the bubble were calmed. This implies that high velocity was generated in the spanwise direction, where the thickness of the liquid film on the outside was thicker than that at the center, or that vortices were developed in the streamwise direction in this region.
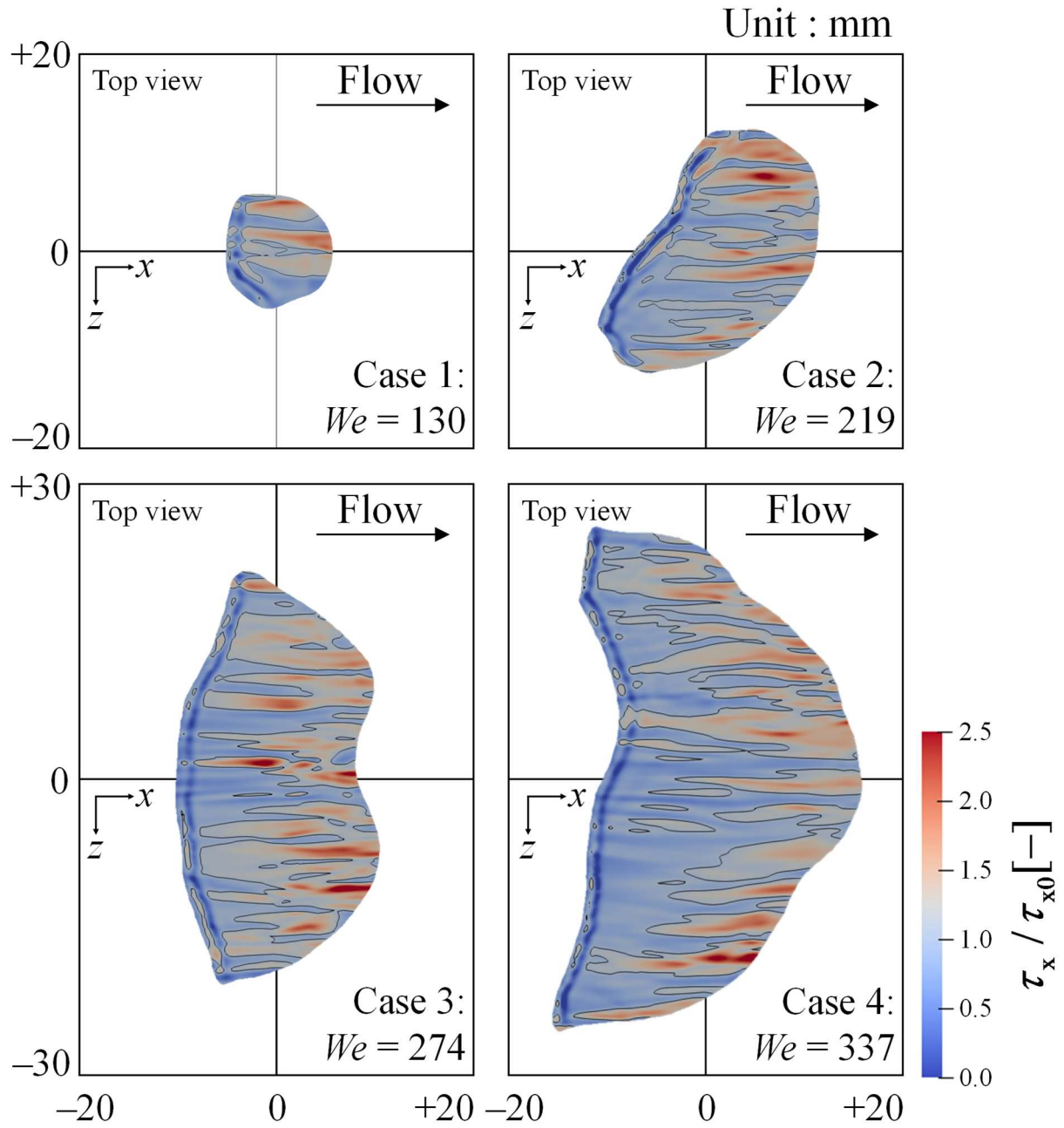
Figure 4.16: Effect of Weber number on skin friction in streamwise direction at the liquid film. The black line on the contour represents $\tau_x/\tau_{x0} = 1.0$.
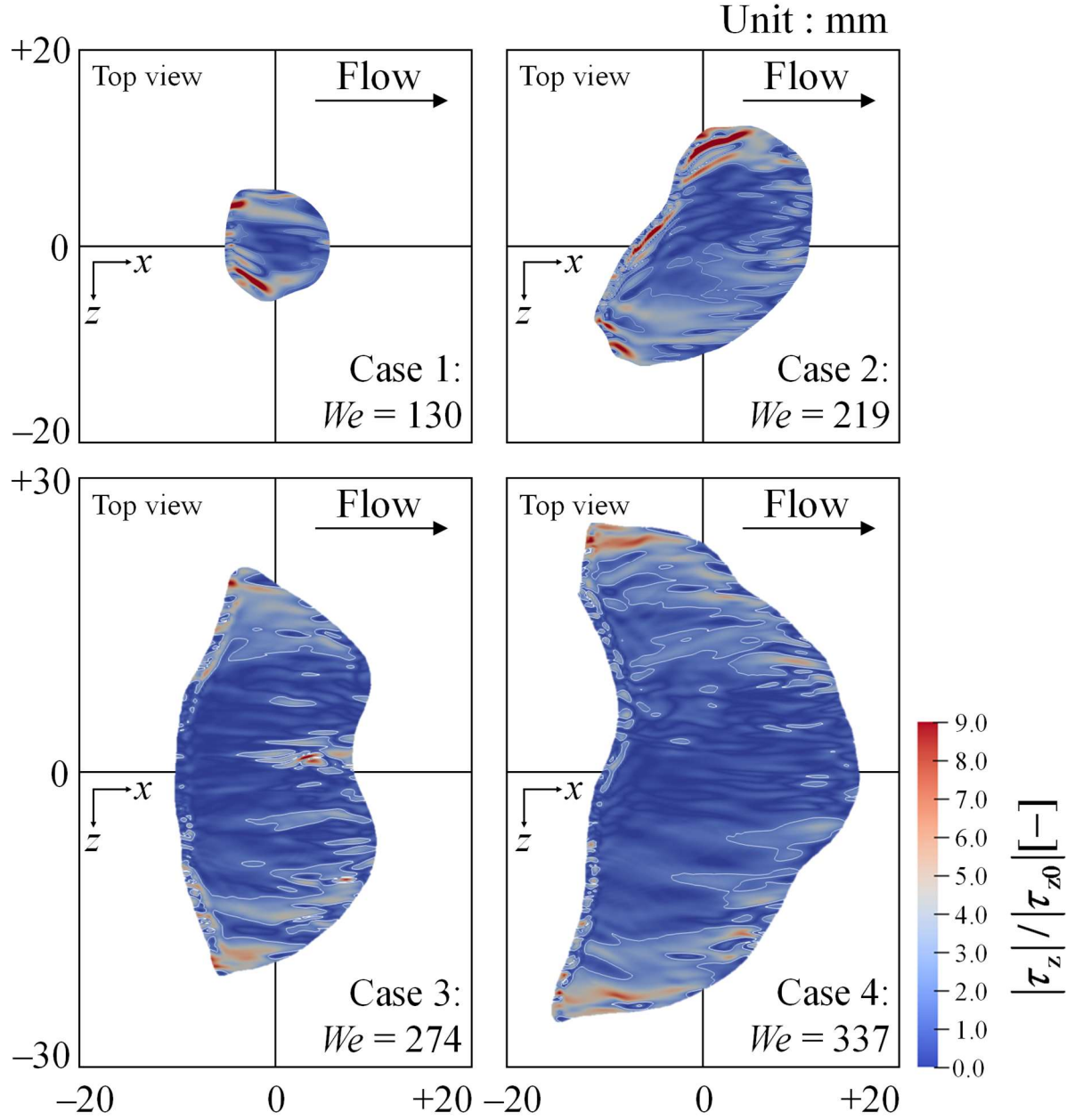
Figure 4.17: Effect of Weber number on absolute value of skin friction in the spanwise direction at the liquid film. The black line on the contour represents $\tau_z/\tau_{z0} = 1.5$

4.5.4 Skin friction characteristics on secondary flow

As shown in Figs. 4.9 and 4.10, the secondary flow region also exhibited drag reduction. Therefore, to investigate the drag modulation effect, the area of the secondary flow was evaluated as shown in Fig. 4.18. Figure 4.19(a) shows the mean ratio of skin friction in the streamwise direction at the secondary flow.

Generally, the drag reduction ratio increased as the Weber number and λ_{se} increased. Meanwhile, the drag reduction ratio began to decrease at $We = 274$ for $\lambda_{se} = 1.5d_{st}$ and $1.0d_{st}$ but monotonically increased for $\lambda_{se} = 0.5d_{st}$. Figure 4.19(b) shows the mean ratio of absolute value of skin friction in the spanwise direction at the secondary flow; for $\lambda_{se} = 0.5d_{st}$, the value almost matched with that at the liquid film, as shown in Fig. 4.15(b), and this trend gradually decreased as λ_{se} increased. In contrast, the deviation of the mean ratio of skin friction decreased as λ_{se} decreased and the Weber number increased. Eventually, this inverse proportional relationship between λ_{se} and the mean ratio of skin friction disappeared for $We = 274$ and higher.

Figure 4.20 shows the instantaneous skin friction contour in the streamwise direction of secondary flow. Case 1 showed no specific change except for drag reduction in the region closest to the bubble. This drag reduction region tilted with the rotation of the bubble in Case 2, and a high drag increase was observed around the bottom side of the bubble. In Case 3 and 4, the drag reduction region expanded, especially in the central region of the bubble.

At the same time, a region of high drag increase was also observed on the side of the secondary flow and behind the region of drag reduction. In addition, there were many small fragments of drag increase behind the bubble; these locations were consistent with the rear edge of a liquid film, which showed a high skin friction ratio in the spanwise direction, as illustrated in Fig. 4.17. This implies that high velocity flow or vortices in the streamwise direction were generated from the rear edge of the liquid film and persisted in the secondary flow.

Figure 4.21 shows the instantaneous skin friction contour in the spanwise direction at the secondary flow. For all cases, a region showing high skin friction can clearly be observed to originate from both the span edge of the secondary flow and the span edge of the bubble, where high skin friction of the liquid film was observed, as shown in Fig. 4.17. For Case 2, the region near the bottom side of the bubble showed a higher skin friction ratio than that near the upper side of the bubble.

This asymmetric trend was also observed in the liquid film, as shown in Fig. 4.17. Furthermore, the location of this region corresponded with that of the higher skin friction in the

streamwise direction, as shown in Fig. 4.20. This implies that high velocity flow or vortices in the streamwise direction were generated from the span edge of the bubble and induced the drag increase in the secondary flow.
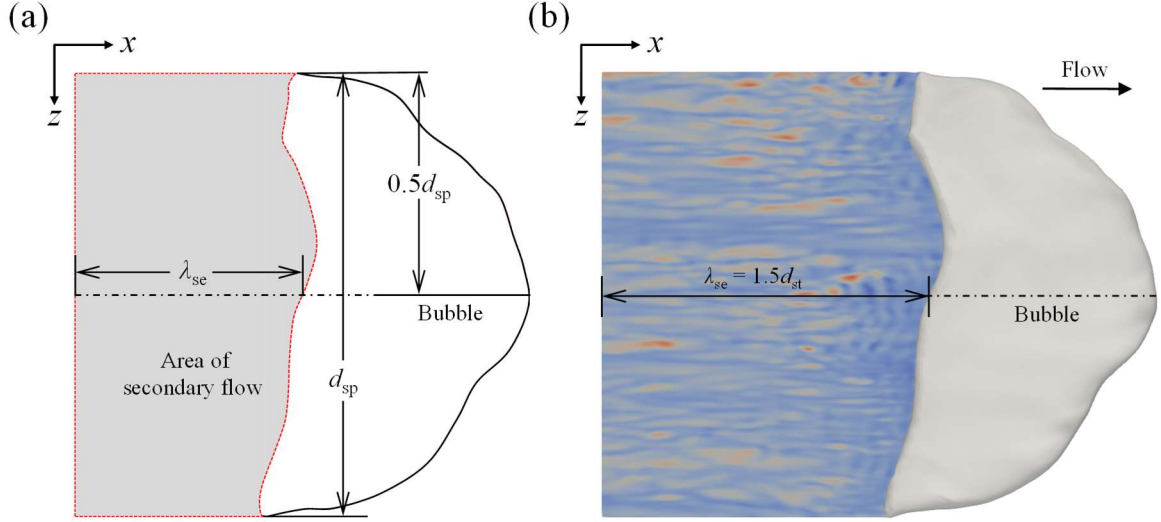
Figure 4.18: (a) Sketch of secondary flow area measurement and calculation, (b) Example of the secondary flow.
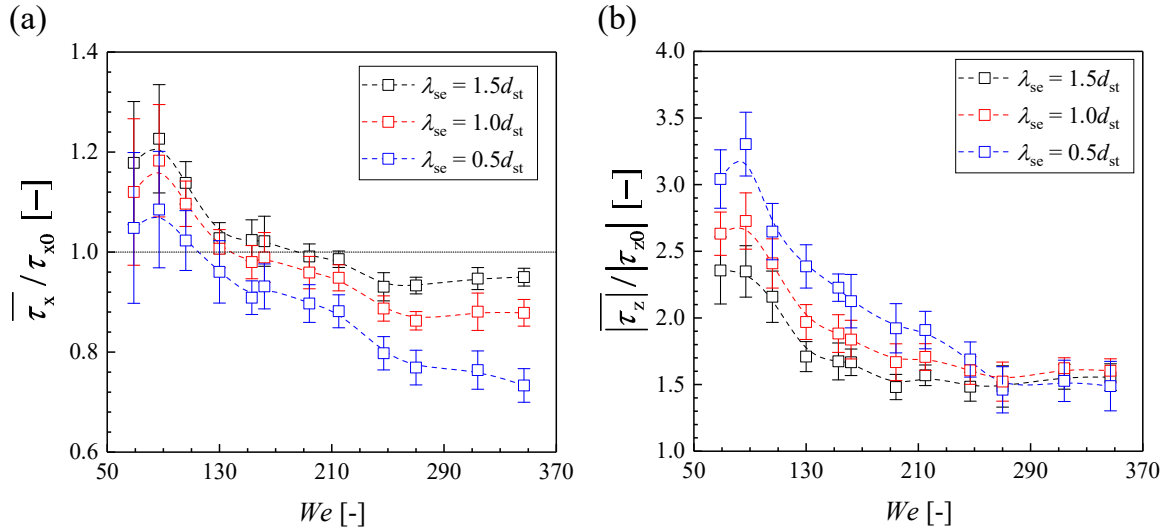
Figure 4.19: Mean ratio of skin friction of secondary flow with varying λ_{se} in the (a) streamwise direction, and (b) spanwise direction, where the error bars indicate the standard deviation of the data.
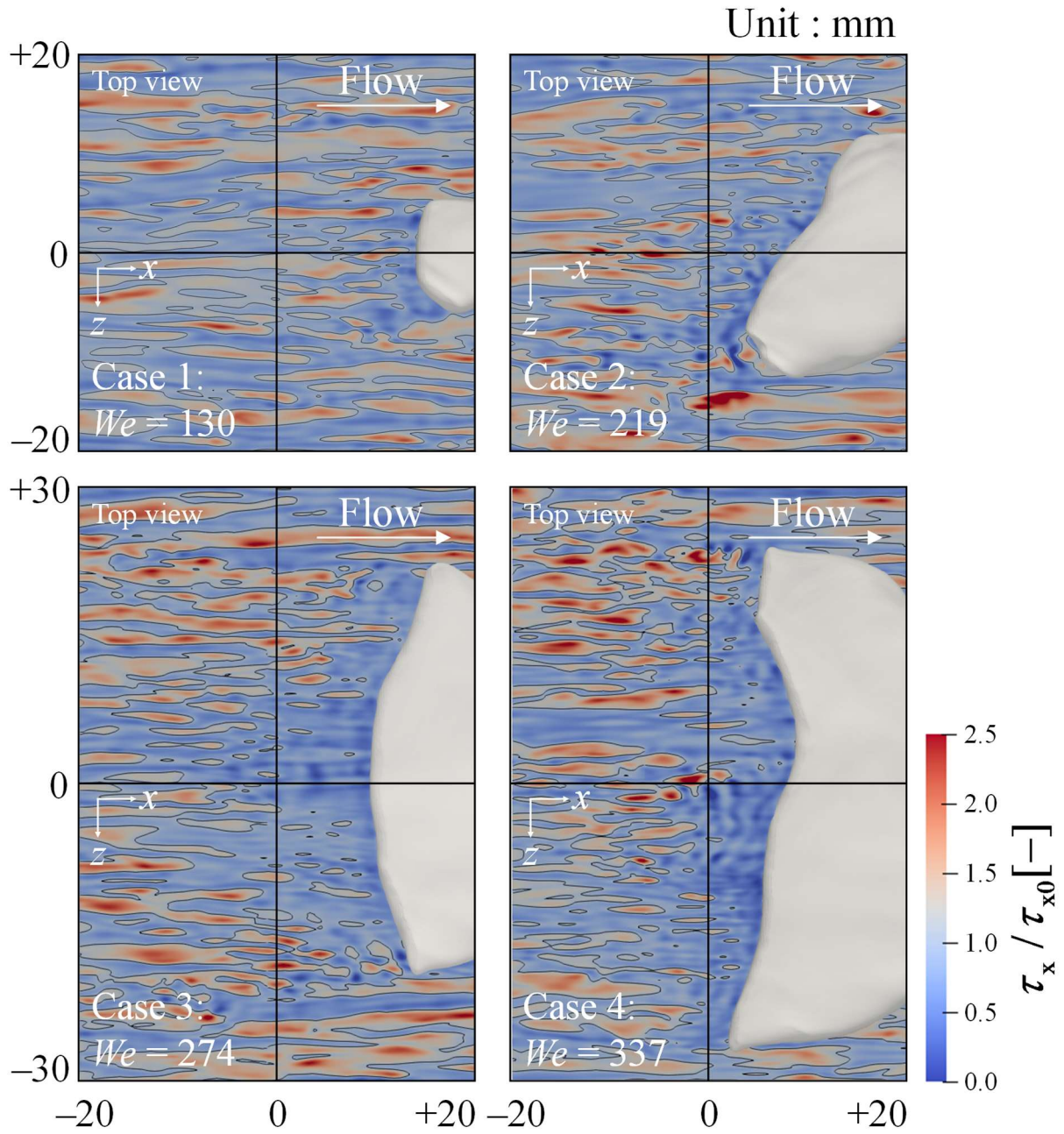
Figure. 4.20: Effect of Weber number on skin friction in the streamwise direction at the secondary flow. The black line on the contour represents $\tau_x/\tau_{x0} = 1.0$.
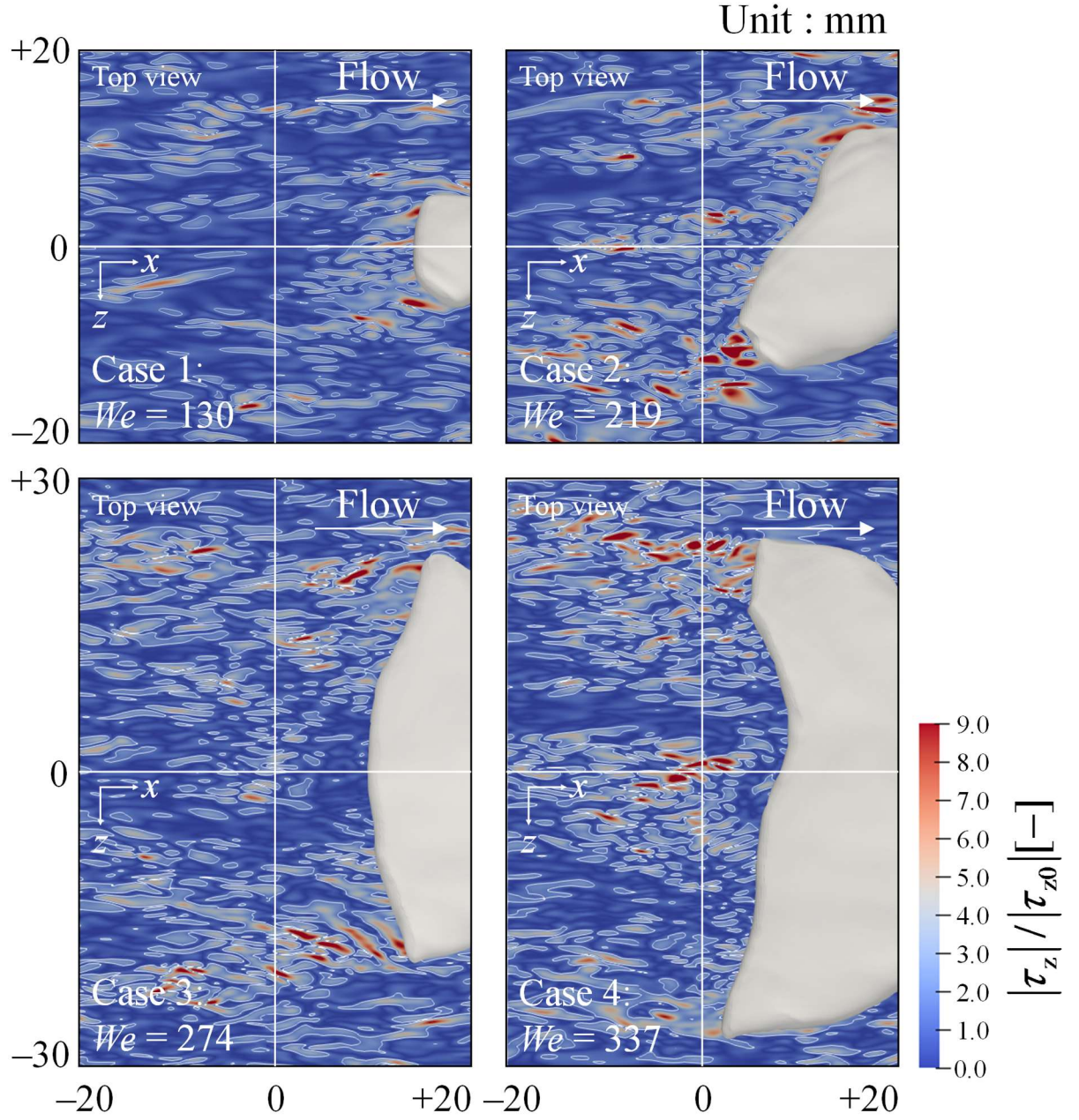
Figure 4.21: Effect of Weber number on skin friction in the spanwise direction at secondary flow. The white line on the contour represents $\tau_z/\tau_{z0} = 1.5$.

4.5.5 Spatial average of skin friction in streamwise direction

The spatial average of skin friction in the streamwise direction was analyzed, and Figs. 4.22(a)–(c) present a typical example of post-processing, which measures the spatial average of skin friction. The original skin friction contour is presented in Fig.4.22(a), which shows the distance from the center of the bubble to the center of the domain. The bubble center is transferred to the domain center, as shown in Fig. 4.22(b), and this process is applied in total time steps, as shown in Fig. 4.22(c). As a result, the example of the spatial average is as shown in Fig. 4.22(d); the averaged skin friction is normalized by the skin friction of single-phase flow. Although the coherent turbulent structure is still visualized after the spatial average, it shows a distinctive feature, as the Weber number increases.
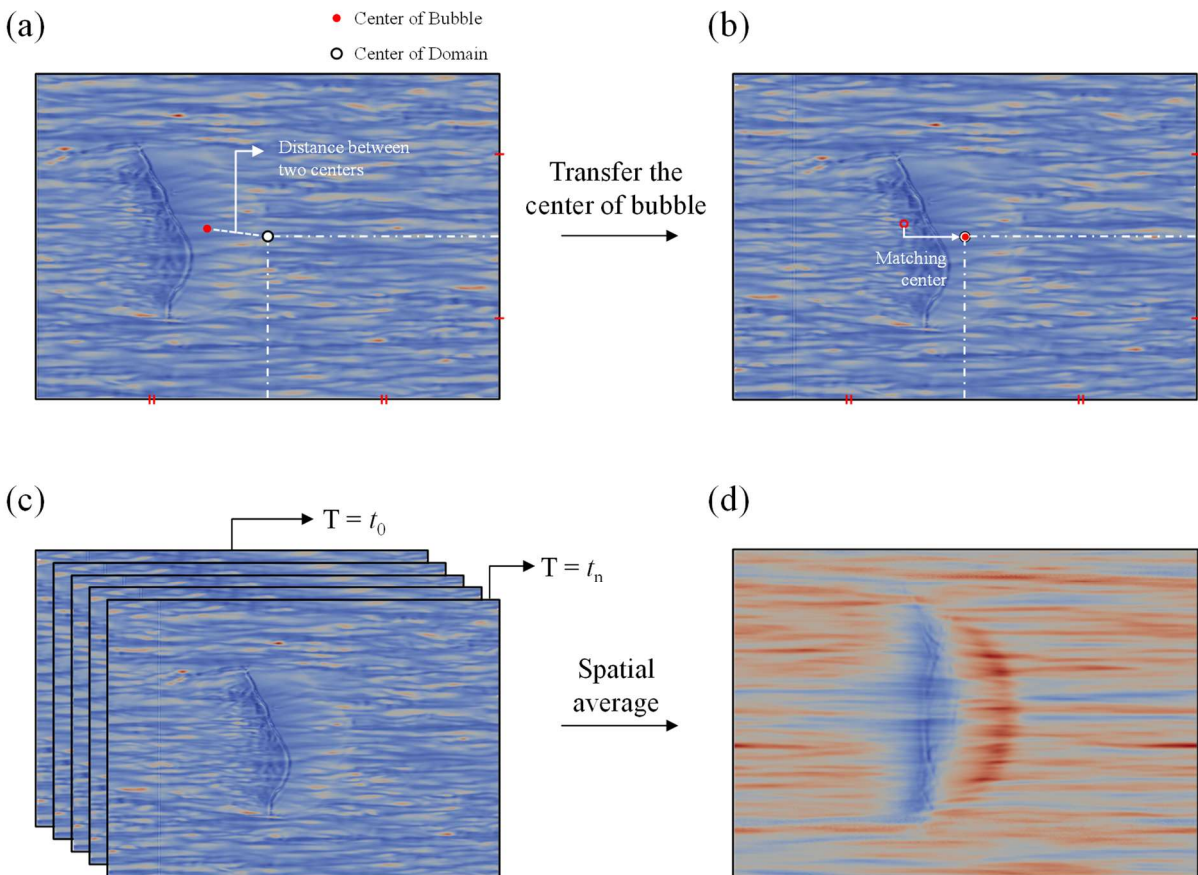

Figure 4.22: Definition of spatial skin friction in post-processing: (a) original contour of skin friction with distance between two centers, (b) transferred bubble center to domain center, (c) spatial averaging for total time-steps, and (d) example result of spatially averaged skin friction contour.

For all bubbles, the features of skin friction can be divided into three categories. First, Weber numbers 69–106 show high skin friction in the entire region of the liquid film without the relaminarization, as reported by Park et al. (2019), and the bubble shape estimated by the distribution of skin friction in the liquid film is relatively spherical. Interestingly, these high skin frictions are also observed in the secondary flow, and this region is broadened with an increase in the length of the secondary flow, while drag reduction occurs in the vicinity of this region. This feature is sustained until the Weber number 106 and is considered to be related to the local high skin friction region, which forms a horseshoe shape (section 3.5.3).

At Weber numbers 130–250, the drag reduction occurs from behind the bubble, and this region is broadened. Moreover, the high skin friction at the secondary flow disappears. In addition, skin friction on liquid film still shows high skin friction with the striped pattern in a streamwise direction. However, relaminarization is observed at a small portion near the capillary wave region. The expected bubble shapes are ellipsoidal. Finally, at Weber numbers 274–337, the drag reduction shows near the bubble center, while curving to the back in the outer region. In addition, the front side of the bubble shows high skin friction with the striped pattern in a streamwise direction, and the expected bubble shapes are crescent arcs.

These universal features for increasing the drag from the front side and decreasing it on the rear side with relaminarization in the middle of the liquid film can be deduced from Fig. 4.26. Figure 4.26 shows the isosurface of the instantaneous momentum flux defined in Sections 3.5.2 via equations 3.7 and 3.8, with an instantaneous bubble shape. Generally, a negative momentum flux is formed in the front side and is considered drag increment, while positive momentum flux occurs at the rear side and considered as drag reduction. These formations are owing to the curvature effect where show high curvature around the bubble and cause sudden contraction and enlargement. Between the negative and positive momentum fluxes, there is a large area with the transition of momentum flux because of too thin to show large momentum flux, and increases as the Weber number increases. Thus, the balance of curvature effect of front region and relaminarization of the liquid film including curvature effect of the rear region is considered to cause trend of total drag increase or decrease of the large-sized bubble as shown in Fig. 4.27.
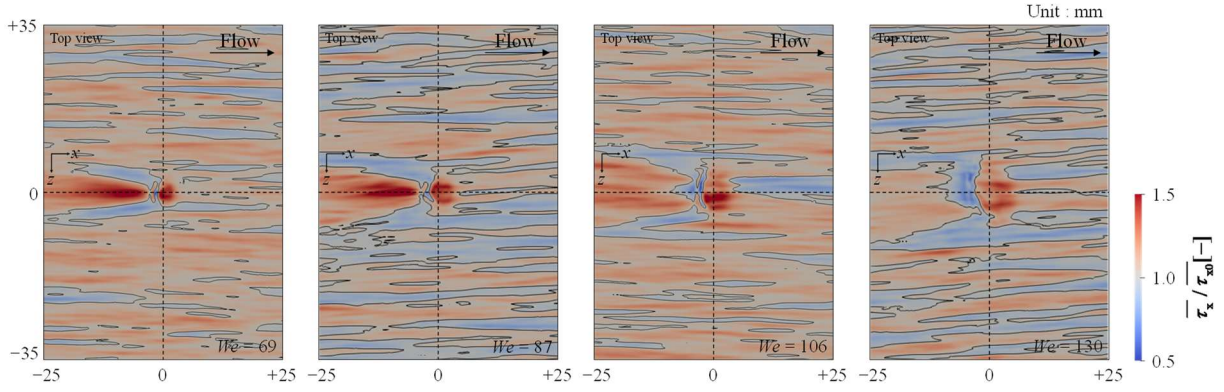
Figure 4.23: Spatial average of skin friction in the streamwise direction for We = 69–130. The black line on the contour represents $\overline{\tau_x} / \overline{\tau_{x0}} = 1.0$.

Figure 4.24: Spatial average of skin friction in the streamwise direction for We = 154–219. The black line on the contour represents $\overline{\tau_x} / \overline{\tau_{x0}} = 1.0$.

Figure 4.25: Spatial average of skin friction in the streamwise direction for We = 250–337. The black line on the contour represents $\overline{\tau_x} / \overline{\tau_{x0}} = 1.0$.

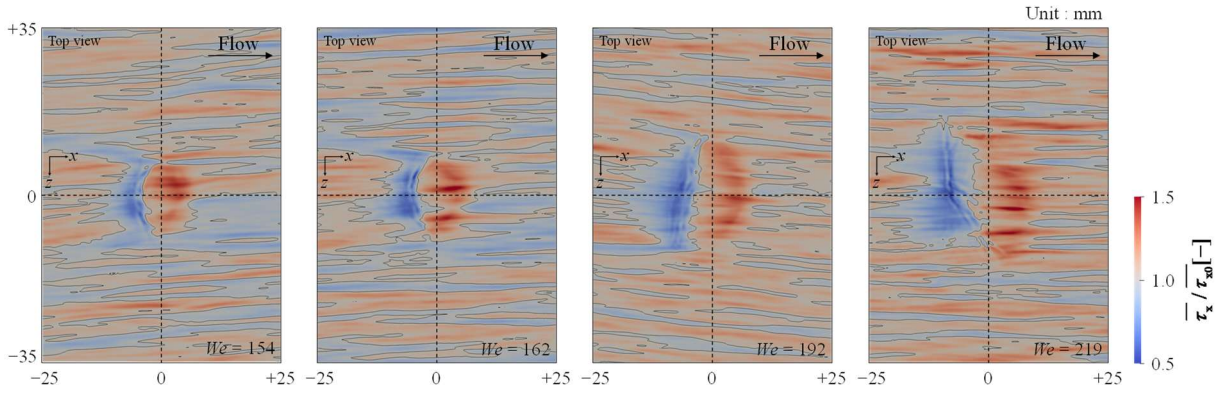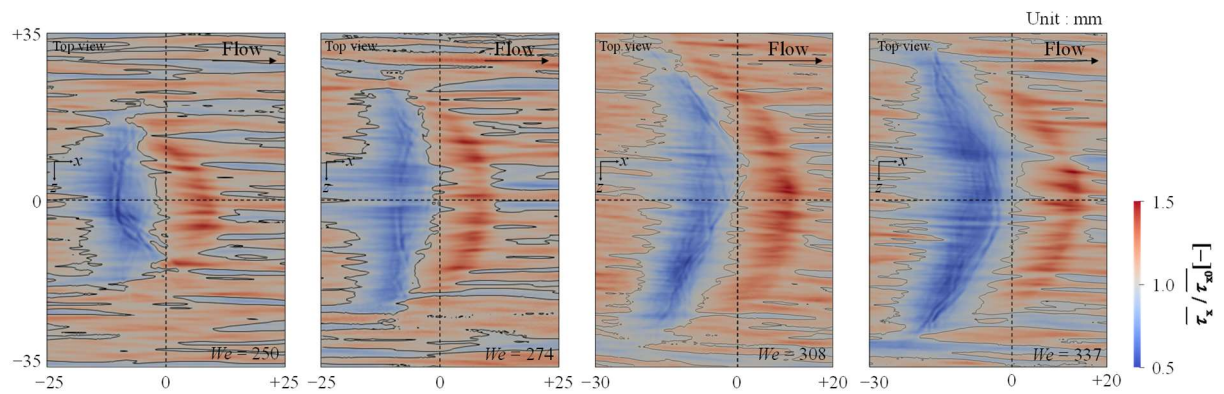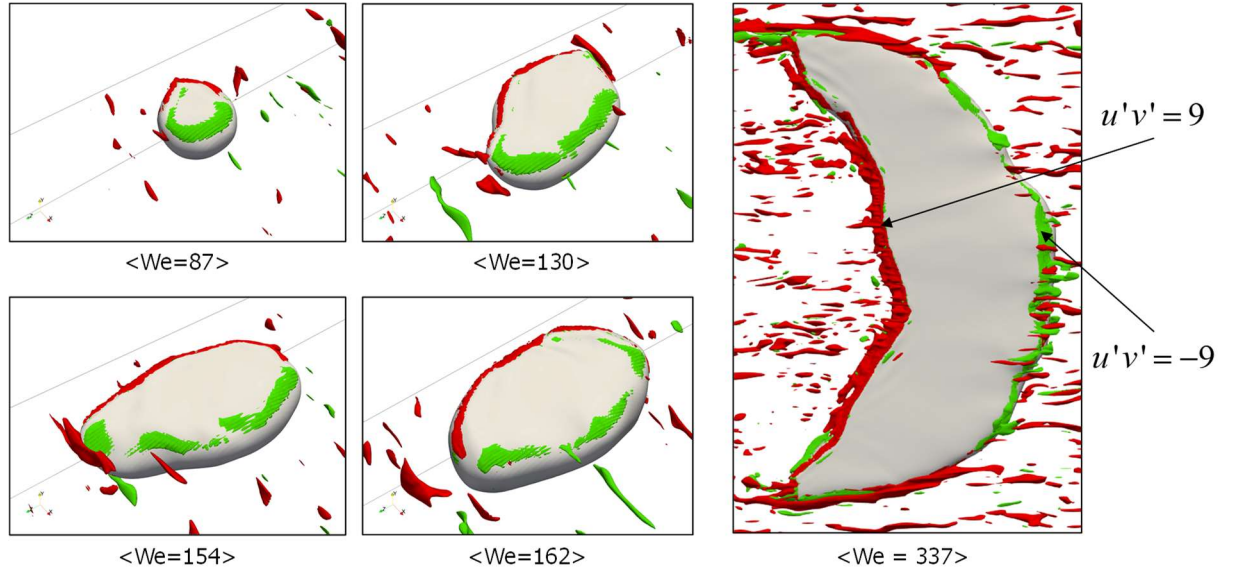Figure 4.26: Iso-surface of instantaneous momentum flux on bubble surface.
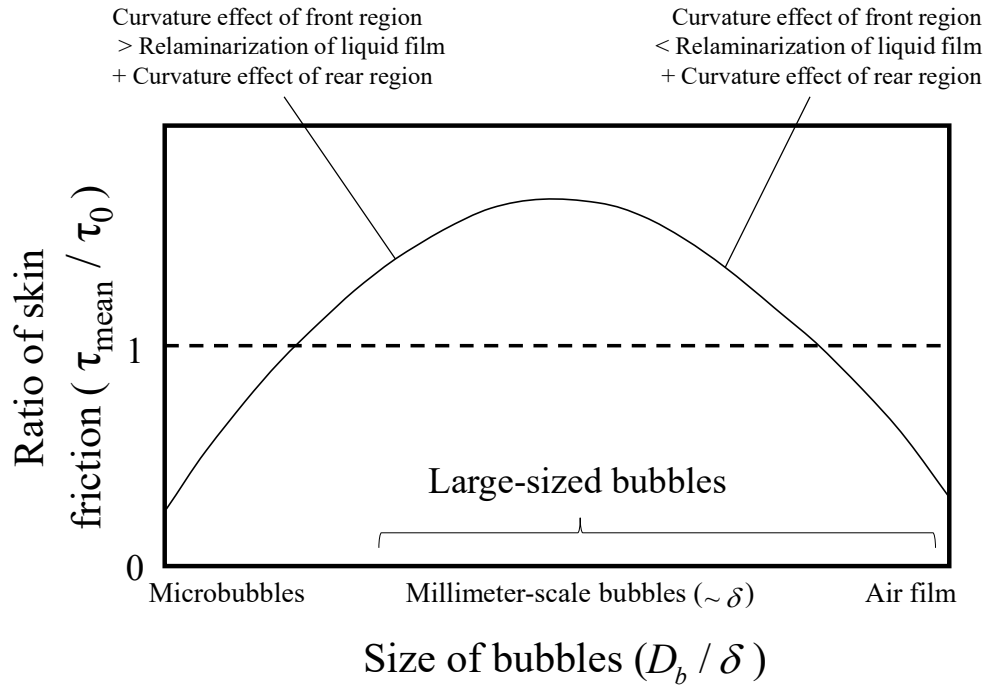

Figure 4.27: Skin friction increase and decrease as the balance between curvature effect of front region and relaminarization of liquid film including curvature effect of rear region.

4.6 Conclusion

In this study, DNSs of a series of large-sized bubbles were conducted to analyze their drag modulation effect, and the following results were obtained. i) The local skin friction profile of the core region of the bubble exhibited a uniform trend, such as an increase near the front region and a decrease near the rear region of the liquid film; the minimal value of local skin friction decreased with increasing Weber number. Considering the mean ratio of skin friction to define each local area, drag reduction was first observed in the core region at $We = 191$ and extended in the spanwise direction at larger Weber numbers. The local mean ratio of skin friction then decreased with increasing λ_{lo}.

ii) The mean ratio and instantaneous contours of skin friction were analyzed for the liquid film and secondary flow regions in the streamwise and spanwise directions. In the case of the skin friction in the streamwise direction, we observed a region of drag increase whose shape corresponded with the turbulent flow beginning from the front side of the liquid film. This region became smaller as the Weber number increased. Owing to this feature, the mean ratio of skin friction in the streamwise direction was generally greater than unity, eventually converging to the unit value with the continued increase in Weber number. This observation indicates that it is hard to achieve drag reduction in the bubble using only the liquid film. This lack of drag reduction performance was recovered from the secondary flow, and an effective λ_{se} was obtained. In addition, the drag reduction region was observed to form behind the center of the bubble.

iii) In contrast, the absolute value of the skin friction in the spanwise direction was shown by the mean ratio trend to increase as the Weber number decreased. From the instantaneous contours, the skin friction was observed to concentrate on the span edge of the liquid film and continue to the secondary flow. This trend might not be important for drag reduction in the streamwise direction; however, the instantaneous contours in the spnawise direction clearly showed that high skin friction corresponded to this trend in the streamwise direction. Indeed, the observed skin friction in the spanwise direction is a good indicator implying that high momentum flux occurred in this region. Note that the findings obtained by this study were confined to the single bubble condition. To expand these findings to practical applications such as ship drag reduction, further studies will be performed on the interactions between multiple large-sized bubbles to confirm the resulting changes in drag modulation.

References

[1] Kim, S.W., Oshima, N., Murai, Y., and Park, H.J., 2020, Direct Numerical Simulation for Drag reduction effect of a Single Intermediate-sized Bubble, *Proc. Fluid Eng. Division.* 2020.

[2] Hibiki, T., and Ishii, M., 2002. Interfacial area concentration of bubbly flow systems. *Chem. Eng. Sci.* 57(18), pp. 3967–3977.

[3] Lu, J., and Tryggvason, G., 2006. Numerical study of turbulent bubbly downflows in a vertical channel. *Phys. Fluids* 18(10), 103302.

[4] Lu, J., and Tryggvason, G., 2007. Effect of bubble size in turbulent bubbly downflow in a vertical channel. *Chem. Eng. Sci.* 62(11), pp. 3008–3018.

[5] Lu, J., and Tryggvason, G., 2008. Effect of bubble deformability in turbulent bubbly upflow in a vertical channel. *Phys. Fluids* 20(4), 040701.

[6] Lu, J., and Tryggvason, G., 2013. Dynamics of nearly spherical bubbles in a turbulent channel upflow. *J. Fluid Mech.* 732, pp. 166–189.

[7] Lu, J., and Tryggvason, G., 2018. Direct numerical simulations of multifluid flows in a vertical channel undergoing topology changes. *Phys. Rev. Fluids* 3(8), 084401.

[8] Lu, J., and Tryggvason, G., 2019. Multifluid flows in a vertical channel undergoing topology changes: Effect of void fraction. *Phys. Rev. Fluids* 4(8), 084301.

[9] McCormick, M., and Bhattacharyya, R., 1973. Drag reduction of a submersible hull by electrolysis. Nav. Eng. J. 85(2), pp. 11–16.

[10] Kanai, A., and Miyata, H., 2001. Direct numerical simulation of wall turbulent flows with microbubbles. *Int. J. Numer. Meth. Fluids* 35(5), pp. 593–615.

[11] Xu, J., Maxey, M.R., and Karniadakis, G.E., 2002. Numerical simulation of turbulent drag reduction using micro-bubbles. *J. Fluid Mech.* 468, pp. 271–281.

[12] Ferrante, A., and Elghobashi, S., 2004. On the physical mechanisms of drag reduction in a spatially developing turbulent boundary layer laden with microbubbles. *J. Fluid Mech.* 503, pp. 345–355.

[13] Pang, M.J., Wei, J.J., and Yu, B., 2014. Numerical study on modulation of microbubbles on turbulence frictional drag in a horizontal channel. *Ocean Eng.* 81, pp. 58–68.

[14] Zhang, X., Wang, J., Wan, D., 2020. Euler–Lagrange study of bubble drag reduction in turbulent channel flow and boundary layer flow. *Phys. Fluids* 32(2), 027101.

[15] Moriguchi, Y., and Kato, H., 2002. Influence of microbubble diameter and distribution

on frictional resistance reduction. *J. Mar. Sci. Technol.* 7(2), pp. 79–85.

[16] Kawamura, T., Moriguchi, Y., Kato, H., Kakugawa, A., and Kodama, Y., 2003. Effect of bubble size on the microbubble drag reduction of a turbulent boundary layer. *Proc. ASME/JSME Fluids Eng. Conf. Summer Meeting 2003*, pp. 647-654.

[17] Shen, X., Ceccio, S.L., and Perlin, M., 2006. Influence of bubble size on micro-bubble drag reduction. *Exp. Fluids* 41(3), 415–424.

[18] Lu, J., Fernandez, A., and Tryggvason, G., 2005. The effect of bubbles on the wall drag in a turbulent channel flow. *Phys. Fluids* 17(9), 095102.

[19] Sugiyama, K., Kawamura, T., Takagi, S., and Matsumoto, Y., 2005. Recent Progress of Microbubble Flow Simulation for Elucidating Drag Reduction Mechanism. *Proc. of the 6th Symp. on Smart Control of Turbulence*, pp. 191–202.

[20] Kawamura, T., 2005. Numerical and experimental investigation the mechanism of the microbubble drag reduction. *Proc. 6th Symposium Smart Control of Turbulence.*

[21] Spandan, V., Verzicco, R., and Lohse, D., 2017. Deformable ellipsoidal bubbles in Taylor-Couette flow with enhanced Euler-Lagrangian tracking. *Phys. Rev. Fluids* 2(10), 104304.

[22] Murai, Y., 2014. Frictional drag reduction by bubble injection. *Exp. Fluids* 55: 1773.

[23] Murai, Y., Fujii, H., Tasaka, Y., and Takeda, Y., 2006. Turbulent bubbly channel flow investigated by ultrasound velocity profiler. *J. Fluid Sci. Technol.* 1(1), pp. 12–23.

[24] Murai, Y., Fukuda, H., Oishi, Y., Kodama, Y., and Yamamoto, F., 2007. Skin friction reduction by large air bubbles in a horizontal channel flow. *Int. J. Multiphase Flow* 33(2), pp. 147–163.

[25] Oishi, Y., and Murai, Y., 2014. Horizontal turbulent channel flow interacted by a single large bubble. Exp. Therm. Fluid Sci. 55, pp. 128–139.

[26] Park, H.J., Tasaka, Y., and Murai, Y., 2019. Bubbly drag reduction investigated by time-resolved ultrasonic pulse echography for liquid films creeping inside a turbulent boundary layer. *Exp. Therm. Fluid Sci.* 103, pp. 66–77.

[27] Brackbill, J.U., Kothe, D.B., and Zemach, C., 1992. A continuum method for modeling surface tension. *J. Comput. Phys.* 100(2), pp. 335–354.

[28] Kim, S.W., Oshima, N., Murai, Y., and Park, H.J., 2020. Numerical investigation of a single intermediate-sized bubble in horizontal turbulent channel flow. *J. Fluid Sci. Technol.* 15(3).

[29] Roache, P.J., 1998. Verification and Validation in Computational Science and

Engineering. Hermosa Publishers, Albuquerque, New Mexico.

[30] Araújo, J., Miranda, J., Pinto, A., and Campos, J., 2012. Wide-ranging survey on the laminar flow of individual Taylor bubbles rising through stagnant Newtonian liquids. *Int. J. Multiphase Flow*, 43, pp. 131–148.

[31] Massoud, E.Z., Xiao, Q., El-Gamal, H.A., and Teamah, M.A., 2018. Numerical study of an individual Taylor bubble rising through stagnant liquids under laminar flow regime. *Ocean Eng.* 162, pp. 117–137.

Characteristics of a single large-sized bubble in turbulent Couette channel flow

Contents

Preface

The aim is to investigate the bubble deformation in turbulent Couette channel flow, which lacks experimental and numerical studies. In this chapter, several series of large-sized bubbles deformed by turbulent Couette flow were visualized, and we investigated the reason for the deformation of the bubble dynamically. This study was presented at Kim et al. (2021).

Abstract

Many experiments on the bubble for the air lubrication system of a ship were conducted on the channel flow to investigate the bubble dynamics. The model ship was then applied to evaluate and investigate the drag reduction performance. large-sized bubbles were also studied using the aforementioned procedure. However, owing to the different flow conditions such as Poiseuille flow in channel flow and Couette flow on the ship surface, different deformations of the large-sized bubble were expected; however, no study has investigated this aspect. Therefore, the intermediate condition shared from both the channel and ship surface is needed, but it is difficult to generate the turbulent Couette flow in the channel and to measure the shear stress on the wall surface, owing to the moving wall. In this study, large-sized bubbles in turbulent Couette channel flow are investigated numerically to determine the common characteristics of large-sized bubbles from turbulent Couette flow. Three different bubble sizes were chosen to compare the bubble characteristics. By comparing the different sizes of bubble cases with the bubble evolution, velocity, and thickness ratio of the liquid film, we determined the characteristics of bubbles that are distinguished from those in turbulent Poiseuille flow.

5.1 Introduction

Recently, large-sized bubbles have attracted industrial demand as a material for air lubrication systems for the drag reduction of ships, which is easier to generate than microbubbles and air films. Murai et al. (2006) reported that large-sized bubbles provided a velocity gradient that calmed the wake region. The performance of large-sized bubbles for BDR was later found to be dependent on the bubble length (Murai et al., 2007; Oishi and Murai, 2014). In addition to the velocity gradient in the wake region, it is assumed that the liquid film between the bubbles and the wall reduces skin friction by relaminarizing the flow in the film. From this perspective, Park et al. (2019) experimentally investigated the relationship between film thickness and BDR.

This physical mechanism of the large-sized bubble originates from its deformation induced by complex parameters such as shear stress around the bubble and its buoyancy. Additional details of the flow physics have been reported by Murai (2014). These studies were conducted on a horizontal channel to investigate bubbly flow characteristics or control parameters, and then established an effective air lubrication system for applying the model ship test. The difference in flow conditions between the horizontal channel and the model ship is noteworthy.

In short, the horizontal turbulent channel flow is induced by the pressure gradient, whereas the ship surface flow is induced by the ship wall velocity. This difference may have a minor effect on the micro- and sub-millimeter bubbles, which have a spherical shape and less deformability; however, large-sized bubbles are not expected to show the same shape between the two conditions because of their large deformation and thus affect the drag reduction mechanism. This perspective has not yet been confirmed and motivated in the present study.

5.2 Characteristics of large-sized bubble under flow conditions

The large-sized bubble formation under the flow conditions is illustrated in Fig. 5.1. Generally, the surrounding flow on a single large-sized bubble under horizontal turbulent channel flow (shown in Fig. 5.1.(a)) can be categorized into the liquid film between the wall and the bubble, the capillary wave on the bubble surface at the rear of the liquid film, the secondary flow from the wake of the bubble, and bubble shapes between the front and rear side. In the case of the flow conditions, the pressure gradient–induced flow for the horizontal channel represented in Fig. 5.1(a) is called Poiseuille flow, and the wall velocity–induced flow for the ship surface, shown in Fig. 5.1(b), is called Couette flow. In the case of a large-sized bubble in Couette flow, the traveling velocity of the bubble is typically slower than that of the wall velocity.

Thus, the bubble characteristics on the Couette flow are expected to form in opposite directions in Poiseuille flow owing to the direction of the relative velocity from the center of the channel with respect to the wall velocity. However, the direction of flow generation affects the flow condition in the liquid film region, which is enhanced for turbulent flow conditions because the liquid film region in the Couette flow is considered turbulent flow, while it is considered as laminar flow in the Poiseuille flow. In addition, the buoyancy direction for Poiseuille flow is the outer side from the main flow while it is inner side to the main flow for Couette flow. Thus, in the present study, a direct numerical simulation of a turbulent Couette channel flow with a single large-sized bubble of varying bubble size was performed to investigate the bubble characteristics such as bubble deformation.
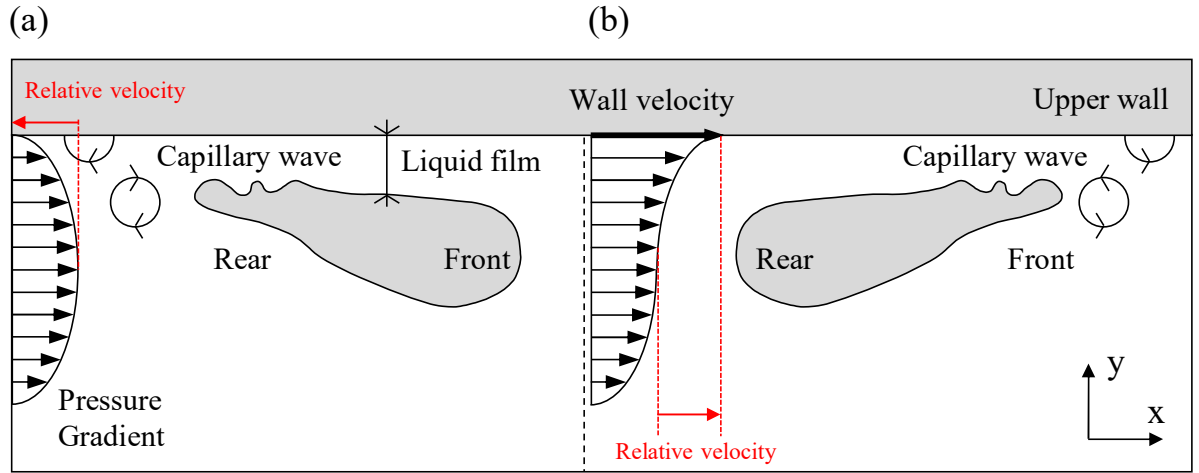
Figure 5.1: Schematic illustration of large-sized bubble formation as the flow condition, (a) turbulent Poiseuille flow, (b) turbulent Couette flow.

5.3 Numerical setup and conditions

The domain of the numerical simulation is modeled according to the experimental channel set-up of Oishi and Murai (2014) and is schematically shown in Fig. 5.2. The test section is 6000 mm in length, and it generated a fully developed boundary layer before injecting the bubble inside the channel; it is 100 mm in width to prevent the effect of from the boundary layer from the sidewall. However, the length and width of the computational domain can be shortened by the periodic condition in the streamwise and spanwise directions, and its contribution to this study was less than that in a study by Kim et al. (2020), and this was in order to save computational resources.

Based on the experimental conditions, the dimensions of the domain were as follows: height (H = 2h) = 10 mm, where h is the half-height of the channel, length (L) = 100 mm, and width (W) = 70 mm. Table 5.1 lists the experimental and numerical conditions of the present work and previous studies (Oishi and Murai, 2014, and Kim et al. 2020) including the size of the channel. The present study generated a turbulent Couette flow in the channel for comparison with the previous studies. The velocity of the upper wall in the channel (U_{wall}) was applied to obtain the same friction velocity (u_τ) used in previous studies to compare the bubble characteristics and drag reduction performance in further studies. All dimensionless numbers were obtained from single-phase flow conditions.

Table 5.1 Comparison of experimental and numerical conditions.

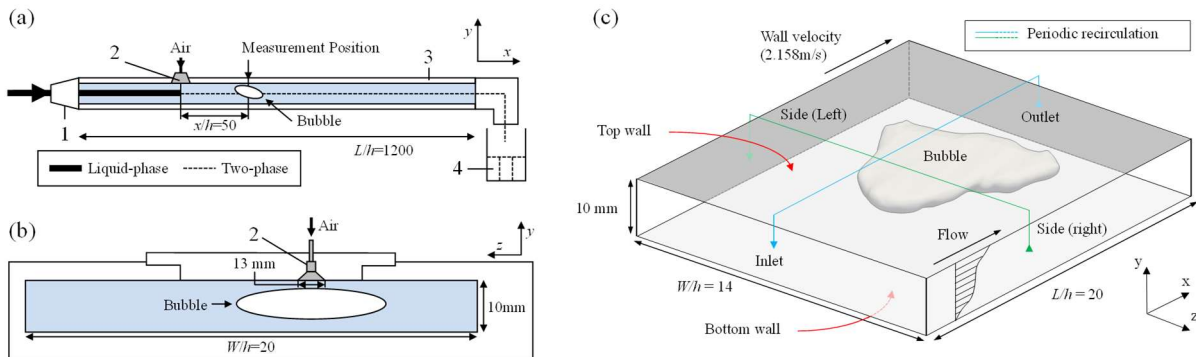|	Oishi and Murai (2014)	Kim et al. (2020)	Present study
Flow condition	Poiseuille flow	Poiseuille flow	Couette flow
$L \times H \times W$ [mm]	$6000 \times 10 \times 100$	$200 \times 10 \times 75$	$100 \times 10 \times 70$
ρ [kg/m^3]	998.7	998.7	998.7
v [m^2/s]	1.08×10^{-6}	1.08×10^{-6}	1.08×10^{-6}
U_{mean} [m/s]	1.0	1.06	1.11
U_{wall} [m/s]	−	−	2.16
Fr	3.19	3.37	3.54
Re	9260	9783	10278
Re_τ	260	260	260

Figure 5.2: Schematic of experimental and numerical conditions (a) Oishi and Murai (2014), (b) present study.

The numerical simulation was performed using the open-source CFD package, OpenFOAM® v1906. The *PimpleFoam* solver was used to generate a fully developed turbulent flow in the channel, whereas the *InterIsoFoam* solver implemented the *IsoAdvector* method, as the interface sharpening method was used for the two-phase flow in the study. Further details, such as the verification work on *InterIsoFoam*, are presented in Kim et al. (2020). All schemes in this study provide second-order accuracy.

The global time step was set to 2.0×10^{-6} s to ensure that the Courant–Friedrichs–Lewy (CFL) number remained below 0.5; the interface CFL number was less than 0.1, in each simulation case, while in the previous study it was maintained at approximately 0.4, because the interface CFL number frequently shot up over the unit owing to the large deformation of the bubble instantaneously. Both the solvers use the *Pimple* algorithm for pressure-velocity coupling in a segregated manner, which computes a velocity field to satisfy the continuity and momentum equations using an iterative procedure.

Table 5.2 lists the boundary conditions of the computational domain. The numerical procedure was divided into three stages owing to the required changes in the solvers and boundary conditions: Stage 1 performed a fully developed turbulent Couette channel flow, Stage 2 conducted bubble injection, and stabilization, and Stage 3 conducted turbulent channel flow with a single injected large-sized bubble. Further details regarding this numerical procedure have been reported by Kim et al. (2020).

5.4 Modeling of turbulent Couette flow

Figure 5.3 shows a schematic view of the turbulent Couette flow generation in stage 1. The flow was driven by a pressure gradient to reach a bulk velocity of 1.11 m/s, as shown in Fig.5.3(a). Under this condition, there is a gap between the pressure gradient region and the wall, to generate the initial perturbation. When the mean velocity is sufficiently high, the flow condition changes from the pressure gradient to the velocity condition of the top wall, as shown in Fig.5.3(b). Finally, a turbulent Couette flow was generated. Figure 5.4 shows the numerical results of turbulent Couette channel flow, which was investigated by examining the profile of the dimensionless mean velocity in the streamwise direction $u^+ = (u - u_{\mathrm{wall}})/u_\tau$ and the root-mean-square (RMS) velocity fluctuations in the streamwise and wall-normal directions, as shown in equation (5.1).

In addition, the dimensionless Reynolds shear stress, $-\overline{u'v'}/u_\tau^2$, which is represented as a

function of the wall distance $y^+ = yu_\tau/v$ and y/h, was examined.

$$u_{rms}^+ = \sqrt{\overline{u'^2}}/u_\tau \; ; \quad v_{rms}^+ = \sqrt{\overline{v'^2}}/u_\tau \tag{5.1}$$

Herein, two previous studies were compared with the present results. One is Oishi and Murai (2014), which has the same domain condition as the present study, to confirm the mean velocity profile and the difference in turbulent properties. The other is by Avsarkisov et al. (2014), who investigated turbulent plane Couette flow in a single-phase flow to determine whether the turbulent properties were obtained well for Couette flow conditions. The mean velocity and RMS velocity fluctuation in the wall-normal direction in the present study show similar trends to those of both these studies. The RMS velocity fluctuation in the streamwise direction shows similar trends to both previous studies below $y^+ = 10$.

Table 5.2 Boundary conditions and solvers used in each stage.

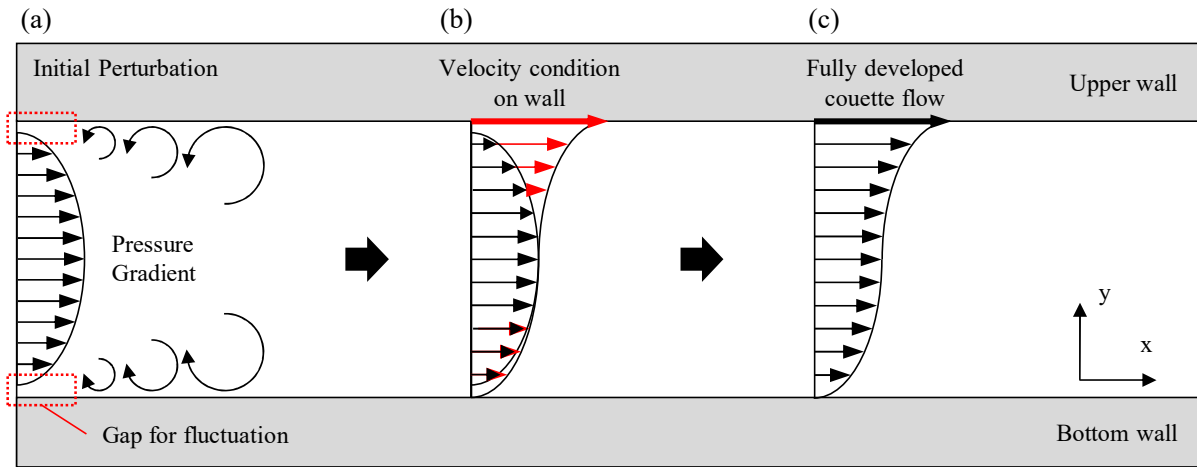| Term	Stage 1	Stage 2	Stage 3
Solver	*pimpleFoam*	*interIsoFoam*, *interFoam*	
Top	*Wall velocity* (2.16m/s)	*Wall velocity* (2.16m/s), *ConstantAlphaContactAngle* (71°)	
Bottom	*NoSlip*	*NoSlip*, *ConstantAlphaContactAngle* (71°)	
Inlet/Outlet	*Cyclic* (Inlet ↔ Outlet)		
Side	*Cyclic* (Left ↔ Right)		

Figure 5.3: Sequence of generation of turbulent couette flow (a) Initial perturbation by pressure gradient, (b) Change the pressure gradient to velocity condition on wall, (c) Fully developed Couette flow.

Meanwhile, the present results of RMS velocity fluctuation show similar trends and are located above the results of Oishi and Murai (2014) from $y^+ = 40$ while located under those of Avsarkisov et al. (2014).

This deviation of the velocity fluctuation in the streamwise and wall-normal directions on the turbulent Couette flow is expected to affect the Reynolds shear stress, and it shows different trends between the two previous studies. The present results approach the turbulent Couette flow, but there is some deviation between them. This deviation indicates that the momentum from the pressure gradient remained and hindered the momentum transfer from the near top wall to the bulk flow and bottom of the channel. Moreover, the current mesh condition is based on the flow conditions of Oishi and Murai (2014) or the channel size with respect to the coherent turbulent structure in turbulent Couette channel flow is not enough to develop, as reported by Kawata and Tsukahara (2021). In a further study, it is necessary to investigate the mesh condition to improve the accuracy of the turbulent properties of turbulent Couette flow.
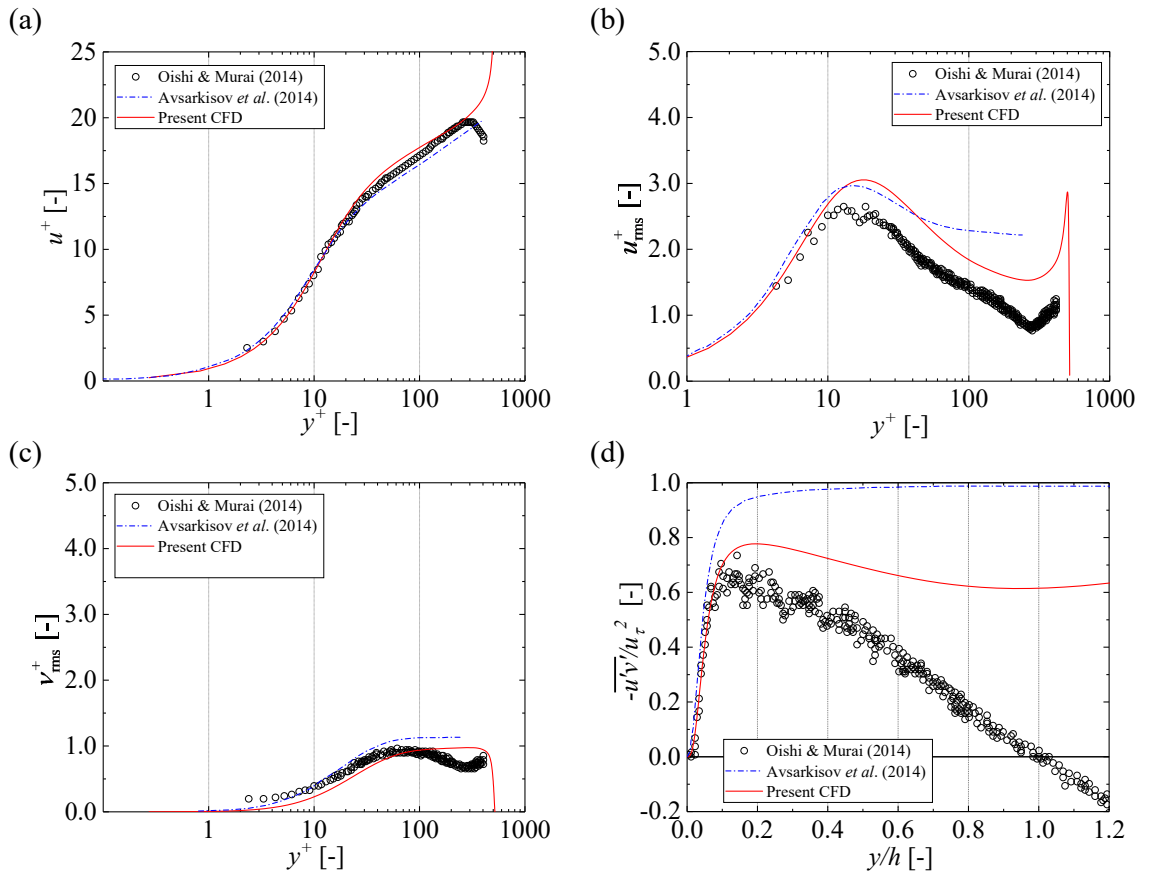

Figure 5.4: Comparison of the turbulent properties as flow condition (a) Mean velocity, (b) RMS velocity fluctuation in streamwise direction, (c) RMS velocity fluctuation in wall-normal direction, and (d) Reynolds shear stress.

5.5 Numerical results of large-sized bubble in turbulent Couette channel flow

5.5.1 Characteristics of the initial bubble

In stage 2, the bubbles were injected by *SetFields*, which sets the scalar values of the fields in specific regions. To stabilize the bubble in the channel, an *adjustable time step* is used in this stage to maintain the interface CFL number below 0.4.

When placing the bubble in the channel, as shown in Fig. 5.5(a), there is a small gap between the wall and bubble interface, which saves computational resources for detaching from the wall. It is placed at the bottom of the channel because it is fragmented into small bubbles by the high shear near the top wall, as shown in the top panel of Fig. 5.5(b). Consequently, its shape was successfully maintained, as shown in Fig. 5.5(c).

Thus, further numerical simulations were performed on the three bubble cases, as shown in Table 5.3 and Fig. 5.6, and these properties were obtained before the initial breakup event. There are two definitions of bubble velocity: the traveling velocity of the bubble, $U_{tra.}$, and the relative velocity, $U_{rel.} = U_{wall} - U_{tra.}$ with respect to the upper-wall velocity. Thus, Weber numbers, $We_{tra.}$ and $We_{rel.}$, were obtained using these two velocities. Here, the Weber numbers in the range of $200 - 300$, wherein the drag reduction in secondary flow and laminarization in the middle of the liquid film at turbulent Poiseuille flow can be observed in Chapter 4.
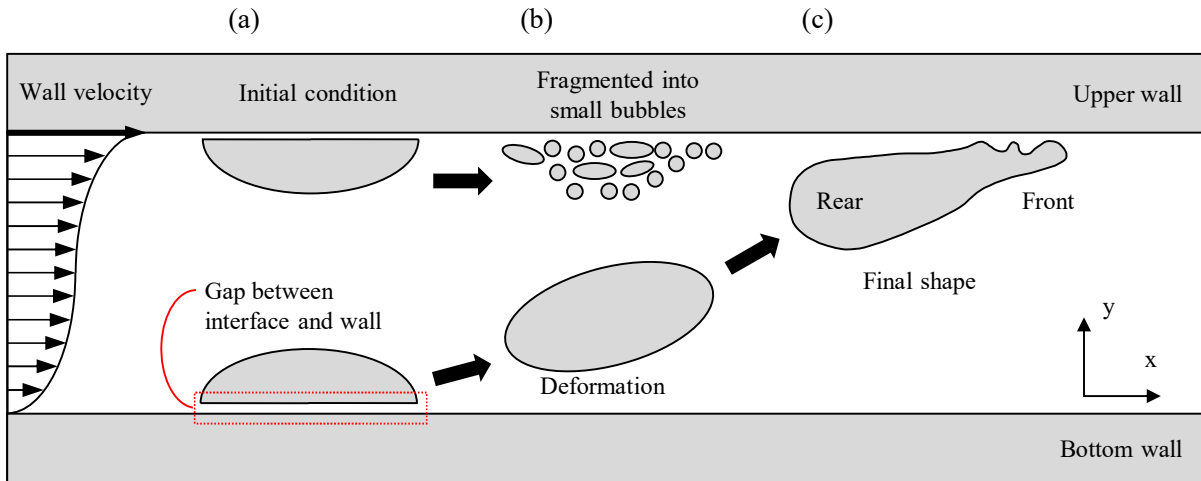

Figure 5.5: Schematic view of bubble injection in the channel (a) Initial condition of bubble when placing near top and bottom, (b) Intermediate condition of bubble deformation as the initial locations, (c) Final shape of bubble when bubble is placed at bottom of channel.

5.5.2 Deformation characteristics of a large-sized bubble

Figures 5.7 – 5.9 show the top views of bubble evolution as the bubble cases in time period. As expected, the capillary wave region is formed on the front side of the bubble, while the rear shape of the individual bubble is round and arch. Although it is difficult to determine the bubble dynamics with respect to the bubble sizes, the bubble deformations can be categorized as follows:

(a) The initial state of the bubble is prior to the deformation, which corresponds to Case 1 (0–167, 351, 410, 621, 671 ms), Case 2(0, 59, 270, 369, 432 ms) and Case 3 (0, 500, 693 ms). The front side of the bubble is irregular, with a high curvature on the tip in the spanwise direction.

(b) After the initial state, the ligaments develop from the span edge of the front side of the bubble. Generally, the ligament head grows at the front and outer sides in a spanwise direction. These ligaments are developed from both sides for Case 1 (261, 288 ms), Case 2 (180, 270), and Case 3 (63, 122, 522 – 612 ms), when the front side of the bubble is aligned perpendicular in the streamwise direction.
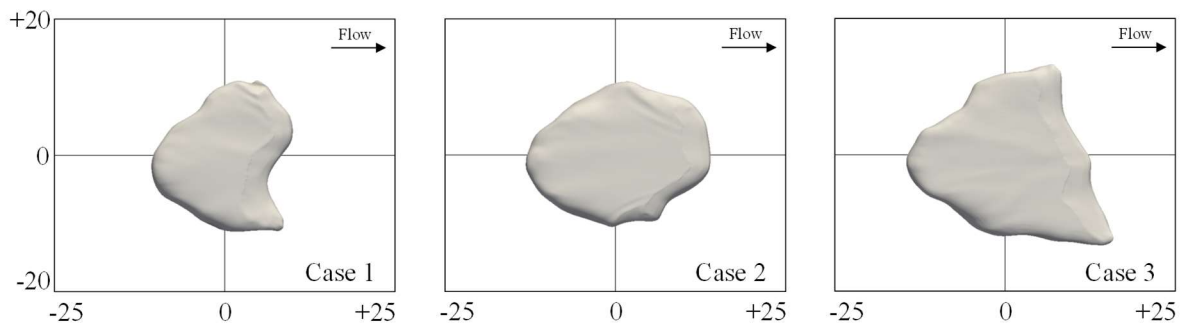
Figure 5.6: Initial bubble shapes from top view.

Table 5.3 Comparison of bubble parameters; The equivalent bubble diameter, d_e, was calculated from the bubble volume, V_b.

		Case1	Case2	Case3
Bubble volume (V_{bubble}) [mm³]		1463.3	1912.2	2167.5
Equivalent diameter ($D_{equiv.}$) [mm]		14.09	15.40	16.06
Bubble velocity	$U_{tra.}$ [m/s]	1.075	1.083	1.112
	$U_{tra.} / U_{mean}$	0.968	0.976	1.002
	$U_{rel.}$ [m/s]	1.085	1.077	1.048
	$U_{rel.} / U_{mean}$	0.977	0.970	0.944
Weber number	$We_{tra.} = \rho U_{tra.}^2 D_{equiv.}/\sigma$	232	258	283
	$We_{rel.} = \rho U_{rel.}^2 D_{equiv.}/\sigma$	237	255	252

These ligaments show an imbalance between them, and a relatively small ligament is frequently suppressed. In contrast, a one-direction development of the ligament is shown in Case 1 (410 – 536 ms) and Case 2 (95 – 203, 396, 486 – 572 ms) when the front side of the bubble is tilted from the streamwise direction.

(c) The ligament tips show pinch-off and break up as in Case 1 (297 – 320, 540, 554 ms), Case 2 (243 ms), and Case 3 (243, 252, 612 – 666 ms). Daughter bubbles were generated and detached from the main bubble. The size of these daughter bubbles is typically small with respect to that of the major bubbles to not affect the volume of the major bubble, as shown in Table 5.4, where the volume ratio of the daughter bubbles is distributed nearly zero. After the break-up event, the ligament bases were splash-back, and the center of the air mass shifted to the center of the bubble again.

(d) Meanwhile, not all of the ligaments experience the splash-back after the breakup. A relatively larger ligament than the opposite one suppresses the development of the opposite one. Eventually, the center of the air mass is shifted to the ligament side such that the main bubble part shrinks and expands the ligament for Case 2 (243 – 338 ms) and Case 3 (252 – 383 ms). This situation occurred without splitting as in Case 2 (486 – 572 ms).

(e) After the breakup from the tip of ligaments or shift the center of air mass to the ligament side, the bubble shape was deformed to stabilize its shape, as in Case 1 (351, 410, 621, 671 ms), Case 2(270, 369, 432 ms), and Case 3 (500, 693 ms). The bubble is rotated from the streamwise direction owing to the direction of the development of a relatively large ligament. From this state, one direction of development of the ligament is observed frequently.

Table 5.4 Volume ratio of daughter bubble, $V_{daughter}$, and major bubble, V_{major}; V_{total} is the total volume of the bubble before the each breakup.

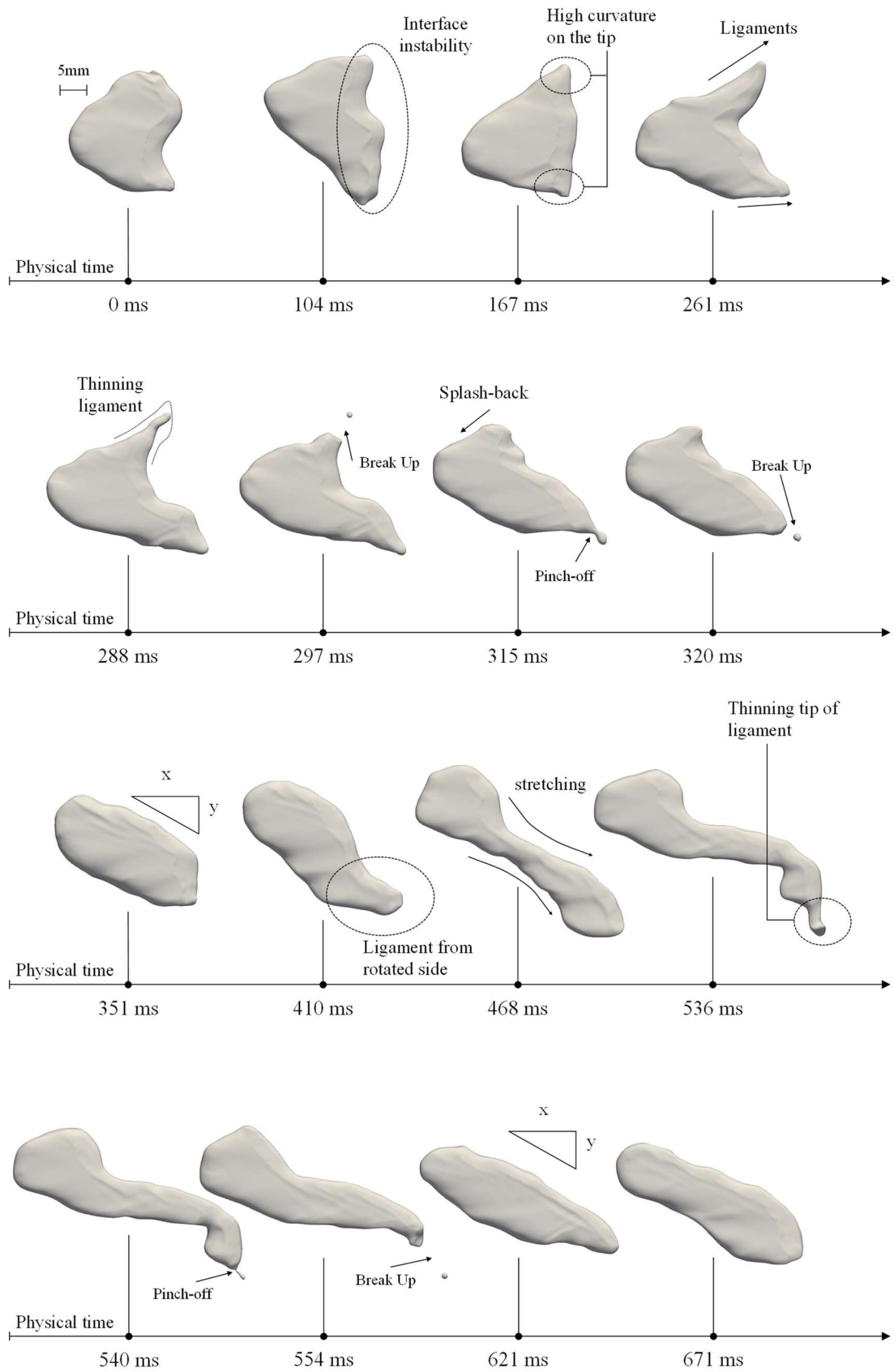| We [-]	Time [ms]	$V_{daughter} / V_{total}$	V_{major} / V_{total}
199	297	0.0004	0.9996
	320	0.0009	0.9991
	554	0.0005	0.9995
226	243	0.0009	0.9991
246	252	0.0091	0.9909
	468	0.0002	0.9998
	648	0.0411	0.9589
	666	0.0539	0.9461

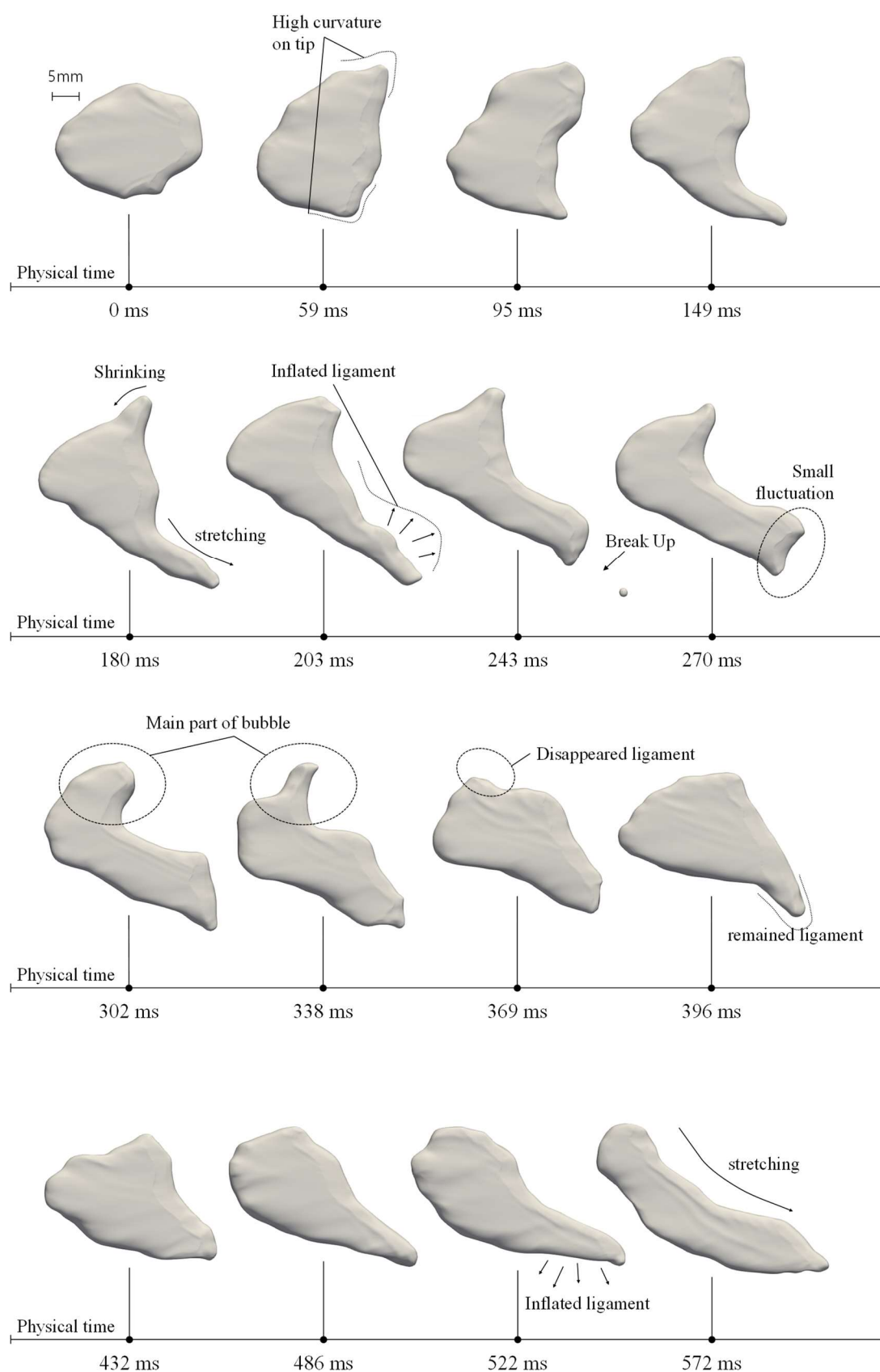Figure. 5.7: Bubble deformation for case 1.
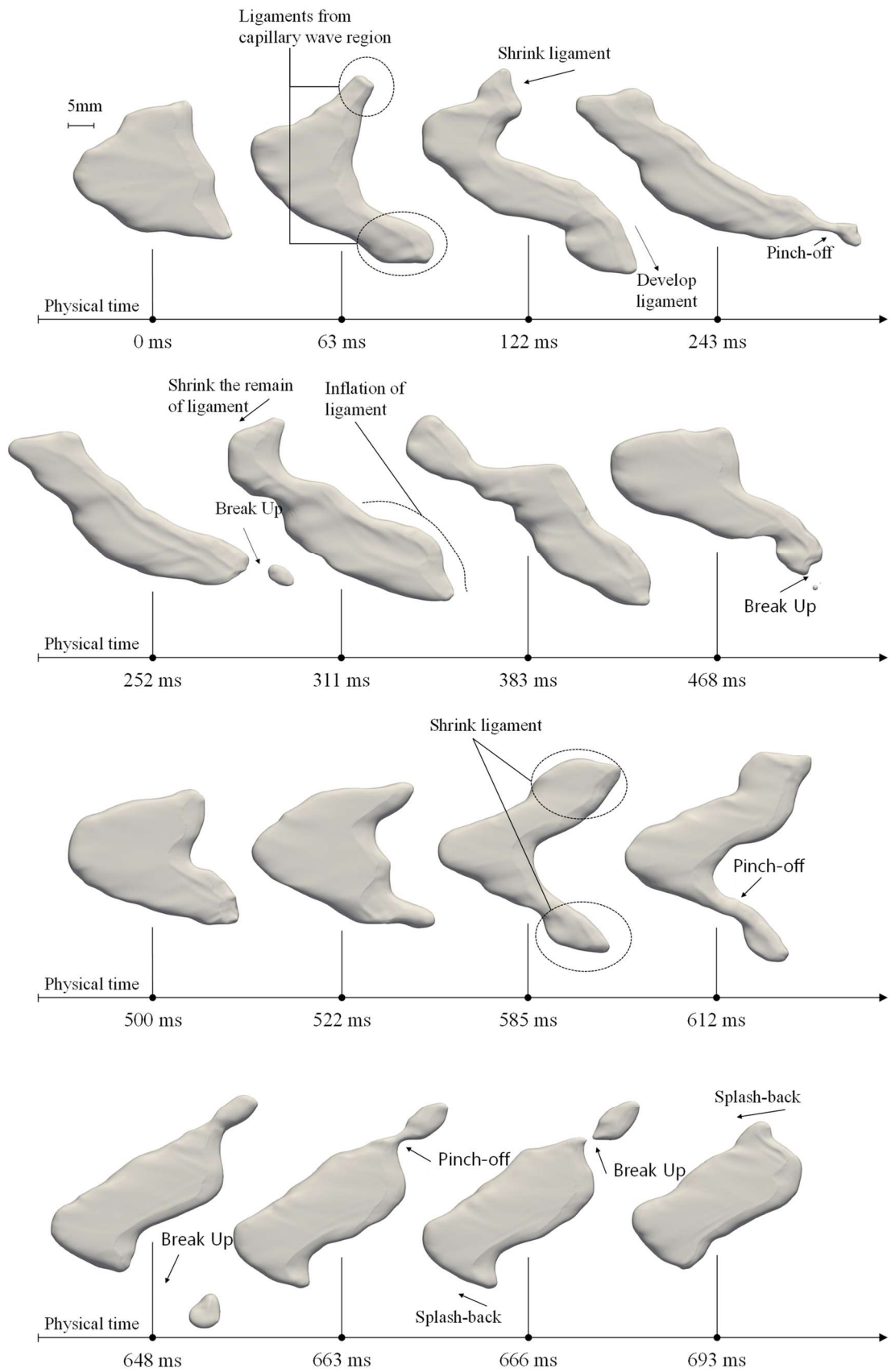
Figure. 5.8: Bubble deformation for case 2.

Figure 5.9: Bubble deformation for case 3.

5.5.2 Relationship between liquid film thickness and velocity ratio

In this study, we categorized several sequences of deformation on large-sized bubbles, and the development of ligament in both direction is confirmed at around Weber number 300 on turbulent Poiseuille flow in Chapter 4. However, one direction ligament and inflation in that direction was not at all, and these deformation is considered to observed from large-sized bubble for current cases in turbulent couette flow. Thus, the velocity field around the bubble is investigated based on the knowledge of bubble deformation in the Couette flow, as shown in Fig. 5.10(a).

The bubble in the laminar Couette flow deformed linearly, thus, the bubble in turbulent Couette flow showed high deformation on the tip of the bubble owing to the exponential change in velocity near the wall. Therefore, the ligament on the tip may be affected by the velocity around the bubble, while the bottom of the bubble is not reached at the bottom of the channel owing to the buoyancy in wall-normal direction. Therefore, the relationship between the velocity and thickness of the liquid film is investigated in this section, as shown in Fig 5.10(b), and the velocity is obtained at $y^+ = 2.5$ of single-phase flow.

Figures 5.11 – 5.13 show the velocity and thickness ratio of the liquid film, respectively. The velocity ratio is obtained by dividing the instantaneous velocity by the mean velocity of the single-phase flow at $y^+ = 2.5$, while the thickness ratio is obtained by dividing h and the half-height of the channel. As can be observed, the region of ligaments where the high-velocity ratio is eventually inflated and stretched for all cases while main parts of the bubble is gradually shrunk. Thus, the inflating and shrinking of each part of the bubbles is strongly associated with the high flow field in the liquid film. In addition, the thickness ratio of these regions is lower than that of other regions.
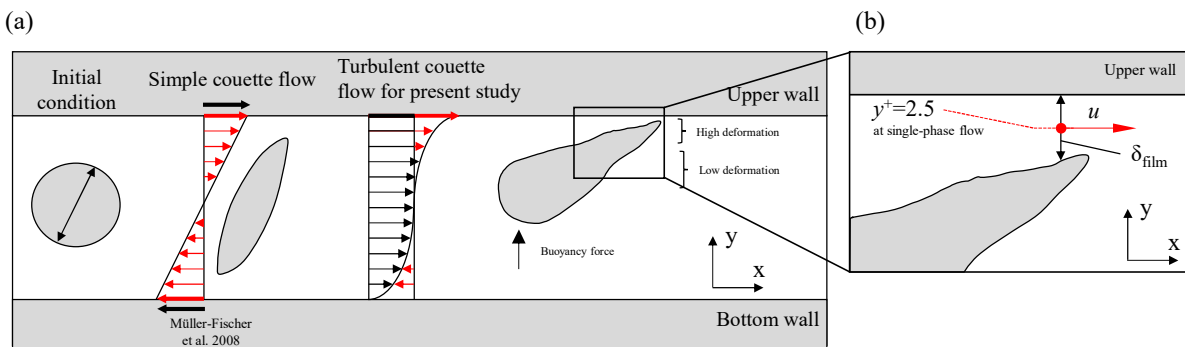

Figure 5.10: (a) Illustration of bubble deformation at laminar and turbulent Couette flow, (b) Schematic view of liquid film thickness and the height where velocity is obtained.
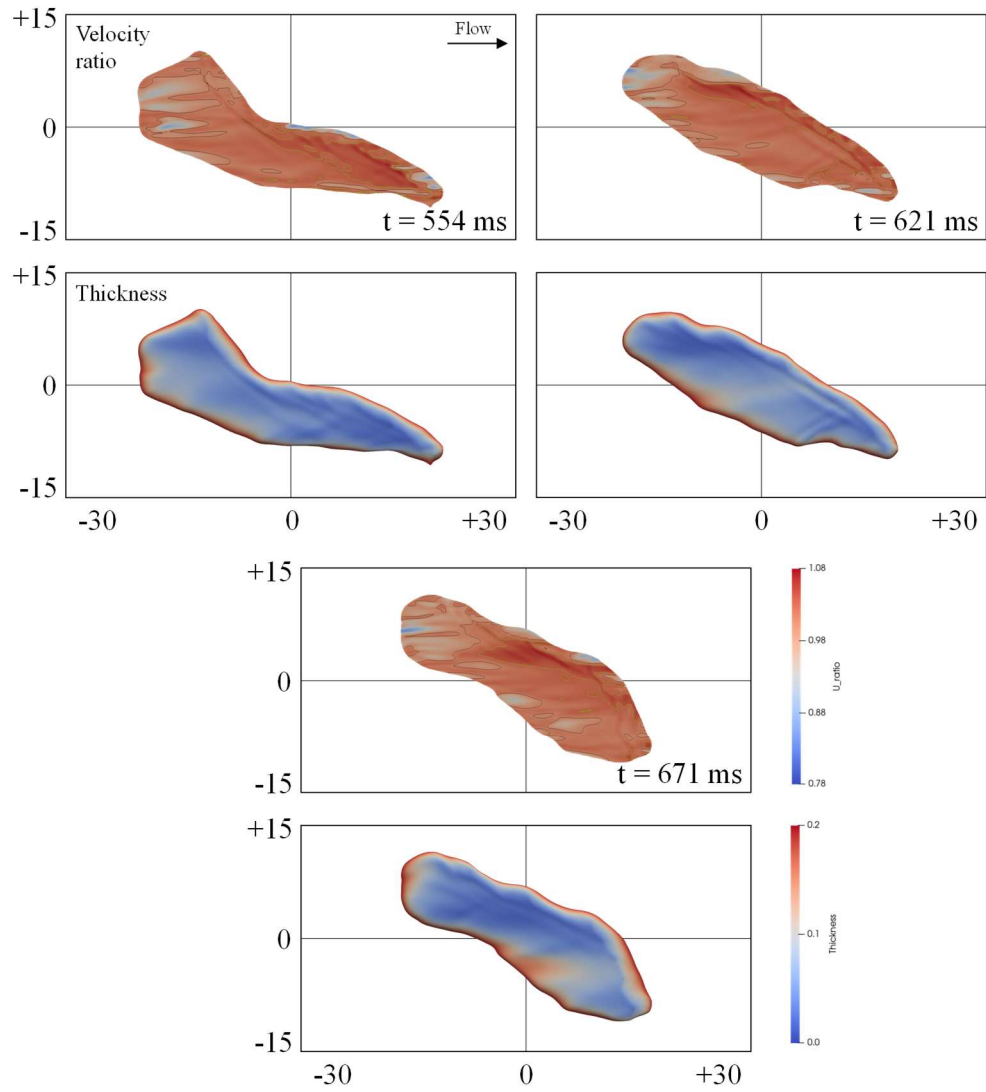
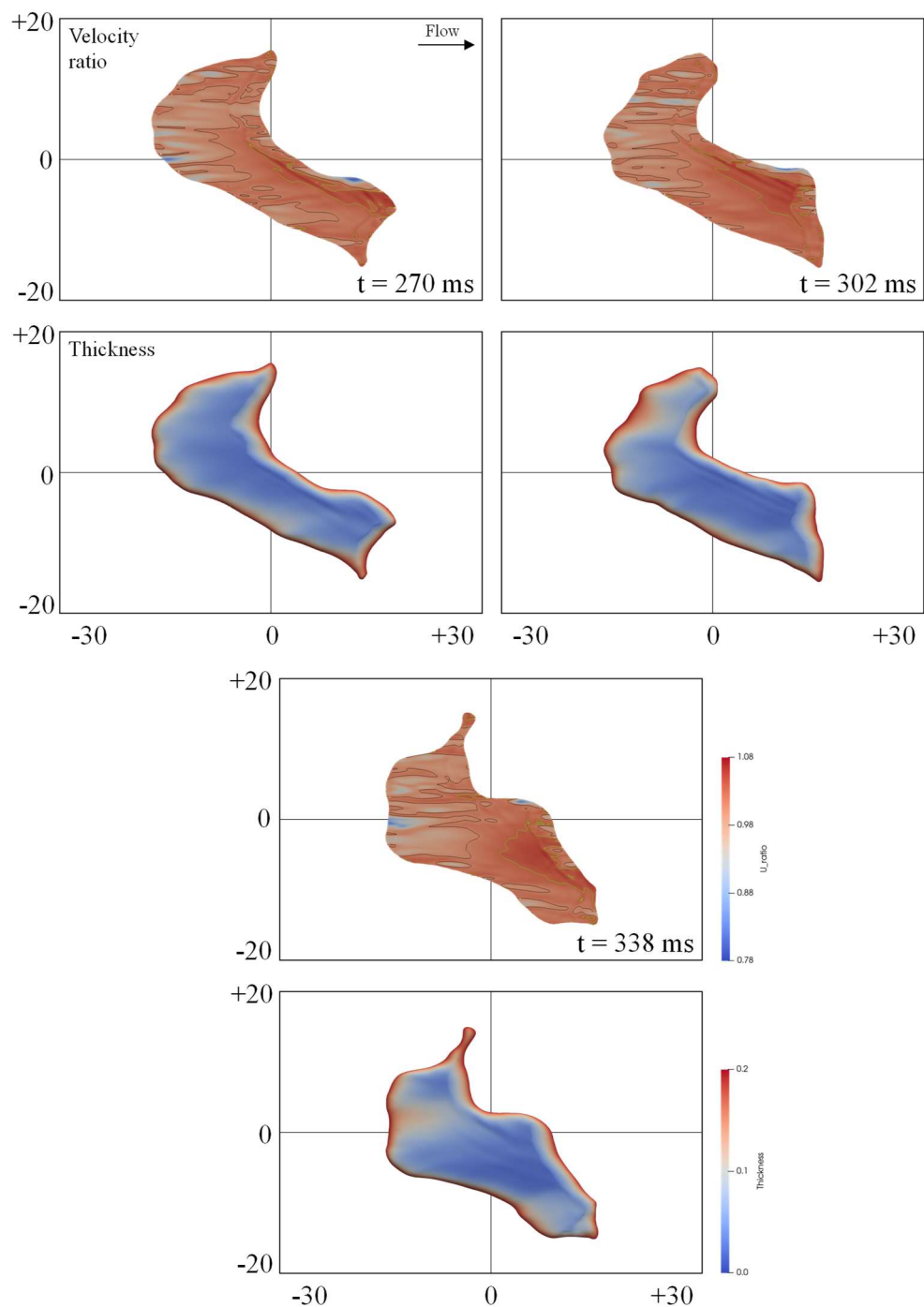Figure. 5.11: Velocity field and thickness of liquid film for case 1.

Figure 5.12: Velocity field and thickness of liquid film for case 2.
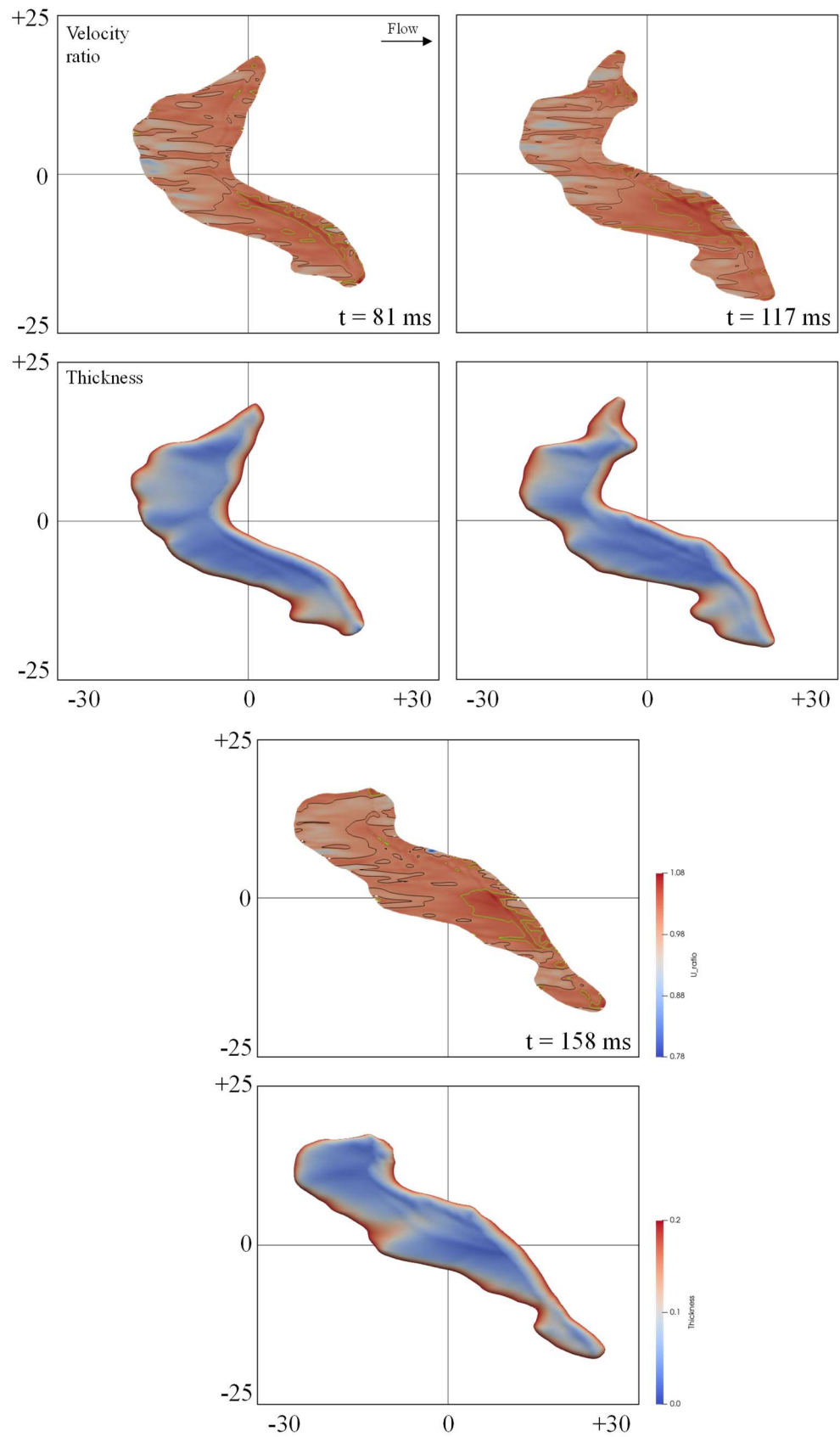
Figure 5.13: Velocity field and thickness of liquid film for case 3.

Figure 5.14 shows the relationship between the velocity ratio and the thickness of the liquid film. The results of these cases are compared with the reference case, which is obtained at a Weber number of 250 from the Poiseuille flow. Typically, the velocity ratio of the Couette flow is distributed widely from 0.8 – 1.05. Meanwhile, there is variation in the time and bubble cases, the data is concentrated, and the velocity ratio is inversely proportional to the specific thickness ratio. In detail, the velocity ratio increased to approximately 1.05 below $\delta_{film}/h = 0.05$. In the reference case the distributions inverse of that in the Couette flow; however, δ_{film}/h is not above 0.05, and shows no concentrated trends near $\delta_{film}/h = 0.05$. Thus, the acceleration of velocity in this region and thinning of the liquid film for Couette flow are considered to cause additional deformation on the tip, similar to the development of the ligament, as shown in Fig 5.15.

Figure 5.14: Scatter plots on the relationship between velocity ratio and thickness of liquid film. (a) Case 1, (b) Case 2, (c) Case 3, (d) Reference case, $We = 250$ in Chapter 4.

Figure 5.15: Velocity acceleration on liquid film and additional deformation of tip on the bubble.

5.6 Conclusion

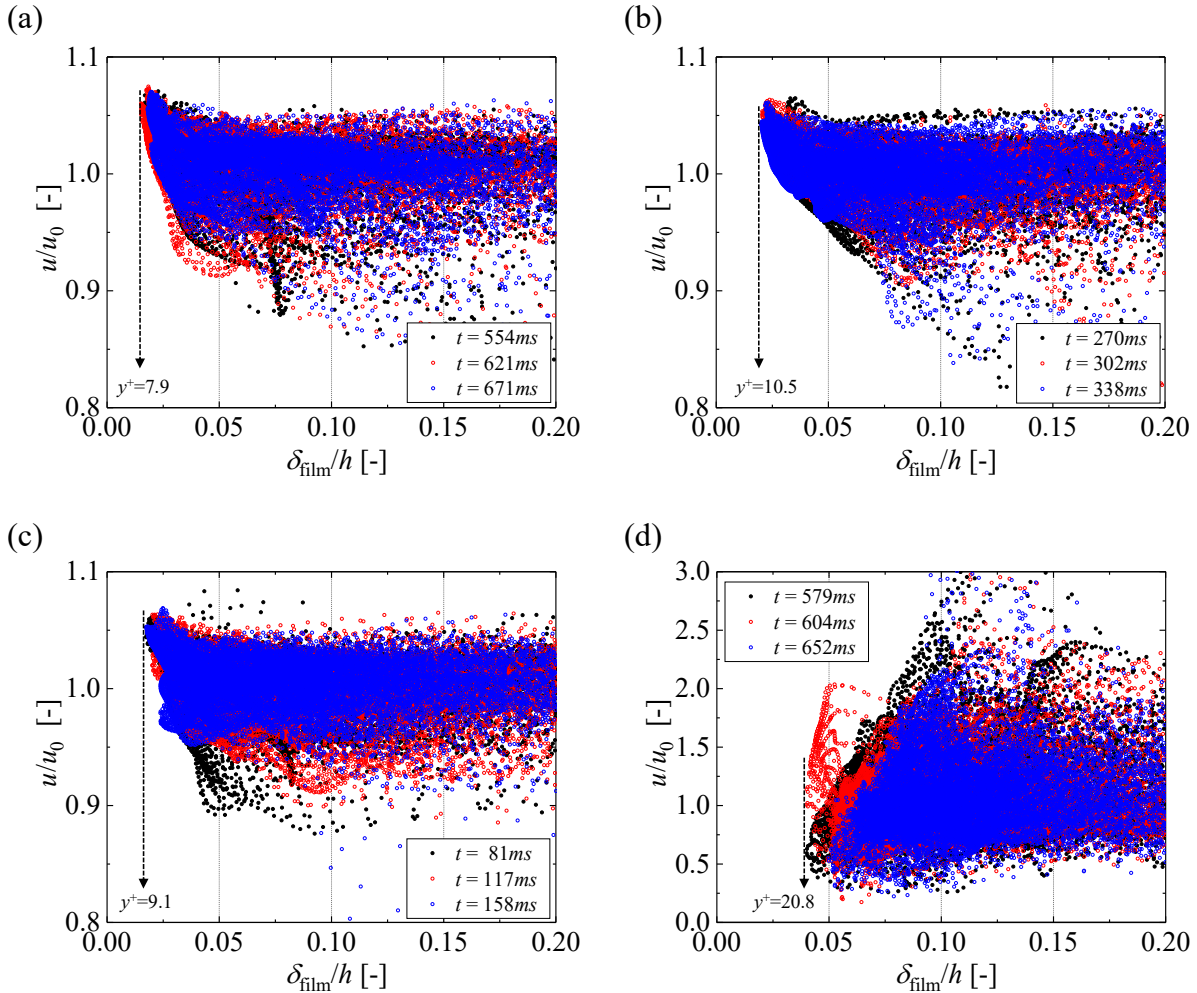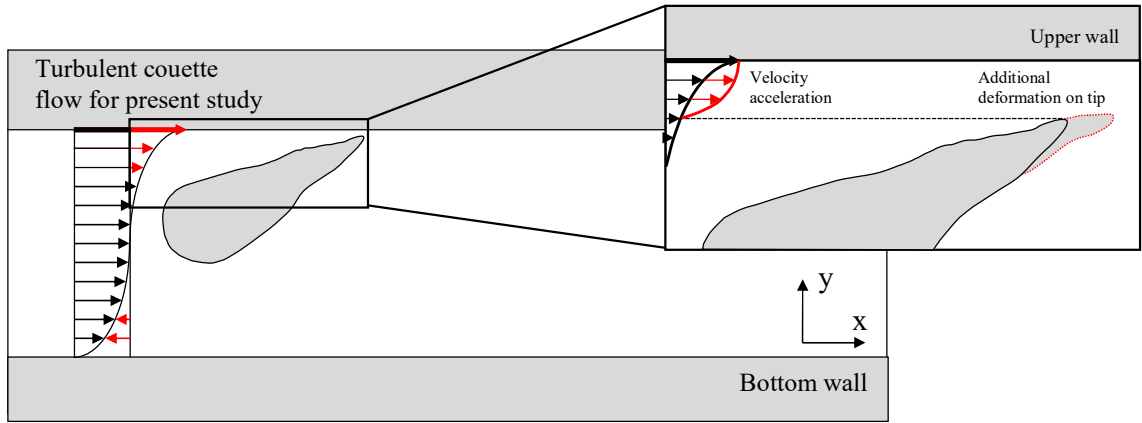In this study, the numerical flow visualization of a single large-sized bubble in a turbulent Couette channel flow was performed. As expected, for a single large-sized bubble in turbulent Couette flow, the representative shape characteristics of the large-sized bubble, such as the liquid film and the capillary wave, were formed in the direction opposite to those at Poiseuille flow. Figure 5.16 shows the physical mechanism of bubble deformation in turbulent Couette channel flow, and the detailed description is as follows.

i) The initial state shows a relatively round shape on the rear side and interface instability on the front side with a high curvature on the tip in the spanwise direction.

ii) Deformation on front side (Ligament) is of two types. One is in both directions when the front side is aligned perpendicularly in the streamwise direction. In addition, a relatively small ligament is suppressed. Another is when the front side is tilted from the streamwise direction, and this condition frequently occurs and is maintained even if the tip breaks.

iii) Change in the bubble CG is observed from the one direction development of ligament. This ligament was sometimes larger than the main part of the bubble and caused shrinking of the main part of the bubble.

iv) Pinch-off and breaking of the ligament occurred when it was sufficiently developed. The tip of the ligament frequently breaks and quickly shrinks owing to the splash-back. Meanwhile, the large ligament due to the change in the bubble CG shows only a small fluctuation on the breakup surface and maintains its shape.

v) Deformation to stable state (Similar with initial stage) is shown after the sequences **iii** and **iv**. Interestingly, in most cases, the front side is tilted in a certain direction because of the

imbalance of ligament size and change in the bubble CG. Consequently, this condition quickly changes to sequence **ii**.

Based on this sequence of bubble deformation, we observed the development of ligament in one direction and inflating ligament with shrinking main part of bubble. This deformation of the bubble is dominated by the displacement of the main part of the bubble, which experiences an acceleration of velocity greater than that of the single-phase flow from the liquid film region. From the scatter plot that shows the relationship between the velocity and thickness ratio, it is clear that the acceleration of velocity occurred below $\delta_{\text{film}}/h = 0.05$.

The bubble cases in this study were limited to a Weber number range of $200 - 300$. Thus, in future work, numerical simulations will be performed on Weber numbers below 200 and above 300 to generalize the mechanism of bubble deformation in turbulent Couette channel flow.
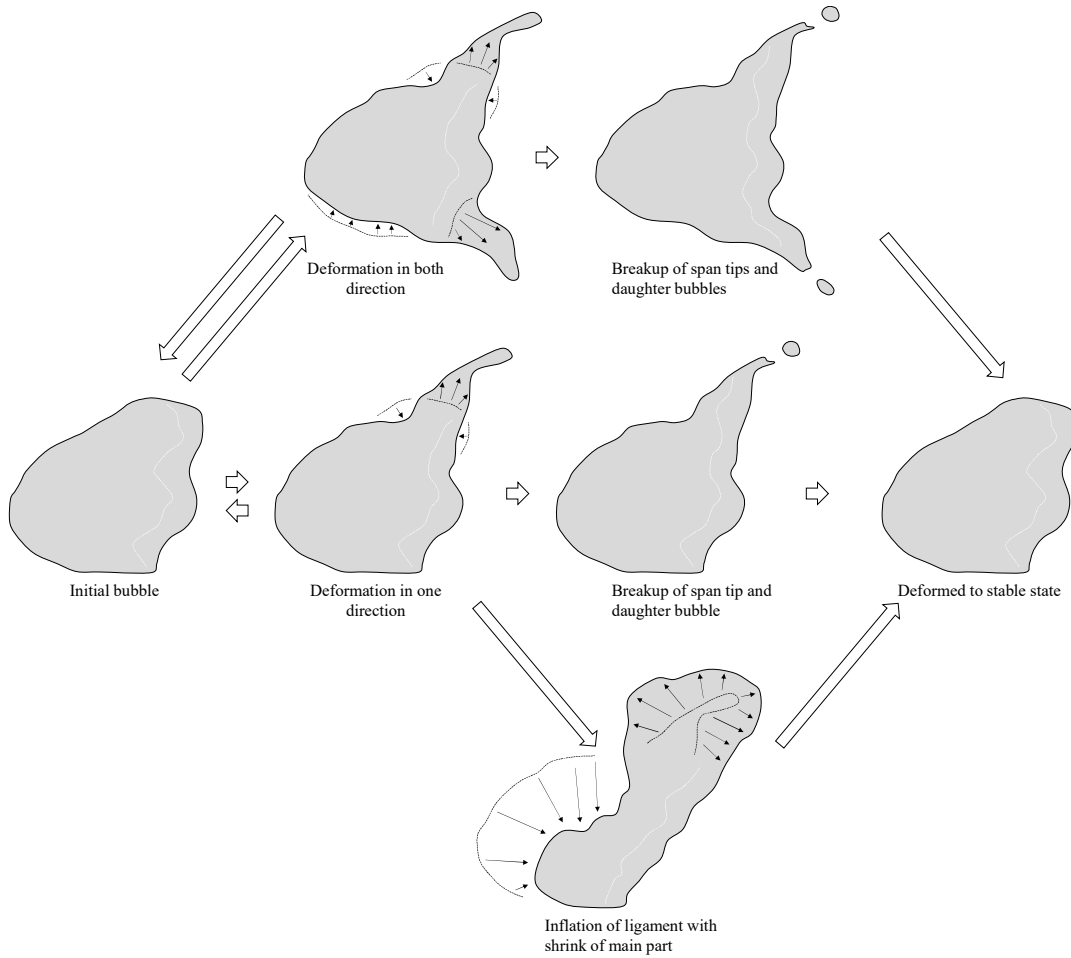

Figure 5.16: Schematic illustration of the sequence of large-sized bubble deformation in turbulent Couette channel flow. The initial bubble states and development of ligaments in both directions are observed from previous chapter.

References

[1] Kim, S.W., Oshima, N., 2021, Numerical Flow Visualization of Large-sized Bubble in Turbulent Couette Channel Flow using OpenFOAM. *Proc. 19th Int. Sym. on Flow Visualization*.

[2] Murai, Y., Fujii, H, Tasaka, Y., and Takeda, Y., 2006. Turbulent bubbly channel flow investigated by ultrasound velocity profiler. *J. Fluid Sci. Technol.* 1(1).

[3] Murai, Y., Fukuda, H., Oishi, Y., Kodama, Y., and Yamamoto, F., 2007. Skin friction reduction by large air bubbles in a horizontal channel flow. *Int. J. Multiphase Flow* 33(2), pp. 147–163.

[4] Oishi. Y., and Murai. Y., 2014. Horizontal turbulent channel flow interacted by a single large bubble. *Exp. Therm. Fluid Sci.* 55, pp. 128–139.

[5] Park, H.J., Tasaka, Y., and Murai, Y., 2019. Bubbly drag reduction investigated by time-resolved ultrasonic pulse echography for liquid films creeping inside a turbulent boundary layer. *Exp. Therm. Fluid Sci.* 103, pp. 66–77.

[6] Murai, Y., 2014. Frictional drag reduction by bubble injection. *Exp. Fluids*.

[7] Kim, S.W., Oshima, N., Murai, Y., and Park, H.J., 2020. Numerical investigation of a single intermediate-sized bubble in horizontal turbulent channel flow. *J. Fluid Sci. Technol.* 15(3).

[8] Avsarkisov, V., Hoyas, S., Oberlack, M., and García-Galache, J.P., 2014. Turbulent plane Couette flow at moderately high Reynolds number. *J. Fluid Mech.* 751.

[9] Kawata, T., and Tsukahara, T., 2021. Scale interactions in turbulent plane Couette flows in minimal domains. *J. Fluid Mech.* 991.

Drag reduction performance produced by large-sized bubbly flows

Contents

Preface

The aim is to establish a numerical model for large-sized bubbly flow as flow conditions, based on the results obtained in **Chapters 4** and **5**. In this chapter, several series of large-sized bubbly flows in turbulent Poiseuille and Couette flows were conducted, and we investigated the drag reduction performances as flow conditions and the expected problems when the numerical model was extended to bubbly flow.

Abstract

In this study, a large-sized bubbly flow was established in turbulent Poiseuille and Couette channel flows to investigate bubble shapes and drag reduction performance under flow conditions. Four different volume fraction cases in both flow conditions were chosen for the comparison of the drag reduction performance. The turbulent Couette channel flow shows reasonable numerical results and a similar trend. In contrast, the turbulent Poiseuille channel flow shows significant problems such as the oscillation of the pressure gradient in the inlet and outlet regions as the bubble exists. As a result, the mean velocity of the channel gradually decreases, and the skin friction changes as the volume fraction increases. The expected solution to this problem is a local bubble swarm in the longer channel to recover the fluctuation of the pressure gradient when the bubble passes.

6.1 Introduction

Frictional drag reduction by air injection has been researched for over 40 years and applied to liquid transport in pipelines and ship surfaces in water. This method does not damage the environment compared to other techniques and does not require appendages or modifications on the wall surface. In industrial fields, it is called air lubrication technology, and there are two aspects of drag reduction: air bubbles and film methods.

The typical bubble in the air bubble methods involves microbubbles. Since the first report by McCormick and Bhattacharyya (1973), many researchers have conducted experiments on micro-bubble drag reduction to study the parameter dependency and skin friction reduction process (Madavan et al. (1985); Merkle and Deustch (1992); Kato et al. (1999); Kodama et al. (2000); Gabillet et al. (2002)). Meanwhile, Moriguchi and Kato (2002), Kawamura et al. (2003), and Shen et al. (2006) reported that the bubble size dependency on micro-bubbles drag reduction is no significant effect in the case of the high shear rate. This implies that a bubble size is not required to be very small. Recently, the discussion on drag reduction mechanism of the bubble was shifted to its deformability, by Moriguchi and Kato (2002), Kitagawa et al. (2005), Lu et al. (2005), Sugiyama et al. (2005), Kawamura (2005).

In contrast, the air film method has been found to be practically viable in the last two decades (Fukuda et al., 1999; Matsumura et al, 2002; Katsui et al, 2003). The air film is formed by injecting air on the super-hydrophobic surface and separates the liquid phase of the flows and the wall by locating between them and interrupting the momentum transfer from the flows to the wall (Fukuda et al., 2000). Although both methods show significant drag reduction from the experimental scale, there is a problem with the persistence of drag reduction from the downstream. For instance, the typical microbubble method contains a-few-millimeter size bubbles, and they frequently coalesce in the shear layer and become large bubbles in the downstream region. However, in the case of the air film method, disturbances on the interface of the air film owing to Kelvin-Helmholtz instability leads to the formation of gas pockets at downstream. The liquid flow is turned upstream as a re-entrant jet, such that the air pockets change to an air ligament. This air ligament is stretched and part of it is separated into large-sized bubbles from the downstream (Mäkiharju et al., 2013).

Therefore, the bubble size at downstream of both methods is important in determining the total drag reduction, when considering the persistency of drag reduction along the streamwise direction. However, the critical bubble size has not been determined. In this situation, the drag

reduction performance of large-sized bubbles was found to be dependent on the bubble length (Murai et al., 2007). Oishi and Murai (2014) rigorously investigated and described influential characteristics such as the velocity gradient and u'v' contours related to the drag reduction of a single large-sized bubble. Park et al. (2019) experimentally investigated the film thickness of large-sized bubbles and BDR. Recently, Kim et al. (2020) numerically realized a single large-sized bubble and investigated the flow field around a large-sized bubble.

In the present study, a direct numerical simulation of large-sized bubbly flow under two flow conditions, turbulent Poiseuille and Couette channel flow, was performed to investigate the drag reduction performance and the difference from the liquid film region of a large-sized bubble, which has a high shear rate in turbulent Couette flow, but a low shear rate in turbulent Poiseuille flow. This is because the physical mechanism of the large-sized bubble is due to its deformation induced by shear stress around the bubble and its buoyancy.

6.2 Numerical setup and conditions

The numerical domain was modeled according to the experimental channel set-up of Oishi and Murai (2014). The length and width of the computational domain can be shortened by the periodic conditions in the streamwise and spanwise directions to save computational resources. Based on the experimental conditions, the domain dimensions were as follows: height ($H = 2h$) = 10 mm, where h is the half-height of the channel, length (L) = 100 mm, and width (W) = 70 mm. Table 6.1 lists the experimental and numerical conditions of the present study, including the size of the channel.

The present study generated a turbulent Couette flow in the channel to compare the experimental results. The velocity of the upper wall in the channel (U_{wall}) for the Couette flow and the mean velocity (U_{mean}) driven by the averaged pressure gradient were applied to obtain the same friction velocity (u_τ) of the experimental study to compare the drag reduction performances as the flow conditions. All dimensionless numbers were obtained from single-phase flow conditions.

Table 6.1 Comparison of experimental and numerical conditions.

Flow condition	Oishi and Murai (2014)	Poiseuille flow	Couette flow
$L \times H \times W$ [mm]	$6000 \times 10 \times 100$	$100 \times 10 \times 70$	
ρ [kg/m^3]	998.7	998.7	
v [m^2/s]	1.08×10^{-6}	1.08×10^{-6}	
U_{mean} [m/s]	1.0	1.039	1.11
U_{wall} [m/s]	–	–	2.16
Fr	3.19	3.31	3.54
Re	9260	9620	10278
Re_τ		260	
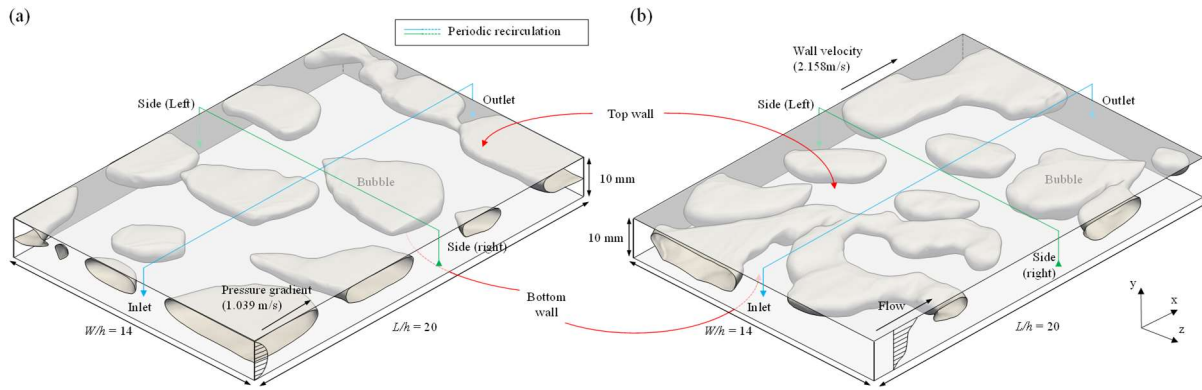
Figure 6.1: Schematic of the numerical conditions (a) Poisuelle flow, (b) Couette flow.

Numerical simulation was performed using the open-source CFD package OpenFOAM® v2006. The *PimpleFoam* solver was used to generate a fully developed turbulent flow for both flow conditions, whereas the *InterIsoFoam* solver implemented the *IsoAdvector* method, as the interface sharpening method was used for two-phase flow in this study. Further details, such as the verification work on *InterIsoFoam*, are presented in Kim et al. (2020). All schemes in this study provide second-order accuracy.

The global time step was set to 2.0×10^{-6} s to ensure that the Courant–Friedrichs–Lewy (CFL) number remained below 0.5; the interface CFL number was less than 0.3, in each simulation case, because the interface CFL number frequently shot up above the unit owing to the breakup and coalescence of the bubble. Further, both solvers use the *Pimple* algorithm for pressure-velocity coupling in a segregated manner, which computes a velocity field to satisfy the continuity and momentum equations using an iterative procedure.

6.3 Numerical results

6.3.1 Mean velocity of large-sized bubbly flow

The simulation cases are divided into two groups as flow conditions, as described in Table 6.2, and these groups comprise four cases as the volume fraction of air, α_{air}. Figure 6.2 and Table 6.3 show the mean velocity of the bubbly flow as a flow condition. In the case of Poiseuille flow, the mean velocity gradually decreased as α_{air} increased, and the difference reached 12.8 % at P24. In contrast, the velocity of the Couette flow is a constant, showing a small fluctuation in the velocity profiles near the top wall. From this perspective, the Poiseuille flow condition is considered similar to the Couette flow condition; however, the velocity profile of the Poiseuille flow at the bottom side of the channel decreased.

Table 6.2 simulation cases for large-sized bubbly flows.

	Case	α_{air}		Case	α_{air}
Poiseuille flow	P9	0.0949 (9.49 %)	Couette flow	C9	0.0957 (9.57 %)
	P14	0.1423 (14.23 %)		C14	0.1436 (14.36 %)
	P19	0.1906 (19.06 %)		C19	0.1908 (19.08 %)
	P24	0.2414 (24.14 %)		C24	0.2469 (24.69 %)

Table 6.3 Mean velocity of large-sized bubbly flows.

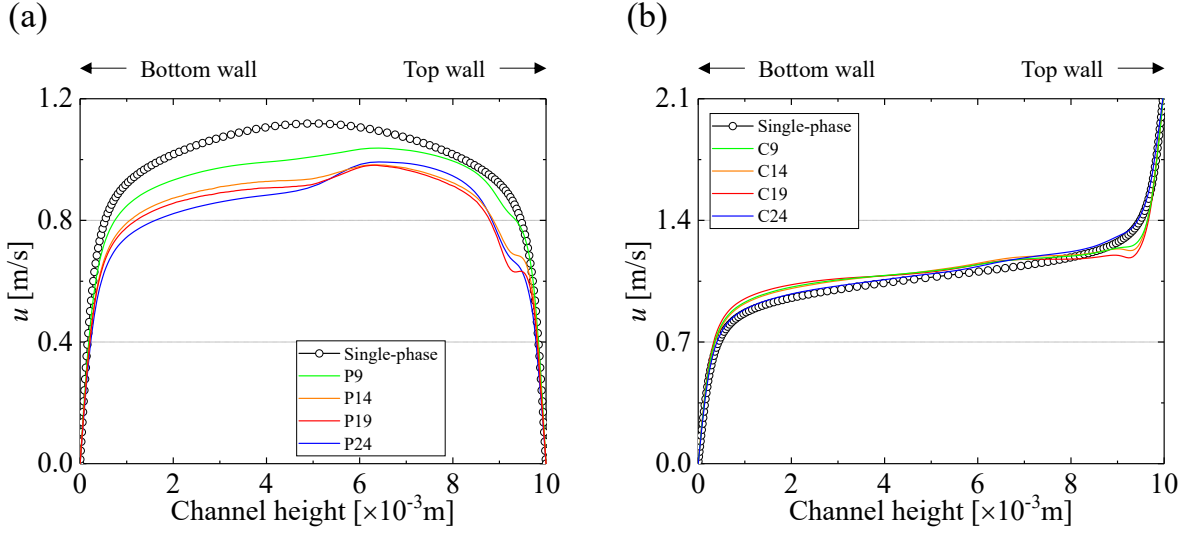| Case	Mean velocity [m/s]	Case	Mean velocity [m/s]
Single-phase	1.006	Single-phase	1.100
P9	0.968	C9	1.104
P14	0.900	C14	1.103
P19	0.883	C19	1.101
P24	0.877	C24	1.102

Figure 6.2: Mean velocity profile of bubbly flow as flow conditions (a) Poisueille flow, (b) Couette flow.

6.3.2 Void fractions and skin friction coefficient of large-sized bubbly flow

Figure 6.3 shows the relationship between the volume fractions and projected void fractions as flow conditions. There was no significant difference in the flow conditions, and the projected void fractions were approximately twice the volume fractions. Figure 6.4 shows the relationship between the volume fractions and mean skin friction coefficients as flow conditions. The Poiseuille flow differs from the mean velocity as the volume fraction increases, and the skin friction is converted to a coefficient based on equation (6.1).

$$C_f = \frac{\tau_w}{\frac{1}{2} \cdot \rho_{liquid} \cdot U_{mean}} \tag{6.1}$$

where τ_w and ρ_{liquid} are the skin friction and density of the liquid phase, respectively, and U_{mean} is the mean velocity of each case.

Subsequently, the temporal average is applied as the time period, and the flows acquired skin frictions are fully developed and achieve a steady state after the bubble injection in the channel. The range of each time period is a quarter of the total physical time, T = 0.1 s in this study. Consequently, the Couette flow shows similar trends with each period and gradually decreases skin friction as time passed. In contrast, the Poiseuille flow shows large deviations as the time period and increases from T3 and T4.
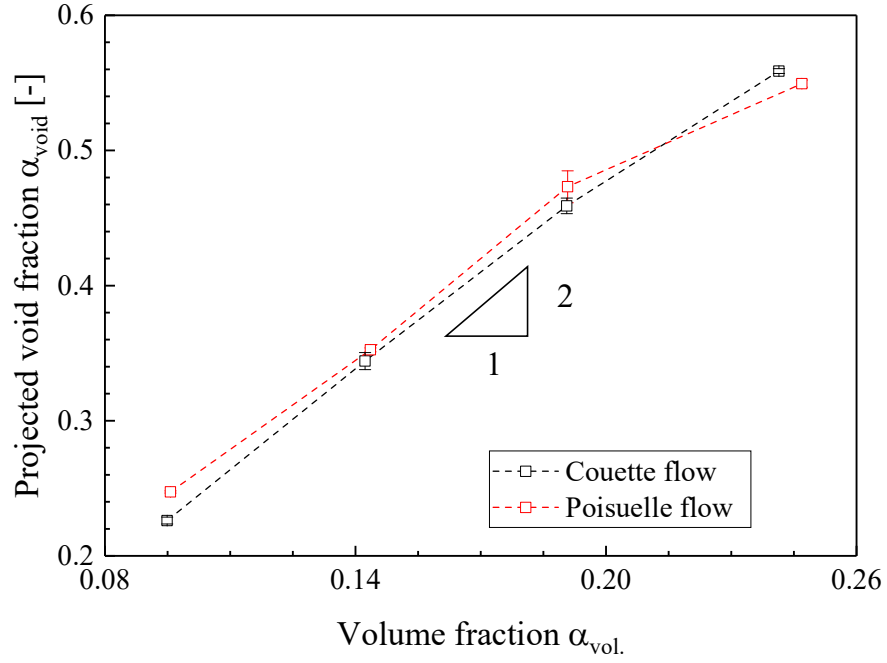
Figure 6.3: Relationship between volume fraction and Projected void fractions.
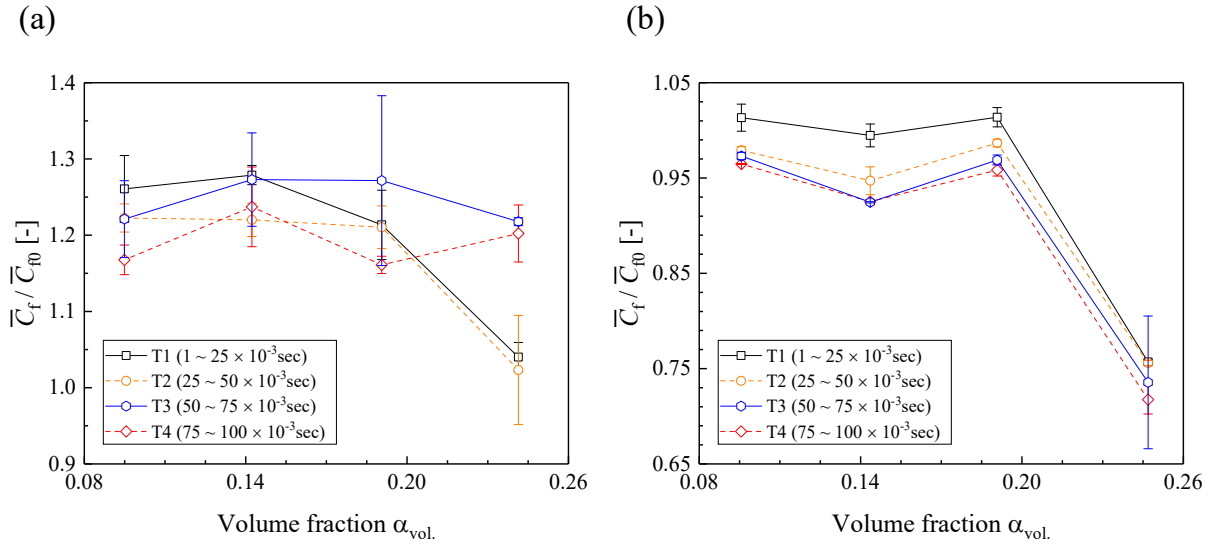
(a)　　　　　　　　　　　　　　　　(b)

Figure 6.4: Mean skin friction coefficients as time period: (a) Poisueille flow, (b) Couette flow.

6.3.3 Instantaneous bubble shape and contour of skin friction coefficients

Figures 6.5 and 6.6 show the instantaneous snapshot of bubble shapes and the contours of the skin friction coefficient for Poiseuille flow. As can be observed, the bubbles coalesce and merge with each other and become larger as the volume fraction increases, and the flow state of P24 almost resembles churn flow. From the contour of the skin friction coefficient, the relaminarization of a liquid film can be observed on sufficiently large bubbles. However, the high skin friction and fluctuations from the inlet and outlet regions from P14 and P24.

The reason is the pressure gradient condition in the inlet, which is designed to separate the pressure fluctuation due to the different phase properties for a single bubble, as described in Chapters 3 and 4. When multiple bubbles pass this region continuously, the internal velocity of the bubble, which shows relatively high velocity and swirling, causes the pressure gradient to fluctuate and the mean velocity decreases. This pressure gradient recovered to a target velocity of 1 m/s when the bubble disappeared in the inlet and outlet regions, as shown in P14 and P24.

There are solutions to this problem. One is adding the source term of the constant pressure gradient in the momentum equation. However, the idea of a constant pressure gradient in the entire region also affects the internal field of the bubble, which can cause unexpected deformation of the bubble. Furthermore, the source term should be adjusted for the target velocity using an iterative procedure. Thus, the current numerical model of large-sized bubbly flow for Poiseuille flow should be modified by locally multiple bubble conditions with longer channel lengths, such as the bubble swarm of repetitive bubble injection (RBI) proposed by Park et al. (2015), which is expected to recover the pressure gradient after the bubbles pass.

Figures 6.7 and 6.8 show the instantaneous snapshot of bubble shapes and the contours of skin friction coefficient for Couette flow. As can be observed, the bubbles in the Couette flow also coalesce and merge with each other and become larger as the volume fraction increases, and the flow state of P24 almost resembles churn flow. From the contour of the skin friction coefficient, the relaminarization of the liquid film can be observed on sufficiently large bubbles. In addition, the Couette flow shows no fluctuation in the contours of the skin friction coefficients at the inlet and outlet regions because the wall velocity is independent of the bubble existence.
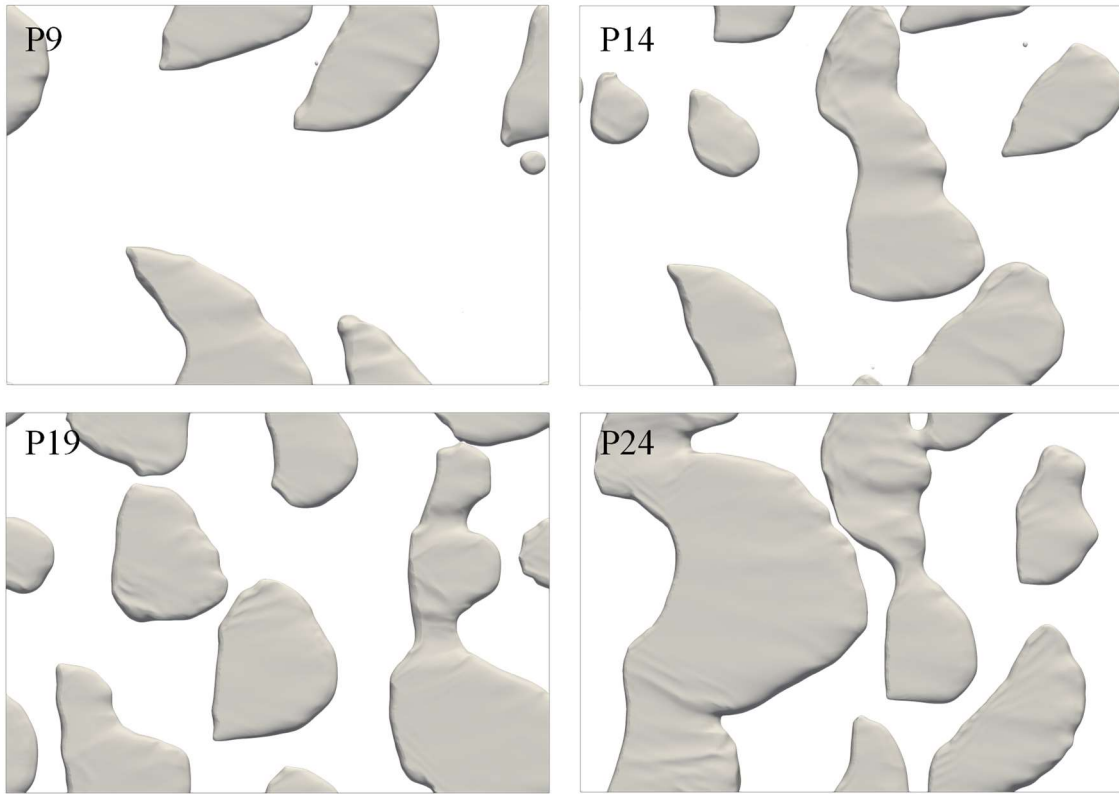
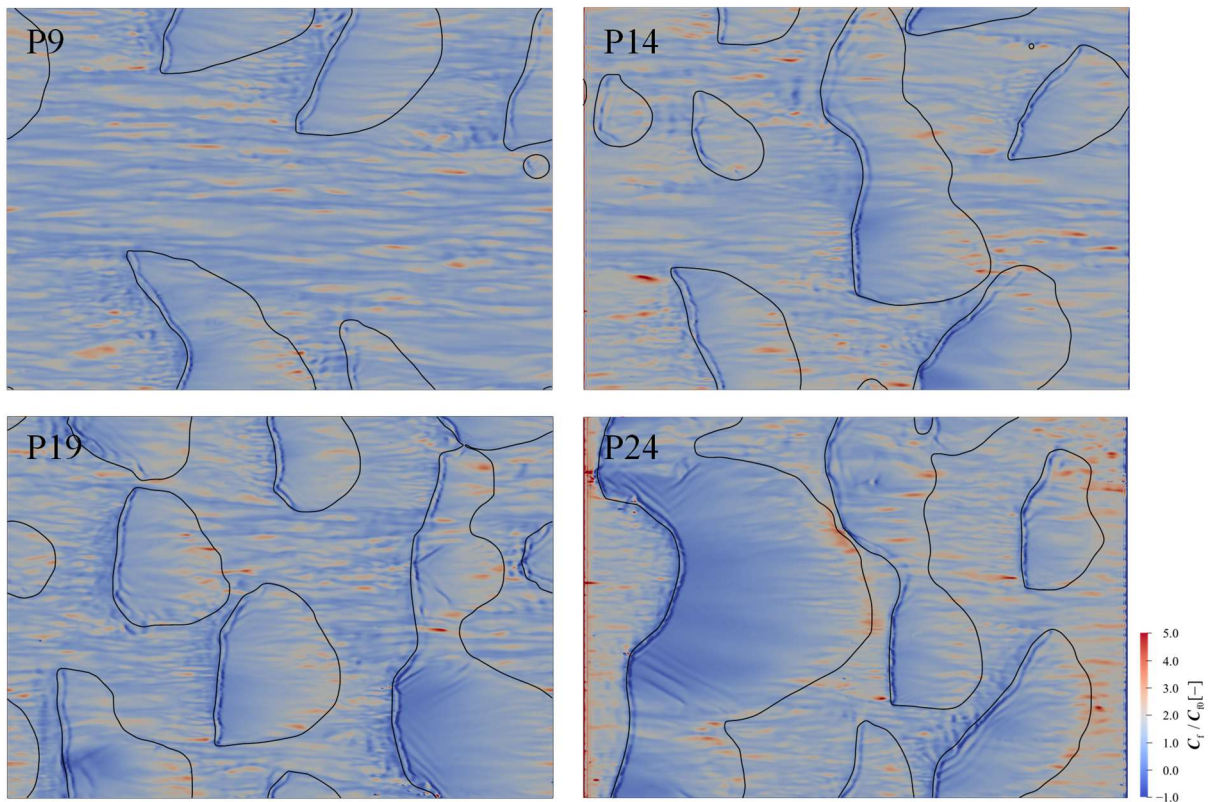Figure 6.5: Instantaneous snapshot on bubble shapes for Poisueille flow

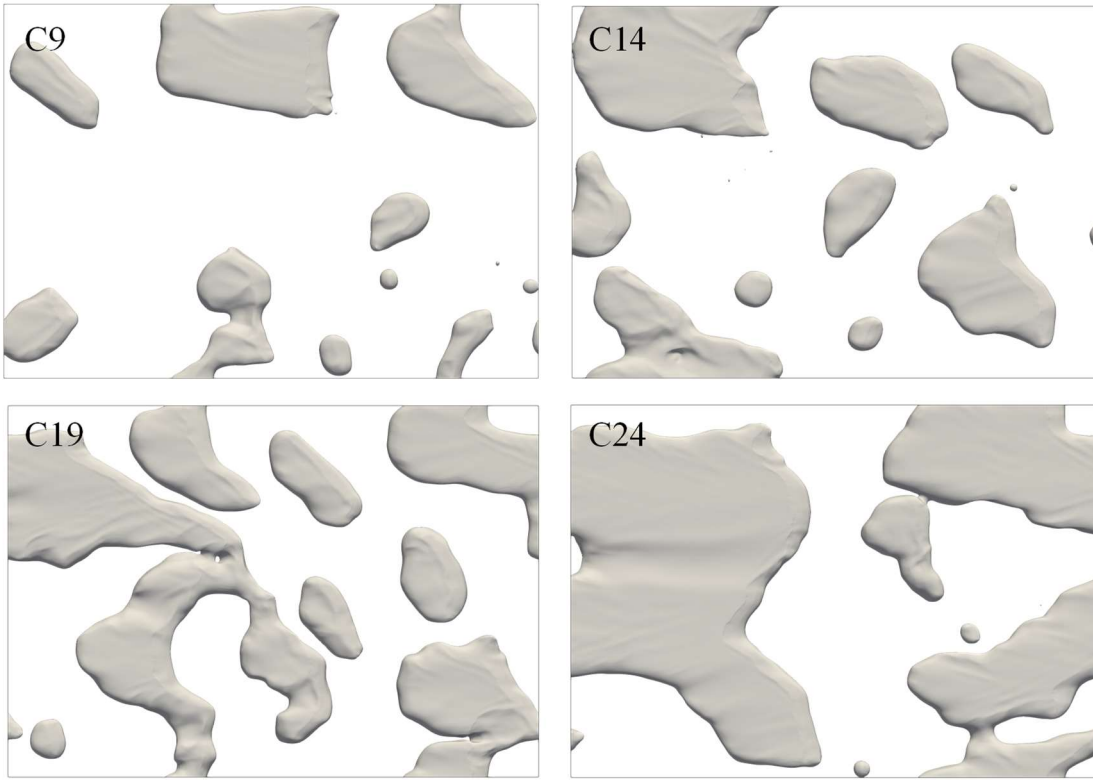Figure 6.6: Instantaneous snapshot on contours of skin friction coefficients for Poisueille flow

Figure 6.7: Instantaneous snapshot on bubble shapes for Couette flow
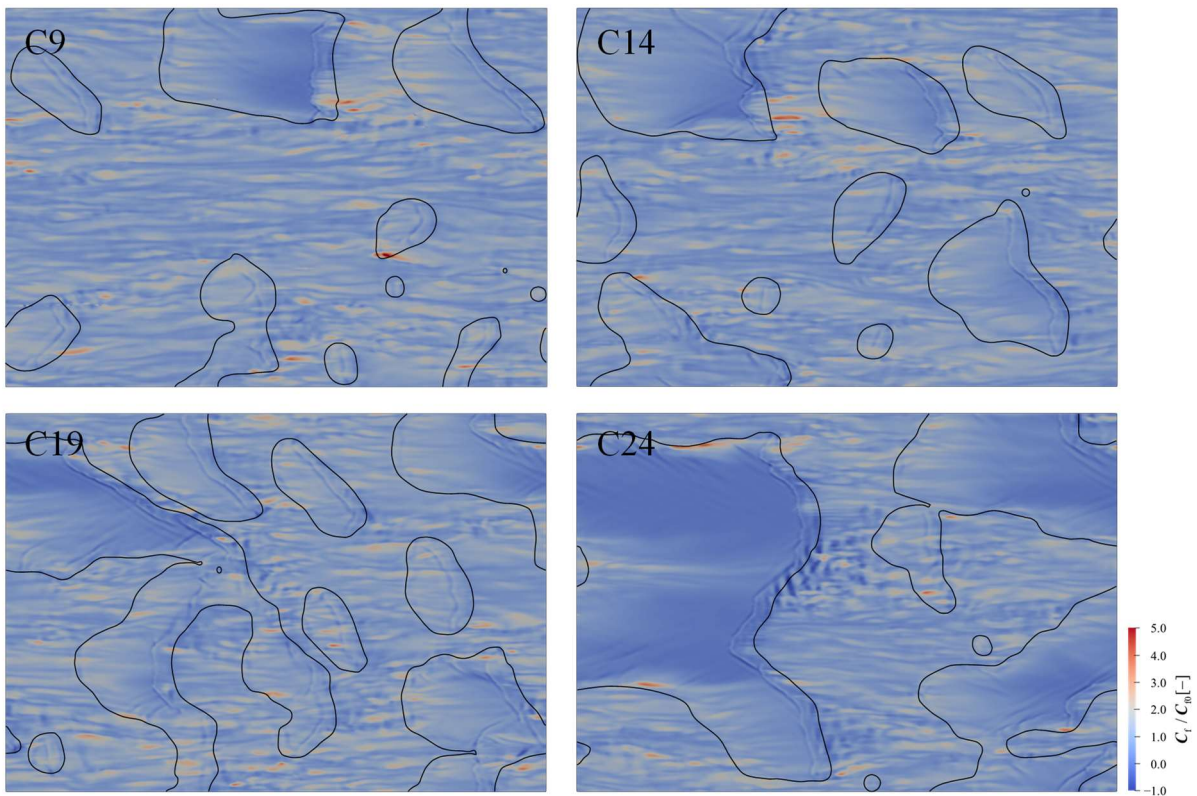
Figure 6.8: Instantaneous snapshot on contours of skin friction coefficients for Couette flow

6.4 Conclusion

In this study, a direct numerical simulation of the large-sized bubbly flow in turbulent Poiseuille and Couette channel flows was performed. The turbulent Couette flow shows reasonable numerical results, and it may show a trend similar to that of the experiment when conducting simulations for longer periods. In contrast, the turbulent Poiseuille flow shows significant problems such as the oscillation of the pressure gradient in the inlet and outlet regions as the bubble exists, and there are the expected solution to this problem is a local bubble swarm in a longer channel, as shown in Fig. 6.9, which simply extends the channel length and confines the bubble locally such as the bubble swarm of the RBI, to recover the fluctuation of the pressure gradient when the bubble passes. Interestingly, near-zero skin friction contours on the liquid film of the large-sized bubble are successfully confirmed from both flow condition from sufficiently large-sized bubbles in all cases, and this effect is maximized when the bubble reaches sufficiently longer in streamwise direction. Thus, the critical equivalent bubble diameter at large-sized bubble can be replaced to the streamwise bubble length ($d_{st.}$) as shown in Fig. 6.10.
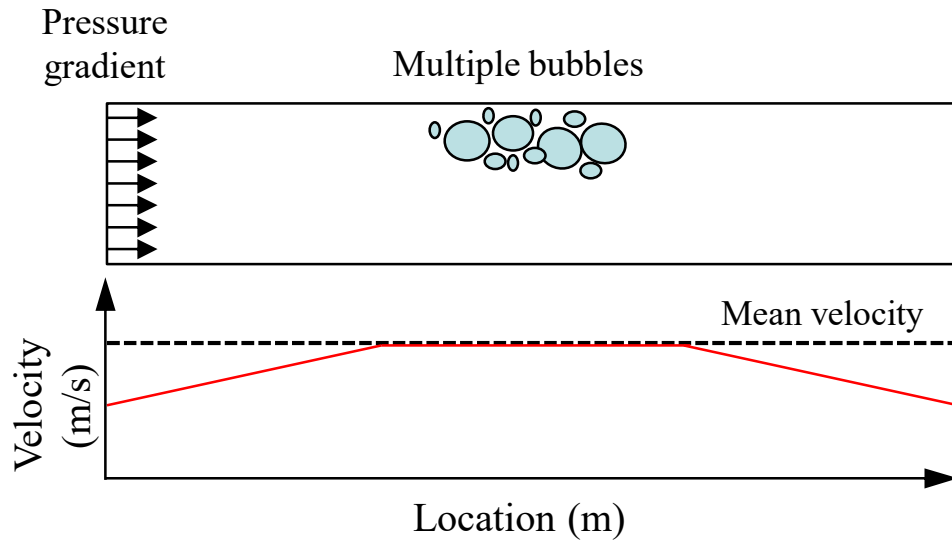
Figure 6.9: Longer channel with locally bubble swarm state.
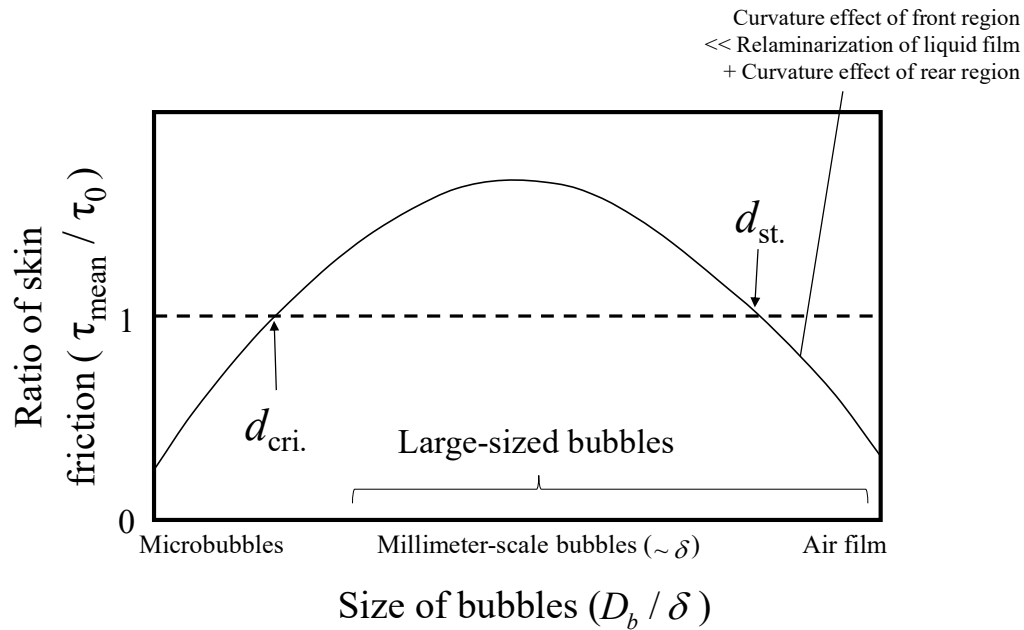
Figure 6.10: Streamwise bubble length ($d_{st.}$) to replace the critical equivalent bubble diameter and the reason of drag reduction of large-sized bubbles.

References

[1] McCormick, M., and Bhattacharyya, R., 1973. Drag reduction of a submersible hull by electrolysis. *Nav. Eng. J.* 85(2), pp. 11–16.

[2] Madavan, N.K., Deutsch, S., and Merkle, C.L., 1984. Reduction of turbulent skin friction by microbubbles, *Phys. Fluids* 27(2), pp. 356-363.

[3] Merkle, C.L., and Deutsch, S., 1992. Microbubble drag reduction in liquid turbulent boundary layers. *ASME appl. Mech. Rev.* 45(3) pp. 103-127.

[4] Kato, H., Iwashina, T., Miyanaga, M., and Yamaguchi, H., 1999. Effect of microbubbles on the structure of turbulence in a turbulent boundary layer. *J. Marine Sci. Tech.* 4, pp. 115-162.

[5] Kodama, Y., Kakugawa, A., Takahashi, T., and Kawashima, H., 2000. Experimental study on microbubbles and their applicability to ships for skin friction reduction. *Int. J. Heat Fluid Flow.* 21(5), pp. 582-588.

[6] Gabillet, C., Colin, C., and Fabre, J., 2002. Experimental study of bubble injection in a turbulent boundary layer. *Int. J. Multiphase Flow* 28(4), pp. 553-578.

[7] Moriguchi, Y., and Kato, H., 2002. Influence of microbubble diameter and distribution on frictional resistance reduction. *J. Mar. Sci. Technol.* 7(2), pp. 79–85.

[8] Kawamura, T., Moriguchi, Y., Kato, H., Kakugawa, A., and Kodama, Y., 2003. Effect of bubble size on the microbubble drag reduction of a turbulent boundary layer. *Proc. ASME/JSME Fluids Eng. Conf. Summer Meeting 2003*, pp. 647-654.

[9] Shen, X., Perlin, M., and Ceccio S.L., 2006. Influence of bubble size on microbubble drag reduction. *Exp. Fluids* 41, pp. 415-24.

[10] Kitagawa, A., Hishida, K., and Kodama Y., 2005. Flow structure of microbubble-laden turbulent channel flow measured by PIV combined with the shadow image technique. *Exp. Fluids* 38, pp. 466-475.

[11] Lu, J., Fernandez, A., and Tryggvason, G., 2005. The effect of bubbles on the wall drag in a turbulent channel flow. *Phys. Fluids* 17(9), 095102.

[12] Sugiyama, K., Kawamura, T., Takagi, S., and Matsumoto, Y., 2005. Recent Progress of Microbubble Flow Simulation for Elucidating Drag Reduction Mechanism. *Proc. of the 6th Symp. on Smart Control of Turbulence*, pp. 191–202.

[13] Kawamura, T., 2005. Numerical and experimental investigation the mechanism of the microbubble drag reduction. *Proc. 6th Symposium Smart Control of Turbulence.*

[14] Fukuda, K., Tokunaga, J., Nobunaga, T., Nakatani. T., Iwasaki, T., and Kunitake, Y., 1999. Frictional Drag Reduction with Air Lubricant over Super Water Repellent Surface (2nd Report) -Resistance Tests of Tanker and High Length to beam ratio Ship Models-, *J. Soc. N.A. Japan* 186.

[15] Matsumura, K., Kaminaga, F., and Saito, H., 2002. Drag reduction on super water repellent surface with air injection method: 2nd report, drag reduction mechanism. *JSME, Trans, B* 68(671) pp. 32-38 (in Japanese).

[16] Katsui, T., Okamoto, Y., Kasahara, Y., Shimoyama, N., Iwasaki, Y., Soejima, S., and Hirayama, A., 2003. A study of air lubrication method to reduce frictional resistance of ship. *J. Kansai Soc. N.A., Japan* 239, pp. 45-53 (in Japanese).

[17] Fukuda, K., Tokunaga, J., Nobunaga, T., Nakatani, T., Iwasaki, T., and Kunitake, Y., 2000. Frictional drag reduction with air lubricant over a super-water-repellent surface. *J. Mar. Sci. Technol.* 5(3), pp. 123-130.

[18] Mäkiharju, S. A., Elbing B. R., Wiggins, A., Schinasi, S., Vanden-Broeck, J. -M., Perlin, M., Dowling, D. R., and Ceccio, S. L., 2013. On the scaling of air entrainment from a ventilated partial cavity. *J. Fluid Mech.* 732, pp. 47-76.

[19] Murai, Y., Fukuda, H., Oishi, Y., Kodama, Y., and Yamamoto, F., 2007. Skin friction reduction by large air bubbles in a horizontal channel flow. *Int. J. Multiphase Flow*

33(2), pp 147–163.

[20] Oishi. Y., and Murai. Y., 2014. Horizontal turbulent channel flow interacted by a single large bubble. *Exp. Therm. Fluid Sci.* 55, pp. 128–139.

[21] Park, H.J., Tasaka, Y., and Murai, Y., 2019. Bubbly drag reduction investigated by time-resolved ultrasonic pulse echography for liquid films creeping inside a turbulent boundary layer. *Exp. Therm. Fluid Sci.* 103, pp. 66–77.

[22] Kim, S.W., Oshima, N., Murai, Y., and Park, H.J., 2020. Numerical investigation of a single intermediate-sized bubble in horizontal turbulent channel flow. *J. Fluid Sci. Technol.* 15(3).

[23] Park, H. J., Tasaka, Y., Oishi, Y., and Murai, Y., 2015. Drag reduction promoted by repetitive bubble injection in turbulent channel flows. *Int. J. Multiphase Flow* 75, pp. 12-25.

CHAPTER **7**

Concluding remarks

7.1 Summaries of each chapter

We developed a numerical model of the large-sized bubbles in a turbulent boundary layer. Numerical simulations were performed using horizontal rectangular channels to evaluate the drag reduction mechanism of large-sized bubbles. The details are reported in Chapters 3–6. Summaries of the contents in each chapter are described below.

In **Chapter 3**, the behaviors and properties of a large-sized bubble in a horizontal turbulent channel flow were investigated by dividing the calculation process into three stages. The current solver selected from Chapter 2 minimizes the numerical error and displays the proper volume conservation. The numerical results such as bubble shape, skin friction, and instantaneous momentum flux above the bubble show trends similar to those of the experiment. In the case of the secondary flow on the current bubble, high skin friction is generated, and this region is broadened as the wake length increases, which corresponds to the distribution of the streamwise vortices in the secondary flow. Further, this behavior of the secondary flow can be described by the interaction between the pair of vortices that are generated on the upper wall and the upper surface of the bubble, and it can be divided into three sequences describing the shape of the vortices, allowing us to identify the reason for the increase in the drag.

In **Chapter 4**, DNSs of a series of large-sized bubbles were conducted to analyze their drag modulation effect as spatial and temporal locations. First, the local skin friction profiles of whole bubbles exhibited a uniform trend in the core regions, and the minimal value at the rear region of the bubbles decreased as the Weber number increased. Considering the mean ratio of skin friction used to define each local area, the local mean ratio of skin friction decreases as the local bubble length increases. From the mean ratio and instantaneous contours of skin friction analyzed for the liquid film and secondary flow regions, the mean ratio of skin friction in the streamwise direction was found to be generally greater than unity, eventually converging to the unit value with the continued increase in Weber number, which implies that drag reduction in the bubble using only the liquid film is difficult. However, this lack of drag reduction performance was recovered from the secondary flow, and an effective length of the secondary

flow was obtained. In contrast, the absolute value of the skin friction in the spanwise direction was observed to concentrate on the span edge of the liquid film, and it continued to the secondary flow; the observed skin friction in the spanwise direction is a good indicator, implying that a high momentum flux occurred in this region and confirmed the balance between the curvature effect of front region and relaminarization of liquid film including curvature effect of rear region causes drag increase and decrease.

In **Chapter 5**, the numerical flow visualization of a single large-sized bubble in a turbulent Couette channel flow was performed. As expected for a single large-sized bubble in turbulent Couette flow, the representative shape characteristics of the large-sized bubble, such as the liquid film and the capillary wave, were formed in the opposite direction to those at Poiseuille flow. From the physical mechanism of bubble deformation in turbulent Couette channel flow, it can be categorized into five states, and the deformation is periodic. The deformation of the bubble is dominated by the displacement of the main part of the bubble, which experiences an acceleration of velocity greater than that of the single-phase flow from the liquid film region. Furthermore, the acceleration of velocity in this region may cause additional deformation of the tip, such as the development of ligament.

In **Chapter 6**, DNSs of large-sized bubbly flows in turbulent Poiseuille and Couette channel flows are described. The turbulent Couette flow shows reasonable numerical results, while turbulent Poiseuille flow shows oscillation in the flow owing to an improper pressure gradient. Thus, further study of turbulent Poiseuille flow will be conducted using the proposed model. Additionally, near-zero skin friction contours on the liquid film of the large-sized bubble are successfully confirmed from both flow condition from sufficiently longer bubble in streamwise direction which can replace the critical equivalent bubble diameter at large-sized bubble. Thus, the present numerical model is available to reproduce the important phenomenon of the large-sized bubbles for drag reduction.

To summarize, several numerical simulations of large-sized bubbly flows have been analyzed and applied to the simulation of physical bubble size and flow conditions. In addition, the scalability test, which is a crucial element for large-scale computations, has been considered. This represents a step forward toward numerical simulations of the large-sized bubbles under practically relevant conditions.

Journals

1. **Kim, S.W.**, Oshima, N., Murai, Y., and Park, H.J., 2021. Direct numerical simulation of frictional drag modulation in horizontal channel flow subjected to single large-sized bubble injection. *Int. J. Multiphase Flow*, (under review).

2. **Kim, S.W.**, Oshima, N., Murai, Y., and Park, H.J., 2020. Numerical investigation of a single intermediate-sized bubble in horizontal turbulent channel flow. *J. Fluid Sci. Technol.* 15(3).

3. **Kim, S.W.**, Oshima, N., Lee, S.E., Lee, G.W., and Seo, K.C., 2020. Hydrodynamic Performance and Appendage Considerations of Wave-Piercing Planing Craft Overlapping Waves and Porpoising. *J. Fluid Sci. Technol.* 15(2).

4. Lim, J.T., Seo, K.C., Park, G.H., and **Kim, S.W.**, 2018. A Numerical Study on the Selection of Main Specification of the 18.5ft Bass Fishing Boat. *J. Korean Soc. Mar. Environ. Saf.* 24(7), pp. 945-952. (in Korean)

5. **Kim, S.W.**, Seo, K.C., Lee, D.K., and Lee, G.W., 2017. A Numerical Study on Dynamic Instability Motion Control of Wave-Piercing High-Speed Planing Craft in Calm Water using Side Appendages. *J. Korean Soc. Mar. Environ. Saf.* 23(3), pp. 320-329.

6. Oh, Y.N., **Kim, S.W.**, Lee, K.W., Han, S.J., and Kim, I.C., 2016. A Study on the Characteristics of Vertical Motions due to Changes of Submerged Shape in the Multi-Purpose Small Floating Body. *J. Fish. Mar. sci.* 28(4), pp. 1024-1030.

International conference papers

Proceedings

1. **Kim, S. W.**, and Oshima, N., 2021. Numerical flow visualization of large-sized bubble in turbulent Couette channel flow using OpenFOAM. *19th International Symposium on Flow Visualization*, Shanghai, China.

2. **Kim, S.W.**, and Oshima, N., 2021. Numerical Prediction of a Large Bubble Behavior in Wall Turbulent Flow. *14th WCCM ECCOMAS Congress 2021*, Virtual Congress.

3. **Kim, S.W.**, Oshima, N., Lee, S.E., Lee, G.W., and Seo, K.C., 2019. Hydrodynamic Performance and Appendage Considerations of Wave-Piercing Planing Craft Overlapping Waves and Porpoising. *ASME-JSME-KSME Joint Fluids Engineering Conference 2019*, San Francisco, USA

4. Wang, L., Oshima, N., and **Kim, S.W.**, 2019. Analysis on Heat Transfer and Phase Change for Two-Phase Boiling Flow in Quenching Process. *ASME-JSME-KSME Joint Fluids Engineering Conference 2019*, San Francisco, USA

5. **Kim, S.W.**, and Oshima, N., 2019. Improvement of the Prediction Accuracy of Non-premixed Piloted Methane Jet Flame. *The 9th East Asia Mechanical and Aerospace Engineering Workshop 2019*, Korea University, Korea.

6. Oshima, N., and **Kim, S.W.**, 2019. Numerical simulation of turbulent combustion flows in industrial gas turbine combustors. *The 9th East Asia Mechanical and Aerospace Engineering Workshop 2019*, Korea University, Korea.

7. **Kim, S.W.**, Lee, G.W., and Seo, K.C., 2017. A Comparison on Resistance Performance and Running Attitude of Asymmetric Catamaran Changing shape of Tunnel Stern Exit Region. *International Conference on Naval Architecture and Ocean & Marine Engineering 2017*, Hong Kong, China.

Posters

1. **Kim, S.W.**, Lee, G.W., Seo, K.C., and Park, G.H., 2017. A Comparative Study on Evaluate Seakeeping Assessment of the Planing Hull between Strip Method and CFD. *International Conference on Naval Architecture and Ocean & Marine Engineering 2017*, Hong Kong, China.

2. Kim, B.J., Lee, G.W., Seo, K.C., and **Kim, S.W.**, 2017. A Study on the Transverse Step Application Location and Height of High-Speed Planing Hull by Numerical Analysis. *International Conference on Naval Architecture and Ocean & Marine Engineering 2017*, Hong Kong, China.

Preprints of domestic conferences

1. **Kim, S.W.**, Oshima, N., Murai, Y., and Park, H.J., 2020. Direct Numerical Simulation for Drag reduction effect of a Single Intermediate-sized Bubble. *The Japanese Society of Mechanical Engineering Division of Fluid Dynamics 98th Conference*, Online, Japan.

2. **Kim, S.W.**, Oshima, N., Murai, Y., and Park, H.J., 2019. Numerical Investigation of Single Large Bubble Injection in Turbulent Channel Flow. *33rd Computational Fluid Dynamics Symposium*, Sapporo, Japan.

3. **Kim, S.W.**, Oshima, N., Murai, Y., and Park, H.J., 2019. Numerical Simulation on Turbulent

Channel Flow for Single Large Bubble near the Wall. *The Japanese Society of Mechanical Engineering Division of Fluid Dynamics 97th Conference*, Toyohashi, Japan.

4. **Kim, S.W.**, Oshima, N., Song, S.W., and Cho, D.H., 2018. A Numerical Study on flow characteristics of tube with the sudden enlargement as changing perforated plates. *The Japanese Society of Mechanical Engineering Division of Fluid Dynamics 96th Conference*, Muroran, Japan.

5. Kim, D.H., Seo, K.C., **Kim, S.W.**, Jang, Y.H., and Kim, J.H., 2018. A Numerical Study of Drag and Lift According to Changing Rudder Shape. *Annual Autumn Meeting, The Korean Society of Marine Environment & Safety*, Busan, Korea (in Korean).

6. **Kim, S.W.**, Lee, G.W., Seo, K.C., Cho, D.H., and Kim, B.J., 2017. The Comparison on Pressure and Lift Distribution of Asymmetric Catamaran Changing Shape of Tunnel Stern. *Annual Autumn Meeting, The Korean Society of Marine Environment & Safety*, Busan, Korea (in Korean).

7. **Kim, S.W.**, Lee, G.W., Seo, K.C., Cho, D.H., and Kim, B.J., 2017. The Comparison on Resistance Performance and Running Attitude of Asymmetric Catamaran Changing Angle of Inclination of Tunnel Stern Exit Region. *Annual Autumn Meeting, Korean Institute of Navigation and Port Research*, Busan, Korea (in Korean).

8. **Kim, S.W.**, Lee, G.W., Seo, K.C., Cho, D.H., and Park, G.H., 2017. A Numerical Additional Study for Evaluate Seakeeping Assessment of the Planing Craft. *Annual Autumn Meeting, Korean Institute of Navigation and Port Research*, Busan, Korea (in Korean).

9. **Kim, S.W.**, Lee, G.W., Seo, K.C., Cho, D.H., and Park, G.H., 2017. A Numerical Additional Study for Evaluate Seakeeping Assessment of the Planing Craft. *Annual Autumn Meeting, Korean Institute of Navigation and Port Research*, Busan, Korea (in Korean).

10. **Kim, S.W.**, Lee, G.W., Lee, D.H., Seo, K.C., and Jeong, T.Y., 2016. A Study on Resistance and Running Attitude of Small High-Speed Planing Hull using CFD. *Annual Autumn Meeting, The Korean Society of Marine Environment & Safety*, Korea Coast Guard Academy, Korea (in Korean).

11. **Kim, S.W.**, Lee, G.W., Seo, K.C., Lee, D.K., Jeong, T.Y., and Lee, C.W., 2016. A Study on Posture Stability of Wave-Piercing High-Speed Planing Hull according to the ship's side fin. *Annual Autumn Meeting, The Korean Society of Marine Environment & Safety*, Korea Coast Guard Academy, Korea (in Korean).

12. Lim, J.T., Seo, K.C., Park, G.H., and **Kim, S.W.**, 2017. A Study on CFD Method for the Small Planing Craft. *Annual Autumn Meeting, Korean Institute of Navigation and Port*

Research, Gyeongju, Korea (in Korean).

13. Son, S.H., **Kim, S.W.**, Lee, G.W., and Cho, D.H., 2016. A Study on Exothermic Accident in Main Bearing of Patrol Type High-Speed Government Vessels. *Annual Spring Meeting, The Korean Society of Mechanical Technology*, Wonkwang University, Korea (in Korean).

14. Kim, B.J., **Kim, S.W.**, Cho, D.H., Lee, G.W., and Seo, K.C., 2016. Field of Vision from Helm Position of Patrol Type High-Speed Government Vessels Assessment with ISO Standard Rule. *Annual Spring Meeting, The Korean Society of Marine Environment & Safety*, National Marine Biodiversity Institute of Korea, Korea (in Korean).

15. **Kim, S.W.**, Cho, D.H., Oh, W.J., Seo, K.C., and Lee, G.W., 2015. A Study on the Improvement in Resistance Performance of a Patrol Type High-Speed vessel that Apply shapes of Concavo-convex. *Annual Spring Meeting, The Korean Society of Marine Environment & Safety*, Gyeongsang National University, Korea (in Korean).

16. Kim, K.B., Lee, C.W., **Kim, S.W.**, Lee, D.J., Bea, J.D., and Lee, G.W., 2015. A Safety Performance Study of Block-Type Kayak using Pol. *Annual Spring Meeting, The Korean Society of Marine Environment & Safety*, Mokpo National Maritime University, Korea (in Korean).

Curriculum vitae

Kim, Sangwon (金 相元)

EDUCATION

Oct.2018 - Sep.2021	Ph.D. of Engineering, Division of Mechanical and Aerospace engineering, Graduate School of Engineering, Hokkaido University, Japan.
Mar.2015 - Feb.2017	Master of Engineering, Department of Ocean system Engineering, Graduate School, Mokpo National Maritime University, Korea.
Mar.2008 - Feb.2012	Bachelor of Engineering, Department of Naval Architecture and Ocean Engineering, College of Maritime Engineering, Mokpo National Maritime University, Korea.

Professional experience

Mar.2012 - Feb.2015	Military Service (Officer), Republic of Korea Navy, Korea.

Honors and awards

Grants

Mar.2021 - Mar.2022	Large scale simulations of flows of high weber number bubble with flow conditions of ship using OpenFOAM, Research Grant from Fugaku Junior Researchers: FY2021 (Period A), hp210160.
Oct.2020 - Mar.2021	Large scale simulations on the flow of multiple high weber number bubbles by using OpenFOAM, Research Grant from Fugaku Preliminary Use Project (Startup Preparation), hp200223.
Apr.2020 - Mar.2022	A Study on the Reduction of Fuel Efficiency of Vessels (Direct Numerical Simulation of Fuel Efficiency Reduction by Bubble Lubrication of Vessels), Research Grant from the Fundamental Research Developing Association for Shipbuilding and Offshore.

Awards

Feb.2012   Excellent Graduation Award from the Society of Naval Architects of Korea.

Scholarships

Apr.2020- Mar.2021   MEXT Honor Scholarship from Japan Student Services Organization.

Oct.2018- Mar.2019   MEXT Honor Scholarship from Japan Student Services Organization.

Sep.2011   Navy ROTC Scholarship from Naval Reserve Officers Training Corps, Mokpo National Maritime University.

Sep.2011   Academic Distinction Scholarship from Mokpo National Maritime University.

Mar.2010 - Sep.2010   Navy ROTC Scholarship from Naval Reserve Officers Training Corps, Mokpo National Maritime University.

Sep.2008 – Mar.2010   Academic Distinction Scholarship from Mokpo National Maritime University.